Aix*Marseille université
Socialement engagée

NNT : 2023AIXM0001

THÈSE DE DOCTORAT

Soutenue à Aix-Marseille Université
le 27 mars 2024 par

Luca CAPPELLI

Study of the dynamics and passive control of heavy ions produced by plasma-wall interaction: toward the elaboration of a predictive model in the suite of codes SOLedge2D-EIRENE from experiments on the tokamak WEST

Discipline
Sciences pour l'ingénieur

Spécialité
Fusion magnétique

École doctorale
ED 353 Sciences pour l'ingénieur : mécanique, physique, micro et nanoélectronique

Laboratoire/Partenaires de recherche
M2P2 - Aix-Marseille Université, CNRS École Centrale Méditerranée
IRFM, CEA

Composition du jury

David TSKHAKAYA Senior Scientist, CAS	Rapporteur
Andreas KIRSCHNER Senior Scientist, IEK	Rapporteur
Richard PITTS Senior Scientist, ITER	Examinateur
George Tynan Professor, UCSD	Examinateur
Clarisse Bourdelle Dir. de Recherche, CEA	Examinatrice
Tiberiu MINEA Professeur, UPS	Président du jury
Eric SERRE Dir. de Recherche, CNRS	Directeur de thèse
Nicolas FEDORCZAK Chercheur, CEA	Co-encadrant de thèse
Yannick MARANDET Dir. de Recherche, CNRS	Membre invité

M2P2 UMR 7340 CNRS - Aix-Marseille Université - Centrale Marseille

cea irfm

Affidavit

I, undersigned, Luca Cappelli, hereby declare that the work presented in this manuscript is my own work, carried out under the scientific supervision of Eric Serre and Nicolas Fedorczak, in accordance with the principles of honesty, integrity and responsibility inherent to the research mission. The research work and the writing of this manuscript have been carried out in compliance with both the french national charter for Research Integrity and the Aix-Marseille University charter on the fight against plagiarism.

This work has not been submitted previously either in this country or in aother country in the same or in a similar version to any other examination body.

Aix-en-Provence 16 janvier 2024



This work is licensed under Creative Commons Attribution-NonCommercial-NoDerivatives 4.0 International Public License

Liste de publications et participation aux conférences

Liste des publications et/ou brevets réalisées dans le cadre du projet de thèse:

1. L Cappelli et al 2023 Plasma Phys. Control. Fusion 65 095001
   DOI: 10.1088/1361-6587/ace282

2. L Cappelli et al 2023 Nuclear Materials and Energy 37 101551
   DOI: 10.1016/j.nme.2023.101551

3. N Fedorczak, S Di Genova, C Guillemaut, R Guirlet, L Cappelli, et al.. Tungsten sources and core contamination in WEST plasmas: from experiments to simulations. OSI25 - 25th International Conference on Plasma Surface Interaction in Controlled Fusion Devices, Jun 2022, E-Conference, South Korea. ffcea-03784806f

Participation aux conférences et écoles d'été au cours de la période de thèse:

1. 19th International Conference on Plasma-Facing Materials and Components for Fusion Applications, May 22 - 26, 2023

Résumé

La fusion dans les tokamaks est proposée comme une alternative pour une production d'énergie durable, mais les interactions plasma-paroi entravent son développement. La décharge de puissance du plasma vers le tokamak entraîne l'érosion des composants mécaniques et la contamination du plasma par des particules érodées. Le tungstène est un matériau prometteur pour prolonger la durée de vie des composants, mais sa gestion dans le plasma, par rapport à des espèces plus légères comme le carbone, reste un défi. La recherche en fusion vise à modéliser l'érosion et le transport des impuretés, cruciales pour soutenir les expériences et concevoir des réacteurs comme ITER. Les modèles fluides sont prometteurs, mais nécessitent des conditions aux limites appropriées. Cette thèse se concentre sur la modélisation de l'érosion et de la redeposition du tungstène via des techniques Monte Carlo et des modèles analytiques, dans une gaine de plasma sans collision et sur une surface érodée lisse. La simulation concerne la région du plasma adjacente à une paroi solide, incluant la gaine de Debye plus la gaine de Chodura (autrement appellée gaine de plasma), et une partie du SOL. Dans la gaine de plasma, caractérisée par un champ électrique dominant et des gradients de densité électronique, des modèles cinétiques sont nécessaires pour résoudre le problème du transport. Une partie de la recherche se consacre à la construction d'un modèle pour la gaine, utilisant un modèle Monte Carlo pour calculer des cartes de probabilité de redeposition, offrant une alternative au suivi des particules. L'étude explore l'impact de différentes distributions d'énergie des ions sur l'érosion et la redeposition. Les résultats indiquent que l'approximation de l'énergie moyenne sous-estime ces phénomènes seulement si l'énergie moyenne est proche du seuil d'énergie de pulvérisation. Une base de données sur la redeposition du tungstène a été créée et utilisée pour former un réseau de neurones (NN) et un modèle analytique. Le NN est précis mais lié à des conditions fixes, tandis que le modèle analytique est plus flexible mais moins précis. Les tests expérimentaux ont validé les hypothèses du modèle de la gaine, montrant un accord entre modélisation et mesures. Le modèle analytique a été appliqué à la base de données WEST pour comprendre les sources de tungstène au divertor inférieur. Cette thèse apporte des perspectives sur la physique de l'érosion et de la redeposition du tungstène dans un contexte sans collision, avec des implications pratiques. Les outils de modélisation développés peuvent être intégrés dans des solveurs de plasma, ouvrant la voie à des simulations innovantes pour la conception de futurs réacteurs tokamak avec du tungstène.

Mots clés: tungstène, érosion, redéposition, interaction plasma-paroi, modèles cinétiques, Monte Carlo

Abstract

Fusion, in the context of tokamak devices, is suggested as an alternative for sustainable and high-performance energy production. To date, one of the issues preventing its industrial development, concerns plasma-wall interactions. Power discharged from the plasma to the tokamak vessel has two main consequences: gradual erosion of mechanical components and contamination of the plasma by eroded species. Tungsten (W) has emerged as a promising material to enhance the lifespan of mechanical components in tokamaks. However, managing W concentrations in the plasma, especially in comparison to lighter species like carbon, poses a challenge. Ongoing fusion research aims for reliable modeling of erosion and transport of impurities. Modeling is fundamental to support experiments, design and prepare optimized scenarios for future reactors as ITER. In particular fluid models are a promising tool for this end, but they need proper boundary conditions. This Ph.D. thesis delves into the modeling of W erosion and redeposition through Monte Carlo techniques and analytical models in the limit of a collisionless plasma sheath and a smooth eroded surface. The research involves simulating W erosion and transport in the plasma region adjacent to a solid wall, encompassing the combined Debye sheath and Chodura sheath (referred to as the plasma sheath) and a segment of the SOL with dimensions on the order of the Larmor radius of the eroded species. The plasma sheath plays a pivotal role in the erosion and redeposition of W. It is characterized by the presence of a dominant electric field and strong electron density gradients, making kinetic models the only way to solve transport within it. A portion of this research is dedicated to building a model for the sheath, which serves as a plasma background where eroded particle transport is solved using Monte Carlo techniques. The Monte Carlo model computes redeposition probability maps, offering an alternative method to particle tracking for the calculation of redeposition. The study also explores the impact of different impinging energy distributions of ions in both erosion and redeposition. Results indicate that approximating the energy distribution of impinging ions on the eroded material with the average energy underestimates erosion and redeposition only if the average energy is close to the sputtering energy threshold. Otherwise, even using the average energy is accurate. A large database regarding W redeposition was rapidly created using the redeposition probability maps. Data was then used to train a Neural Network (NN), capable of estimating redeposition as a function of local plasma parameters. Additionally, an analytical model is provided to explain the main mechanisms of redeposition and how to roughly estimate redeposition through integration. This approach is less accurate but it is more flexible because it does not need the use of probability maps, nor it is valid for a set of fixed conditions, as the NN. The analytical model allows to rapidly estimate other important parameters such as temperature

and average charge state of sputtered and not-redeposited W. Experimental testing validates the sheath model assumptions regarding the electric potential drop, showing good agreement between modeling and experimental measures. Furthermore, the analytical model is applied to the WEST database to gain insights into W sources at the lower divertor. This Ph.D. thesis contributes in plasma-material research providing fundamental insights into the physics of local W erosion and redeposition in the collisionless limit. Beyond its theoretical contributions, this work has practical implications since it provides different modeling tools to estimate local W erosion. Such tools can be integrated into multispecies plasma solvers, paving the way for innovative time-dependent simulations. This in turn could be valuable for the design and optimization of future tokamak reactors incorporating W.

Keywords: Tungsten, Erosion, Redeposition, Plasma-wall interactions, kinetic models, Monte Carlo

Remerciements

These acknowledgements are addressed to everyone who played a role in supporting and assisting me throughout my Ph.D. thesis. First and foremost, I thank my supervisor, Nicolas Fedorczak, for showing me what science really is and for guiding me through numerous exchanges of ideas and inspiring discussions. I thank my thesis director, Eric Serre, for his prompt and constant availability in offering assistance. In addition, I thank Guido Ciraolo and Alberto Gallo. Without meaning to, they have been reference figures I have always known I could count on.

The doctoral program, if you are lucky enough, surrounds you with outstanding colleagues. I am talking about colleagues and friends like Stefano Di Genova, Mathieu Carole, Tullio Barbui and Yaakoub Boumendjel. I am really grateful to have met people like you. I would like to take this opportunity to thank my tungsten-enthusiastic colleague and friend Stefano Di Genova, for the scientific discussions, and for showing me the doctoral offer thanks to which I am here today writing this manuscript.

Of course, my deepest thanks go to my family, who is always welcoming and sheltering me in spite of everything. Thank you Mom, Thank you Dad, Thank you Francesca. I extend my gratitude to my partner, Alejandra, for infusing every moment we share with joy and serenity.

Finally, I thank my lifelong friends for all the good memories that their names bring to my mind. Thank you Dario, Giordano, Amar, Andrea Q., Andrea Z., Luca F., Alex, Marco, Lorenzo and Massimiliano.

Each of you, in one way or another, has played a part in my personal growth, and through this page, I have found the courage to thank you.

Contents

Affidavit 2

Liste de publications et participation aux conférences 3

Résumé 4

Abstract 5

Remerciements 7

Contents 8

Introduction 10
- 0.1 Controlled nuclear fusion . . . 10
  - 0.1.1 Power balance and the exhaust issue in tokamaks . . . 11
- 0.2 Tungsten as plasma facing material . . . 14
- 0.3 Context and Thesis goal . . . 15

1 Overview of Plasma-Wall Interactions 18
- 1.1 Erosion of solid surfaces under particle bombardment . . . 18
  - 1.1.1 Physical sputtering . . . 19
  - 1.1.2 Reflections and evolution of eroded surfaces . . . 23
- 1.2 Plasma sheath . . . 26
  - 1.2.1 Presheath . . . 28
- 1.3 Langmuir Probes . . . 30
- 1.4 Erosion . . . 31
  - 1.4.1 Gross erosion . . . 31
  - 1.4.2 Net erosion . . . 32

2 Monte Carlo modelling of local erosion and redeposition 34
- 2.1 Definitions and context . . . 35
  - 2.1.1 Energy of sputtered ions . . . 35
- 2.2 Sheath model employed . . . 36
  - 2.2.1 Boundary condition - distributions at the Sheath Entrance . . . 38
  - 2.2.2 W erosion and redeposition . . . 39
- 2.3 Monte Carlo simulation . . . 41
  - 2.3.1 Numerical setup . . . 42
  - 2.3.2 Model validation . . . 44

2.4 Results . . . 45
2.4.1 Neutral W non redeposition dependence on plasma parameters and boundary conditions . . . 45
2.4.2 Effective sputtering yield . . . 51
2.4.3 Plasma ions erosion - Deuterium . . . 53
2.4.4 Potential drop model uncertainty . . . 54
2.5 Discussion . . . 55

3 Model reduction through Neural Network and analytical models 58
3.1 Neural Network-based estimation of W redeposition . . . 58
3.1.1 Database production and data preprocessing . . . 59
3.1.2 NN features and results . . . 60
3.1.3 Prompt redeposition or total redeposition? What is best for a fluid plasma solver . . . 63
3.2 Analytical model to estimate prompt redeposition . . . 64
3.2.1 Energetic redeposition . . . 64
3.2.2 Geometric redeposition . . . 69
3.2.3 Collisional sheath . . . 76
3.2.4 Two-groups theory . . . 77
3.2.5 Three-groups and tuning of the code . . . 80
3.3 Prompt self sputtering . . . 86

4 Experimental validation of the sheath model and application of the 3-groups model to the WEST database 92
4.1 Model validation of tungsten erosion and redeposition properties using biased tungsten samples on DiMES . . . 93
4.1.1 Introduction . . . 93
4.1.2 Materials and methods . . . 94
4.1.3 Numerical simulation . . . 96
4.1.4 Results . . . 98
4.1.5 Discussion . . . 100
4.2 Application of 3-groups model model for erosion and redeposition to the WEST database . . . 101
4.2.1 Post-processing of WEST C7 campaign . . . 101
4.2.2 Proxies of impurity ions at the WEST lower divertor . . . 103

Conclusion 112

Bibliography 116

Introduction

0.1 Controlled nuclear fusion

Nuclear fusion is a phenomenon where two atomic nuclei combine to form a heavier nucleus, releasing a significant amount of energy. It is the same process that powers the sun and other stars. Unlike nuclear fission, where heavy nuclei split into smaller ones, nuclear fusion involves the fusion of light nuclei, typically isotopes of hydrogen, to form helium nuclei also called alpha particles. To attain fusion, extreme conditions are essential, demanding exceptionally high temperatures and/or pressures that transform the fuel into a hot (or better thermonuclear) plasma. These conditions are imperative to bring atomic nuclei into close proximity, overcoming the inherent electrostatic repulsion. As the nuclei approach, the strong nuclear force binds them together provoking the fusion process. The hidden advantages of nuclear fusion energy are manifold and have attracted the interest of scientists who, for many decades, have tried to achieve fusion in a controlled manner. Fusion energy is regarded as a sustainable, long-term solution to address the current global energy demand, especially in the face of the urgent challenge posed by climate change. However, the technological difficulty of managing the necessary extreme conditions to sustain it remains unsolved. Additionally, the competition with other technologies raises uncertainties about the penetration of fusion into the market even once successfully developed [1].
To date, different fusion concepts and machines have been tested, all with the same goal of igniting a stable fusion chain. Among them, there are magnetic confinement machines such as stellarators and tokamaks who confine a thermonuclear plasma using magnets. Regardless of the concept, in order to attain stable fusion reactions, all machines have to respect the so-called Lawson criterion [2] that sets the conditions under which ignition is theoretically possible.
Ignition happens when the plasma is heated only by its fusion products and does not need further power from external auxiliary systems to keep burning. Fusion feeds itself through the production of alpha particles which lose all their energy through collision in the plasma. The power P_α released by alpha particles is directly proportional to the rate at which alpha particles are produced multiplied by the initial energy ϵ_α of an individual alpha particle. The production rate is proportional to the plasma density (denoted as n) multiplied by the average of the product of the fusion reaction cross section (denoted as σ) and the relative velocity (v) between reactants.

$$P_\alpha \propto n^2 < \sigma v > \epsilon_\alpha$$

While plasma heats itself through alpha particles it is also subjected to power losses.

In steady state the power loss is equal to the total plasma energy content, denoted as W_p, divided by a characteristic time τ_E called confinement time.

$$P_{loss} = \frac{W_p}{\tau_E}$$

Lawson noticed that the power balance $P_\alpha = P_{loss}$ is respected, thus ignition is possible, only if the product of plasma density (n), temperature (T) and confinement time (τ_E) is greater than a threshold value which depends on the machine and used reactants. The Lawson criterion is hence reported in equation (0.1).

$$nT\tau_E \geq threshold \tag{0.1}$$

In reality the Lawson criterion is strictly valid when the plasma temperature falls within 10-20 keV, because in this interval the reaction rate $<\sigma v>$ is proportional to the square of the plasma temperature ($<\sigma v> \propto T^2$) [3]. As the plasma energy content (W_p) is directly proportional to the product of density and temperature ($W_p \propto nT$), the Lawson criterion (equation 0.1) can be easily shown. An important implication is that machines with high confinement time, or in other words, with a high capacity to retain energy, require to operate with lower density and/or temperature, thus making it is easier to attain ignition. Consequently, new machines such as ITER are designed to achieve high confinement times [4].

0.1.1 Power balance and the exhaust issue in tokamaks

A leading design for achieving controlled nuclear fusion reactions, widely used in fusion research laboratories around the world, is the tokamak. The term "tokamak" is a Russian word which translates to "toroidal chamber with magnetic coils" in English. A tokamak is a type of device used in experimental fusion research to confine hot plasma in the shape of a torus using strong magnetic fields. The magnetic field in a tokamak is created through a combination of poloidal and toroidal coils, see figure 1. Interestingly, the resulting magnetic field is composed by helical field lines around which charged plasma ions and electrons undergo themselves helical motion. Thus, particles are obliged to spiral in the tokamak torus and ideally this would prevent direct contact between plasma and the chamber walls. Such contact could have adverse effects, including damage, cooling, and disruption. In reality, due to other physical phenomenon such as drifts, turbulence, convection, and radiation, the plasma still exchanges energy and matter with the walls of the machine.

In tokamaks the plasma volume is divided in distinct regions known as the core, edge, and scrape-off layer (SOL). These regions exhibit different physical and thermal characteristics. The core is the central region of the plasma where the highest temperature and density are typically found and where the conditions necessary for the nuclear fusion are met. Most of nuclear reactions take place in the core. The Scrape-Off Layer (or SOL) is the region outside the Last Closed Flux Surface (Last Closed Flux Surface (LCFS) or separatrix) where magnetic surfaces are said to be "open" (they

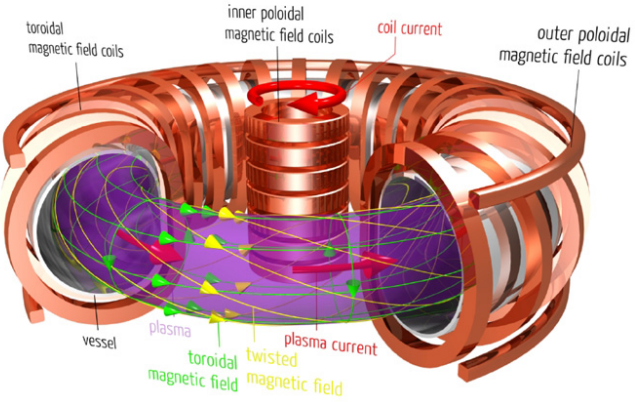

Figure 1: Schematic of a tokamak fusion reactor in limiter configuration (Scheme by Abteilung Offentlichkeitsarbeit - Max-Planck Institut fur Plasmaphysik)

actually close in the solid or outside the machine). In the SOL, plasma is colder than in the core because the wall acts as a sink of particle and heat (see section 1.2), draining power and pressure down around the confined plasma. On the other hand, density, can be as high as in the confined region especially in the presence of an X-point radiator [5]. This is because the wall emits neutral particles back into the plasma through recycling and erosion. Neutrals ionizing up to the separatrix repopulate the SOL while cooling electrons because of collisions, ionization and radiation. The edge is a transition region between the core and the SOL, situated inside the separatrix. It is an important area for studying and controlling plasma instabilities and turbulence. A drawing of the three regions is illustrated in figure 2 where a lower single null (LSN) divertor configuration is presented. Moreover, an example of electron temperature and density profiles found in tokamaks is illustrated in figure 3.

In a steady-state tokamak the power transported P_{SOL} into the SOL, and consequently to the walls, is equal to the total power going in the reactor P_{in} minus the radiative losses P_{rad} happening both in the core and edge. The input power (P_{in}) is roughly equal to the sum of injected power from heating (or auxiliary) systems P_{aux}, and the fusion power liberated in the core P_{α}. Thus the transported power is equal to what reported in equation (0.2).

$$P_{SOL} = P_{\alpha} + P_{aux} - P_{rad} \tag{0.2}$$

As mentioned before particles preferentially follow the field lines. Since tokamaks are toroidally symmetric, the position of a particle within a magnetic flux surface is measured with the normalized poloidal flux ψ_N.

$$\psi_N = \frac{\psi - \psi_0}{\psi_{sep} - \psi_0} \tag{0.3}$$

The coordinate ψ_N is normalized relative to the poloidal flux at the separatrix, ψ_{sep} and adjusted with respect to the poloidal flux at the magnetic axis ψ_0. The definition

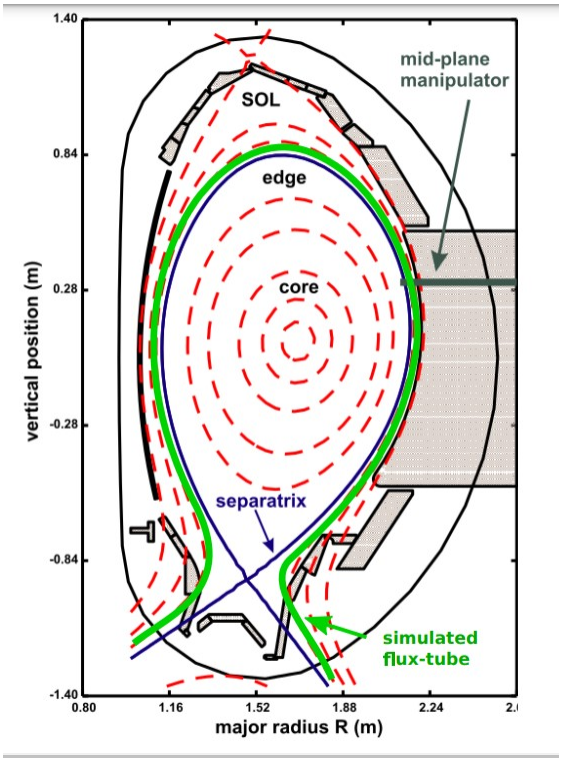

Figure 2: sketch of core,edge and SOL regions for a medium-sized tokamak in a LSN divertor configuration. In red, poloidal cut of some magnetic flux surfaces. In blue, the separatrix, in green, a flux tube in the SOL. Image adapted from [6]

implies that $\psi_N > 1$ ($\psi_N < 1$) outside (inside) the separatrix. The plasma density in the SOL decays exponentially with respect to ψ_N and the power P_{SOL} is mostly focused in a thin flux tube region outside the separatrix, see figure 2. The flux tube bearing the most part of P_{SOL} is large as the typical SOL decay length which depends on the competition between radial (mostly turbulent) and parallel (conduction and sonic flows) transport. If radial transport is strong, the decay length will increase. In tokamaks, the parallel transport is dominant and usually the SOL decay length is in the order of a few millimeters (1-10 mm). Focusing P_{SOL} on a small area proportional to the SOL decay length poses a major challenge on power exhaust management. Unfortunately, the SOL width is hardly controllable, and it generally decreases as global confinement increases (lower radial transport). To date, a popular strategy consists in enlarging the exposed area by optimizing the configuration of the magnetic flux surfaces and the design of exposed Plasma Facing Components (or PFCs). In divertor configurations the magnetic flux surfaces outside the separatrix intersect the so-called divertor-targets (or simply divertors) which as a consequence, bear the highest heat load and particle flux in the machine. The heat flux at the divertor poses a significant challenge for future tokamaks like ITER. This challenge arises from the possibility that the heat flux might exceed the established technological limit of

10 MW/m^2 for stationary loads on its full-tungsten divertor despite optimization of the exposed area, as indicated in studies such as [7] and [8]. That said, not all of the power flowing through the separatrix is discharged to the divertors. A portion of P_{SOL} is lost in the SOL through radiation, and actually, this radiative loss can be artificially increased to mitigate the heat flux. In the tokamaks ASDEX Upgrade [9] and TCV [10] the power radiate in the SOL was increased using the so-called X-point radiator as detailed in [5]. On top of that, other PFCs may be in contact with the SOL, sharing part of the load. Anyway, even if divertors are the most exposed component, no PFC is completely safe. Damage may still be provoked via perpendicular diffusion, runaway electrons, charge-exchange neutrals, Edge Localized Modes (ELMs) and so on.

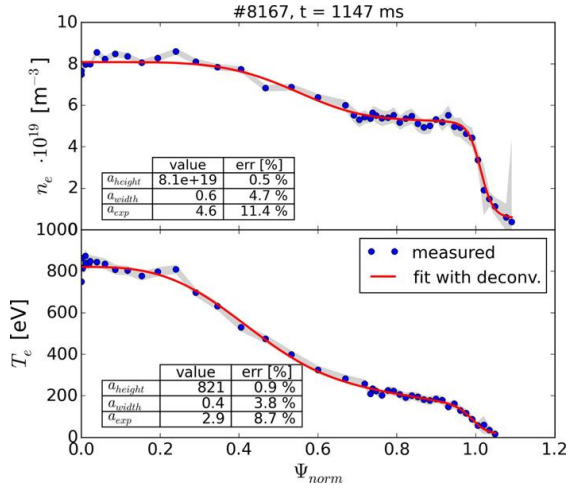

Figure 3: Example of electron density and temperature fitted profiles in COMPASS. Data is shown as function of the magnetic flux coordinate ψ_N defined in equation (0.3). The image is adapted from [11].

0.2 Tungsten as plasma facing material

Despite the possibility to reduce P_{SOL}, thus the heat flux discharged over the walls, a portion of the power will inevitably damage the machine vessel. For this reason extensive research is focused on finding the most suitable plasma-facing material (PFM) to withstand the plasma heat loads. As described in [12] the predilected PFM has transitioned from carbon to tungsten (W). This change is primarily motivated by the high erosion rate of carbon even at low temperatures, and by fuel retention, which increases with fluence making it impossible to safely operate in future reactors. Tungsten on the other hand presents numerous advantages.

1. Low sputtering yield compared to carbon, hence larger lifespan

2. Compatible fuel retention relative to future reactors high fluences

3. Superior heat resistance
4. Low activation and transmutation rate under neutron bombardment
5. Mining supply chain and industrial application already in place

In figure 4 is illustrated a qualitative interpretation of bulk W properties with respect to desired values.

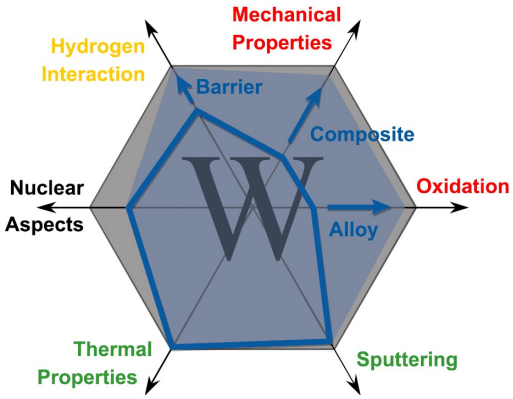

Figure 4: Properties of bulk tungsten (blue line), ideal conditions (blue shadow) and techniques to achieve them. Image adapted from [12]

Unfortunately, adopting a heavy material like tungsten is a double-edged strategy. While it's true that the sputtering yield of tungsten is lower than that of carbon, the acceptable concentration of tungsten in the core is also much lower. Tungsten is an element with elevated cooling factors, even in the core [13]. The reason lies in the high number of electrons of tungsten, emitting line radiation even inside the core where lighter atoms would be instead totally stripped. Although an increase in P_{rad} reduces the power P_{SOL} discharged to the walls (thus reducing erosion), the core temperature decreases. This not only results in lower efficiencies and difficulties in maintaining ignition but also introduces the risk of plasma destabilization and collapse [14]. That being said, current experimental machines such as WEST [15], EAST [16], ASDEX Upgrade [17], and JET [18], successfully operate with tungsten. However, a better understanding of tungsten erosion and its impact on the reactor is crucial. Ideally, having a tool capable of accurately predicting how much tungsten is eroded and how erosion affects reactor performance would be optimal. Such a tool could be used to design future reactors that benefit exclusively from the positive aspects associated with the application of tungsten. In this context, the following doctoral thesis is conceived.

0.3 Context and Thesis goal

Ongoing research focuses on modeling tungsten erosion applying various approaches to accurately simulate both plasma-wall interactions and impurity transport within

the machine. Modelling gives insights into how impurities impact the plasma and how this in turn reflects into both erosion and plasma behavior. Despite the challenges in achieving this objective, various approximations have been proposed over the years, with some commonalities. The plasma solution is fluid and typically treated as steady-state with averaged turbulence, while impurity sources are calculated using a set of approximations regarding the concentration, energy and incidence angle of impinging ions provoking erosion, as well as the associated sputtering yield function, as explained in section 1.4.1. One approach to achieving a stationary solution for plasma and impurity transport involves the use of multi-species fluid solvers, which can simultaneously address plasma, impurities, and their interactions.The main limitation of this approach is related to the inability to fluidly describe both the plasma and the transport of eroded particles within the so-called plasma sheath, whose theory is described in the section 1.2. The necessity for a kinetic solution is justified by several factors, one being that the characteristic size of a fluid element, (on the order of the Larmor radius of the eroded impurity), can surpass the width of the sheath (typically on the order of the Larmor radius of the plasma ion). Consequently, the fluid element is not in thermodynamic equilibrium because the sheath is characterized by strong temperature and density gradients caused by the presence of a net charge. In this case, the fluid solution is intractable. Moreover, a fraction of eroded particles is redeposited on the wall acting as a sink and the probability of redeposition strongly depends on the energy and angular distribution of sputtered particles. To address this challenge, one approach is to consider as boundary condition the so-called 'net' source of impurities, reported in section 1.4.2, rather than the total amount of sputtered particles at the wall, or 'gross' source. The 'net' source is the quantity of particles that traverse the plasma sheath and enter the fluid domain of the simulation. In [19], the net source of W at the WEST divertor was calculated by combining the plasma-wall interaction code EIRENE [20] with a reduced model for translating the gross source from EIRENE to net source. In [21] a multispecies fluid code was used to calculate erosion and W transport in EAST. In this case, the possibility of simplifying the transport of the different ionization states of W by grouping them into bundle charge states to reduce the computational cost was also considered.
Another viable alternative to calculate the sources and transport of impurities is to kinetically solve the transport of impurities throughout the plasma including the sheath using dedicated codes such as ERO2.0 [22] or GITR [23]. In this approach, the plasma fluid solution and the kinetic solution for impurity transport are treated as separate steps. Initially, the plasma solution is computed under the assumption that mutual interactions between the plasma and eroded impurities are negligible. This is true when the concentration of eroded impurities in the plasma is negligible relative to the plasma species density, i.e., the impurities are present in trace amounts. Then the plasma solution is used as fixed input for erosion codes. The erosion codes provide a static plasma solution in the sheath, an estimate of the gross source, and the calculation of impurity transport. In [24, 25], the erosion and transport of W in WEST was addressed by calculating the stationary plasma solution without turbulence using 2D and 3D versions of the SOLEDGE code [19, 26]. Following this, ERO2.0 [22] was

coupled to the plasma solution for the calculation of W erosion and transport. In [27], a quasi-static assumption was used to create a time-dependent feedback loop between SOLEDGE and ERO2.0. This methodology was applied to calculate the time dynamics of W sources during the ramp-up and ramp-down phases of a discharge in the tokamak WEST.
The main goal of the following thesis is to provide a reduced model of the plasma sheath to estimate fundamental quantities about the impurity net sources caused by plasma-wall interactions. This model should be computationally efficient, reasonably accurate, and straightforward to integrate into multispecies fluid solvers, where its purpose would be to address the boundary conditions. This accomplishment would enable time-dependent simulations of erosion and transport without the need for coupling separate fluid and kinetic codes. The thesis focuses on the interface between the plasma and the wall, a region beyond the reach of conventional fluid solvers, serving as the point of connection between them.

In this research, the transport of eroded particles is limited to a confined plasma volume located just above the wall including the sheath. As will be explained in the next chapter, the model reduction of local erosion and redeposition phenomena, particularly concerning heavy species like W, is complicated. For an accurate estimation of crucial parameters related to heavy impurity sources, the employment of kinetic transport models is necessary for both incident and eroded particles within the plasma sheath. In this region, characterized by a strong electric field, the distributions in energy and angle of the incident and eroded particles are significantly skewed. Additionally, the particle transport occurs close to an absorbing and reflecting wall, serving as both a sink and source, and characterized by its own temporal dynamics. In reality, the quantity of eroded impurities exhibits a nonlinear dependence on the temporal evolution of the eroded surface's composition, roughness and geometry. In the upcoming text, we will introduce necessary simplifying assumptions to minimize the loss of generality while addressing the complexities involved in deriving a valid reduced model to calculate the boundary condition.

1 Overview of Plasma-Wall Interactions

Sommaire

1.1 Erosion of solid surfaces under particle bombardment 18
1.1.1 Physical sputtering 19
1.1.2 Reflections and evolution of eroded surfaces 23
1.2 Plasma sheath 26
1.2.1 Presheath 28
1.3 Langmuir Probes 30
1.4 Erosion 31
1.4.1 Gross erosion 31
1.4.2 Net erosion 32

1.1 Erosion of solid surfaces under particle bombardment

The surfaces of solids are eroded when exposed to beams of radiation. This phenomenon, known as sputtering, has always accompanied plasma discharges and has become one of the major obstacles that still interfere with the achievement of controlled thermonuclear fusion. Sputtering in plasma is primarily caused by heavy ions and molecules; however, this does not negate the possibility of sputtering from electrons and photons for high enough energies. Throughout the investigation of this phenomenon, various and classifications of sputtering have been proposed. The three main categories concerning erosion in tokamaks are physical sputtering, chemical sputtering, and potential sputtering. The definitions are listed below.

1. **Physical sputtering** is a process by which atoms or molecules are removed from a solid surface due to the impact of energetic particles, such as high-energy ions or atoms [28]. In a tokamak, this process occurs because of plasma particles and impurities acceleration toward the plasma-facing materials (PFMs) under the effect of the sheath and scrape-off layer (SOL) electric field.

2. **Chemical sputtering** is defined as “a process whereby ion bombardment causes or allows a chemical reaction to occur which produces a particle that is weakly

bound to the surface and hence easily desorbed into the gas phase", see [29] and reference therein.

3. **Potential sputtering** is an ion-induced sputtering due to the potential energy liberated by highly charged ions (HCI) recombining in a solid material [30].

Due to the wide range of chemical and physical reactions involved both within the solid material and the plasma, attempting to quantify sputtering for every material presents a formidable challenge, lying beyond the scope of this study. The primary focus will be directed toward the erosion of monoatomic polycrystalline tungsten (W) or polycrystalline W with a low impurity content such that the principle of superposition is valid. For such solid materials, physical sputtering is arguably the predominant phenomenon. Potential sputtering was detected only for insulators [30], whilst W chemical reactivity is low if compared to other PFMs [31]. Nevertheless, both chemical and potential sputtering can have a non-negligible impact during the transitional phases between consecutive plasma discharges. It is common knowledge that tungsten oxidizes under standard atmospheric conditions [32] and oxidized layers might be subjected to potential sputtering. Additionally, there is evidence showing that the physical sputtering of tungsten is chemically assisted by the production of compounds at the solid surface such as tungsten deuteride (WD) [33]. Newly formed molecules have lower binding energy and even a small momentum exchange can provoke dislocation and sputtering. Further phenomena of material removal are related to temperature, phase changes [18], and mechanical stresses. Finally sputtering is also influenced by macroscopic properties of the material: the presence of helium bubbles accompanied by the creation of the so-called W fuzz [34], surface roughness [35] etc... all cooperate to the final amount of the eroded particles. Since physical sputtering is the predominant cause of W erosion, this thesis will exclusively address and examine this type of sputtering.

1.1.1 Physical sputtering

This section presents a summary of physical sputtering starting from the theoretical foundations to today's applications. Physical sputtering is a phenomenon of particle removal from a solid material caused by the impact between incident ions and the atoms of the material. Depending on the impact energy, three physical sputtering regimes are described [28]. As shown in figure 1.1 if the impact energy causes displacements of the target atoms but they do not have enough energy to cause other displacements then the sputtering is in a single knock-on regime. For higher incident energies released target atoms set other atoms in motion provoking a cascade of collisions. The cascade is linear if displaced atoms' mutual interactions are unlikely, otherwise, sputtering produces a local vaporization also called spike.

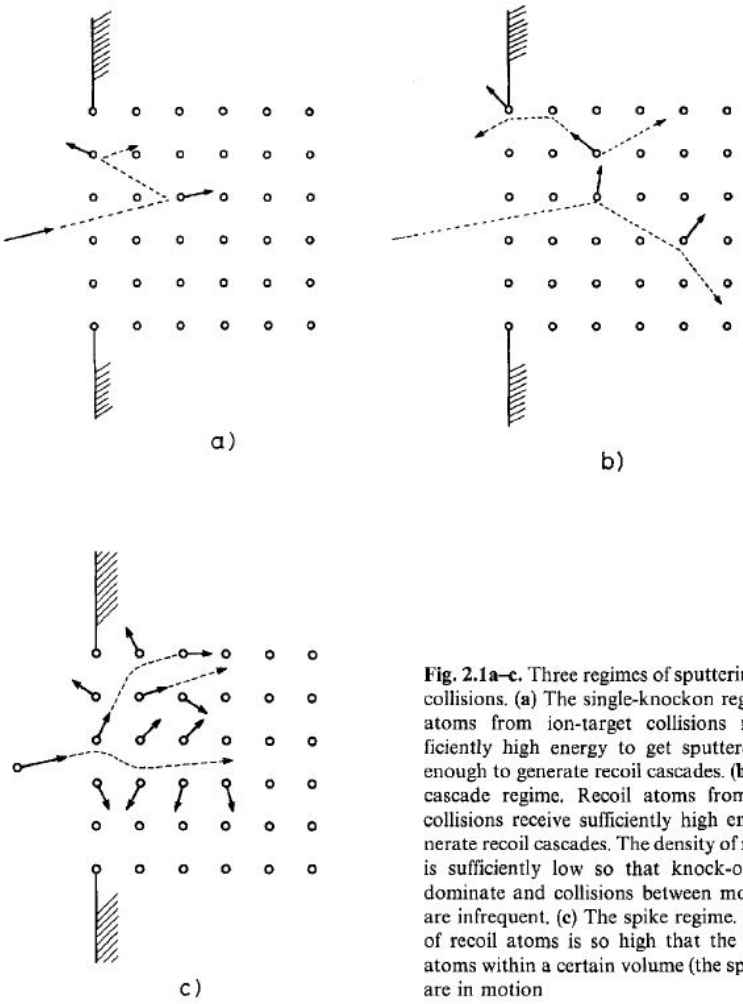

Fig. 2.1a–c. Three regimes of sputtering by elastic collisions. **(a)** The single-knockon regime. Recoil atoms from ion-target collisions receive sufficiently high energy to get sputtered, but not enough to generate recoil cascades. **(b)** The linear cascade regime. Recoil atoms from ion-target collisions receive sufficiently high energy to generate recoil cascades. The density of recoil atoms is sufficiently low so that knock-on collisions dominate and collisions between moving atoms are infrequent. **(c)** The spike regime. The density of recoil atoms is so high that the majority of atoms within a certain volume (the spike volume) are in motion

Figure 1.1: Possible physical sputtering regimes, image adapted from [28]

Multiple collision processes like these are typically addressed within the framework of transport theory. In our specific scenario, the Boltzmann equation is used since most of the particles moving inside the materials are in a neutral medium. A first analytical approximation of physical sputtering based on such equation and further approximations is proposed in [28] for each regime previously cited. To get a glimpse of what has been done, the analytical treatment of sputtering in the linear cascade regime is here shown. The working assumptions are the following: no external forces acting on particles between collisions, target atoms are at rest before impact. In such conditions the volume distribution of all particles (both impinging and eroded) can be linearized as here shown, equation (1.1).

$$f(\mathbf{r},\mathbf{v},t) = N\delta(\mathbf{v}_1) + F(\mathbf{r},\mathbf{v},t) \tag{1.1}$$

N is the target density, $f(\mathbf{r},\mathbf{v},t)$ is the distribution in velocity and position at time t and $F(\mathbf{r},\mathbf{v},t)$ is a small perturbation. The particle distribution is considered to be

piqued at the initial velocity $\mathbf{v}_1$ of target particles and varies slightly as $F(\mathbf{r},\mathbf{v},t)$ due to the presence of colliding impinging ions and displaced atoms. This linearization procedure is strictly suitable for the linear cascade regime, and the resulting transport equation (1.2) is here reported.

$$-\left(\frac{\partial}{\partial t}+\mathbf{v}\cdot\nabla_r\right)F(\mathbf{r},\mathbf{v},t)=N\int d^3v'd^3v''(vFK(\mathbf{v};\mathbf{v}',\mathbf{v}'') - v'F'K(\mathbf{v}';\mathbf{v},\mathbf{v}'')-v''F''K(\mathbf{v}'';\mathbf{v}',\mathbf{v})) \quad (1.2)$$

$\mathbf{v}$,$\mathbf{v}'$ are the incident ion velocities before and after impact and $\mathbf{v}_1$,$\mathbf{v}''$ are the target velocities before and after impact, respectively. $K(\mathbf{v},\mathbf{v}_1;\mathbf{v}',\mathbf{v}'')$ is the differential cross section for an incident particle with velocity $\mathbf{v}$ impacting a target with velocity $\mathbf{v}_1$ whose resulting velocities after the impact are $\mathbf{v}'$ and $\mathbf{v}''$, respectively. Since $\mathbf{v}_1=0$ it was omitted in equation 1.2.
The analytical theory based on the equation (1.2) has provided a better understanding of physical sputtering and resulted in the first formulation of physical sputtering yield. In general, the sputtering yield is defined as the average number of sputtered particles per incident particle.

$$Y=\frac{mean\ sputtered\ particles}{incident\ particles} \quad (1.3)$$

According to linear cascade theory physical sputtering yield is the product between a function of the material properties Λ and the deposited energy F_D by incident ions [28].

$$Y=\Lambda F_D \quad (1.4)$$

Moreover, the deposited energy F_D is directly proportional to the nuclear stopping cross section $S_n(E_0)$, multiplied by a function q of the projectile-target mass ratio.

$$F_D\propto qS_n(E_0) \quad (1.5)$$

The nuclear stopping cross section $S_n(E_0)$ is defined as the average energy transferred times unit area. It is used to calculate $\overline{\Delta E_0}$ the average energy spent in collisions along a distance x in a material of density N.

$$\overline{\Delta E_0}=Nx\int d\sigma(E_0,T)\cdot T\equiv NxS_n(E_0). \quad (1.6)$$

In turn, q and $S_n(E_0)$ depend on the differential impact cross-section $d\sigma$ considered. For elastic collisions where the interatomic potential is in the form $V(R)\propto R^{-1/m}$ in which R is the distance to the nucleus and m is a dimensionless collision parameter (e.g. $m=0$, rigid spheres); $d\sigma$ takes the form expressed in equation (1.7).

$$d\sigma(E_0,T) \simeq \begin{cases} C_m E_0^{-m} T^{-1-m}, & \text{if } \epsilon \lesssim 1 \\ \pi \frac{M_1}{M_2} Z_1^2 Z_2^2 e^4 \frac{dT}{E_0 T^2}, & \text{otherwise} \end{cases} \tag{1.7}$$

The cross-section in equation (1.7) describes the probability a projectile particle of mass M_1 and nuclear charge $Z_1 e$ has to transfer an amount of energy T to a target particle with mass M_2 and nuclear charge $Z_2 e$, provided an impact energy E_0. The collision is approximated as neutral and between rigid bodies if the reduced energy ϵ, that is the impact energy E_0 normalized with respect to the Thomas-Fermi energy E_{TF}, is less than 1. Otherwise, the Coulomb screening can't be neglected. Indeed, even if the medium is macroscopically neutral, there is still an interatomic potential affecting moving charged particles. In the case of rigid impact the cross section depends on the adimensionless parameter m, the constant C_m, the energy before impact E_0 and the transferred energy T. On the other case, the cross section depends on nuclear charges. Another important quantity is the maximum transferable energy T_m, which is limited by the max energy transfer factor γ.

$$T_m = \gamma E_0 \equiv \frac{4 M_1 M_2}{(M_1 + M_2)^2} E_0 \tag{1.8}$$

The stopping cross section introduced in equation (1.6), is normally expressed as an analytical fitting function of the reduced energy, denoted as $s_n(\epsilon)$. The fit result depends on the screened Coulomb interaction considered [36].
Concerning the function material Λ, it is a function of the material surface binding energy E_b or the minimum energy required to escape from the solid. Normally, it is assumed that the binding energy is equal to the sublimation energy $E_b \approx E_s$ which in reality is not always the case [37] . The sputtering yield approximation, equation 1.4, is known to not always be accurate. The resume here proposed about the linear cascade theory is limited and can't be applied universally. For instance, when the mass ratio M_2/M_1 is very large or for impinging particle with grazing incidence angles, the theory breaks down [28]. In addition, the sputtering behavior close to the energy threshold E_{th} is not treated by the former analyses. It was added later in [38] at least for sputtering induced by incident particles impacting perpendicular to the eroded surface.
Since an analytical approach is not always suitable, particle transport was solved numerically. Binary Collision Approximation (BCA) codes such as TRIM (TRansport of Ions in Matter) [39] were deployed to produce numerical sputtering yield databases. The abundance of available data allowed to expand the range of validity of the analytical formula proposed by Sigmund [28]. Bohdansky in [38] proposed a correction term for the stopping cross section $S_n(E_0)$ including sputtering induced by particles with impact energies close to the threshold energy E_{th}, see equation (1.9). The validity of this modification, however, applies only to perpendicular bombardment.

$$Y(E_0, \alpha = 0^\circ) = Q s_n(\epsilon) \left[1 - \left(\frac{E_{th}}{E_0}\right)^{2/3}\right] \left[1 - \frac{E_{th}}{E_0}\right]^2 \tag{1.9}$$

Where Q is a constant used to fit sputtering data. The limit for $E_0 \to \infty$ of the equation (1.9) coincides with the equation (1.4). In [40] it was shown that the sputtering yield could be expressed as the one shown by Bohdansky for perpendicular incidence angle multiplied by a function of the impact angle, denoted as α. The new formula Bohdansky-Yamamura was born, see equation (1.10).

$$Y(E_0,\alpha) = Y(E_0,\alpha = 0^\circ)(cos(\alpha))^{-f} exp\left(f\left[1-(cos\alpha)^{-1}\right]cos(\alpha_{opt})\right) \tag{1.10}$$

In equation (1.10) f and α_{opt} are fitting parameters; α_{opt} is the angle of maximum sputtering. A variant of the sputtering yield from Bohdansky-Yamamura was advanced by [36], where the discrepancy between a larger database and prediction was reduced by applying a few refinements. The Thomas-Fermi cross-section $s_n^{TF}(\epsilon)$ used in the past was replaced with the KrC one $s_n^{KrC}(\epsilon)$, new formulas and data about the energy threshold, the parameter Q, and α_{opt} were proposed. An example of the sputtering yield is shown in figure 1.2 Further data collection showed the occurrence of sputtering yield greater than zero even for energy below the sputtering threshold predicted by previous formulas, so a new fit was published by [41]. This advancement differs profoundly from the past because the deposited energy function F_D was modified again and the parameters λ, μ, b, c, α_0 were added, which (except α_0) are determined by Bayesian probability theory applied to numerical and experimental databases.

$$Y(E_0,\alpha = 0^\circ) = q s_n^{KrC}(\epsilon)\frac{\left(\frac{E_0}{E_{th}}-1\right)^{\mu}}{\lambda+\left(\frac{E_0}{E_{th}}-1\right)^{\mu}} \tag{1.11}$$

$$Y(E_0,\alpha) = Y(E,\alpha = 0^\circ)\left\{cos\left[\left(\frac{\alpha}{\alpha_0}\frac{\pi}{2}\right)\right]^{c}\right\}^{-f} exp\left\{b\left(1-1\Big/cos\left[\left(\frac{\alpha}{\alpha_0}\frac{\pi}{2}\right)\right]^{c}\right)\right\} \tag{1.12}$$

Henceforth, whenever "sputtering" is mentioned in the context of this thesis, it specifically refers to physical sputtering, with a focus on tungsten as the target material.

1.1.2 Reflections and evolution of eroded surfaces

Not all incident particles enter and remain trapped in the target material. Some particles can be backscattered or reflected, meaning they return to the plasma after a series of collisions within the PFCs. From a macroscopic point of view, reflection happens at one point as shown in figure 1.3. In reality, because of collisions, the backscattering angle differs from the initial one. Reflected particles can still sputter because they still exchange some of their initial energy through collisions [42]. Consequently, in sputtering theory, each incident particle with energy E_0 and angle α is characterized by the probability of reflection and by their energy after reflection. For a monoenergetic beam of incident particles with energy E_0 and angle α, two reflection coefficients are established, denoted as R_N and R_E.

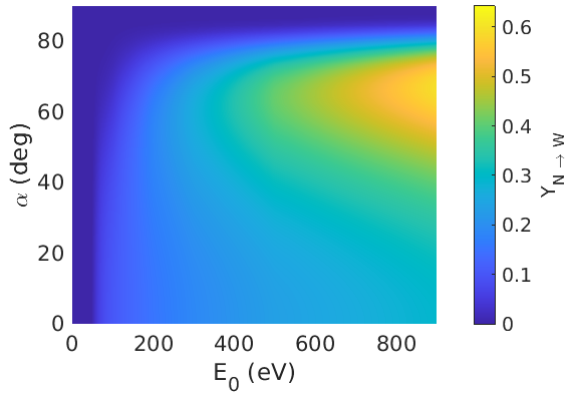

Figure 1.2: Sputtering yield of Nitrogen N on Tungsten W from [41] with respect to angle α and energy E_0 of incidence.

$$R_N(E_0, \alpha, m_i/m_t) = \frac{N}{N_0} \tag{1.13}$$

$$R_E(E_0, \alpha, m_i/m_t) = \frac{N}{N_0}\frac{\overline{E}(E_0, \alpha, m_i/m_t)}{E_0} \tag{1.14}$$

R_N is the average probability of reflection and is equal to the number of reflected particles N divided by the number of incident particles N_0. At the same time R_E is the fraction of reflected energy and is equal to the average reflected energy $\overline{E}$ divided by the incident energy E_0. From the equations (1.13) (1.14) the two coefficients are related

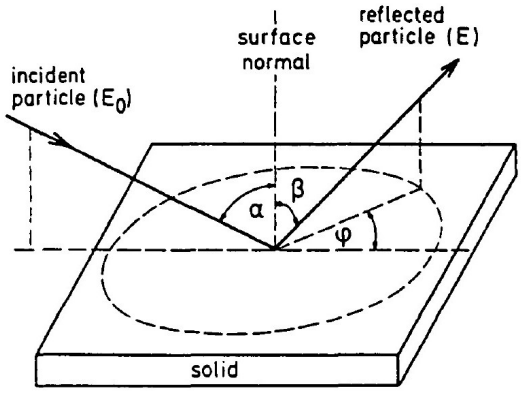

Figure 1.3: Sketch of reflection adapted from [42]

to each other by the relation $R_E = R_N\overline{E}/E_0$. In [42], it is shown that the reflection probability is inversely proportional to E_0 and the mass ratio m_i/m_t between incident and target particles. This is because, the higher E_0, the higher the chance a particle will collide in depth inside the material and implant ($1 - R_N$ is the fraction of implanted

particles). On the other hand, if the mass ratio is small the momentum exchange is less efficient, and more collisions are needed to slow down the incident particle. Similarly as in the previous chapter 1.1.1 practical expressions of the reflection coefficients come from calculated databases retrieved both experimentally (e.g., calorimetric techniques) and numerically (e.g., BCA codes). In some cases, like in the 3D fully-kinetic source and impurity transport code ERO2.0 [22], it is preferred to use databases directly.

It appears from the above that the sputtering yield decreases if reflections are considered. Equation (1.15) shows how reflection coefficients affect sputtering given a fixed mass ratio m_i/m_t.

$$Y(E_0,\alpha) = Y(E_0,\alpha)(1-R_N(E_0,\alpha)) + Y(E_0(1-R_E(E_0,\alpha)),\alpha))R_N(E_0,\alpha) \tag{1.15}$$

The implanted fraction will sputter releasing its whole initial energy E_0, while the reflected fraction will sputter less retaining a part of it. At this point, the following question may arise: what happens to the implanted particles, and how do they change the properties of the material with which they mix? First of all, it should be kept in mind that the range of ions inside dense materials such as tungsten is in the order of the nanometers, see figure 1.4 for an example. Hence the mixing will mostly affect the outermost layer of the target material. According to the **H**omogeneous **M**ixing surface **M**odel (HMM) [43] , [44], the implantation of carbon in tungsten occurs in a layer of thickness $\Delta \approx 3\ nm$ called the implantation layer, while the bulk material underneath remains unaffected. Plasma ions and impurities can either saturate the implantation layer (deposition regime) or reach an equilibrium where a fraction of the bulk material is still present (erosion regime). The resulting sputtering yield should take into account the fact that only a fraction of the eroded particles is bulk material. Once the bombardment is over, the original concentration at the implantation layer can be recovered. Well-known wall conditioning techniques, such as baking [45] are currently used to artificially enhance the desorption of impurities. Finally, ionic bombardment changes the morphology of the eroded material, for instance by promoting roughness if done in an uncontrolled manner [46], [47].

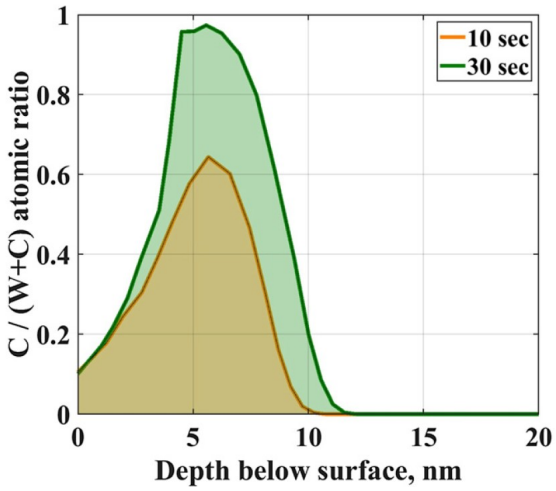

Figure 1.4: Evolution of carbon concentration in tungsten at the small angle slot (SAS) divertor of DIII-D, equilibrium is reached after 30 seconds [48].

1.2 Plasma sheath

When a solid object, such as a probe or a tokamak wall, comes in contact with a plasma, it becomes exposed to a stream of charged particles, such as electrons and ions, that make up the plasma. Electrons due to their high thermal velocity reach the object and begin charging it negatively before ions can counteract this effect. At the end of the transitional phase, if the object is isolated (or floating) and no external potential is applied, impinging electron and ion fluxes are equal, thereby the object maintains the negative charge initially imparted by electrons. The plasma in direct contact with the object will adjust its charge to shield the object's negative potential. As a consequence, a layer with a width on the order of the Debye length λ_D will develop. Within this layer, known as the plasma Debye sheath (DS), the principle of quasi-neutrality is no longer respected. For this reason, the plasma volume is divided into two regions: a region where quasi-neutrality holds $n_e = \sum_i n_i Z_i$ which is the main body of the plasma, and a region of net charge $n_e < \sum_i n_i Z_i$, which is called the Debye sheath. The ionic density in the Debye sheath is larger compared to electron density because plasma is positively charged to shield the negative charge of the confining body. The decrease in electron density within the Debye sheath is connected to the electric potential ϕ within the sheath, and this relationship is governed by the well-known Boltzmann factor [49]. Due to its theoretical significance and its relevance to the thesis work, a concise overview of the Boltzmann factor is provided here. The assumptions employed in deriving this factor are outlined below.

1. electron thermal velocity $\overline{c_e} \gg c_s$ much greater than the speed of sound of the plasma

2. Noncollisional Debye sheath

3. Maxwellian electron distribution at the entrance of the Debye sheath

In this framework, the Boltzmann factor is derived from a one-dimensional case. Let us consider a one-dimensional plasma flowing in the sheath along the spatial direction z perpendicular to the surface material. The one-dimensional maxwellian velocity distribution along z is denoted as $f(v)$. From the flux conservation in the sheath, the following relation holds.

$$f(v)\,v\,dv = g(v')\,v'\,dv' \tag{1.16}$$

Where $g(v')$ is the electron distribution at the generic position z in the sheath. The velocity v', is in turn derived from the energy balance.

$$v'^2 = v^2 - \frac{2e\Delta\phi}{m_e} \tag{1.17}$$

From equations (1.16) (1.17), it follows that the velocity distribution is conserved i.e. $f(v) = g(v')$. Since it is assumed that the velocity distribution $f(v)$ is Maxwellian it results that the velocity distribution in the sheath g is equal to the distribution at the entrance sheath $f(v)$, i.e., where the plasma is unperturbed and the potential is nearly zero, multiplied by an exponential. The exponential carried over to the equation (1.18) is the so-called Boltzmann factor.

$$g(v') = f(v')exp\left(-\frac{\Delta\phi}{T_e^{SE}}\right) \tag{1.18}$$

Integrating the equation (1.18) with respect to v' yields the electron density drop $n_e(z)$ in the sheath.

$$n_e(z) = n_e^{SE}exp\left(-\frac{\Delta\phi}{T_e^{SE}}\right) \tag{1.19}$$

While the electron temperature of the plasma is considered constant and independent of the potential. As for ions, the density $n_i(z)$ is obtained from flux conservation.

$$n_i(z) = \frac{n_e^{SE}c_s}{v'} \tag{1.20}$$

$$v'^2 = v^2 + \frac{2e\Delta\phi(z)}{m_i} \tag{1.21}$$

Once ionic and electron densities are known, the Poisson's equation is used to define the potential drop ϕ inside the Debye sheath. Expanding the Poisson equation to the second order in a Taylor series reveals that as ϕ approaches zero, the ion velocity must be greater than or equal to the speed of sound, denoted as $v_z \geq c_s$. This condition causes $n_i > n_e$ in the Debye sheath hence a shielding of the negative potential to be present, without necessarily implying ϕ monotony [50]. Certainly, this asymptotic treatment is idealistic and cannot be extended to the undisturbed plasma, where the

leading equations break down. Additionally, ions undergo acceleration before entering the Debye sheath, resulting in the presence of an electric field in the quasi-neutral region outside it.

1.2.1 Presheath

The quasi-neutral plasma preceding the Debye sheath is divided into various layers. The region where ion inertia is comparatively smaller than the electric field acceleration is termed the 'presheath.' Despite the existence of a potential drop, the plasma remains quasi-neutral due to the larger characteristic length in comparison to λ_D. The presheath may exhibit collisional and/or ionizing behavior and encompasses the so-called 'magnetic presheath' (MPS) or 'Chodura sheath' (CS) as described by Chodura in 1986 [51], where the velocity parallel to the magnetic field B is converted to a velocity perpendicular to the wall. Chodura postulated a second condition for supersonic flows, namely in the presence of a magnetic field $\vec{B}$ the ion velocity has to be greater or equal to sonic flow along magnetic field lines ($v_\parallel \geq c_s$) at the Chodura sheath entrance. An additional layer adjacent to the negative surface is the Knudsen layer (KL) [52]. The width of this layer varies depending on plasma collisionality. When collisionality is high, it overlaps with both the Debye sheath and a portion of the Chodura sheath. However, when collisionality is low, it extends including even a section of the boundary plasma (also called far SOL). In the Knudsen layer collisions are negligible and the kinetic distortion of plasma ions and impurities is predominant, justifying non-Maxwellian distributions at the surface and/or at the presheath entrance. For this reason, as will be shown later in chapter 2.2.1 a Maxwellian distribution corresponding to high collisionality, thus a Knudsen layer smaller than magnetic presheath, was compared with a Gamma distribution representing low collisionality, thus a Knudsen layer larger than magnetic presheath. To resume, the presheath features are: quasi-neutrality and the predominance of the electric acceleration over inertia. It includes the magnetic presheath and part or all the Knudsen layer. The boundary between the Debye sheath and the presheath is called the sheath edge (SE) or Debye sheath entrance (DSE) according to Langmuir's definition [53]. Since the transition is smooth the sheath edge position is not uniquely defined [54] and it is here assumed that its position coincides with the first point where the Bohm criterion is respected, ($v_i = c_s$). Again, the definition of magnetic presheath entrance (MPSE) faces the same issue related to continuity and for the sake of this work, it is assumed that it coincides with the point where the Chodura sheath criterion is respected ($v_z = c_s$). The last boundary before the SOL is the presheath entrance (or PSE) where a potential drop is still present to accelerate particles in the parallel direction up to the sound speed. A clear definition of the PSE position is not yet formalized, it should be where the potential drop is negligible compared to ions inertia. Unfortunately, the Chodura sheath plus the Debye sheath is sometimes referred to in the literature as 'sheath' [49], [55] creating confusion. This categorization is used to separate the domain where quasi-neutral plasma can be modeled with fluid equations with respect to the sheath and presheath where the fluid solution transitions to singularity. This does not mean

that the quasi-neutral presheath cannot be modeled with fluid equations [56], but in those cases where the fluid solvers don't solve the MPS, it makes sense to gather MPS and Debye sheath in a separate group, even if the terminology is confusing. Since throughout this thesis the Debye sheath and the magnetic presheath are assumed as a single block, their combination will be referred to as 'sheath'. In addition, quantities at the MPSE are assumed approximately equal to those at the PSE resulting for instance in $n_e^{PSE} \approx n_e^{MPSE} \equiv n_e^{SE}$. A sketch representing the 1D structure of the presheath plus Debye sheath is shown in figure 1.5.

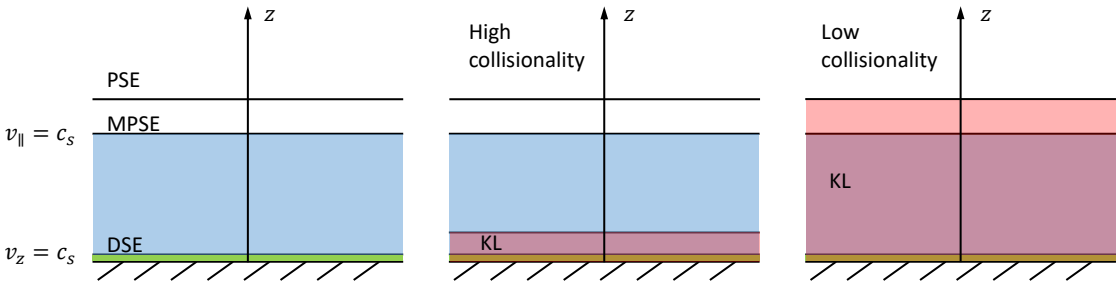

Figure 1.5: Sketch of different layers composing the plasma-sheath in the proximity of a solid surface. DSE, MPSE, and PSE are the entrances of the Debye Sheath (green) Magnetic presheath (light blue), and presheath (white). KL is the Knudsen layer (red) and it is shown for low and high collisionality cases.

A model of the potential drop inside the DS and MPS is proposed in [57], [58] [59] where the MPS potential drop is approximated with an exponential decay. The remaining potential drop before the MPSE is included by using the formula proposed in [60]. As shown in [49] the total potential drop in the case of electrically floating material V_{sf} is shared between the DS and the MPS according to the simple relation.

$$V_{sf} - V_{MPSE} = V_{DS} + V_{MPS} \tag{1.22}$$

This implies that the electron density measured by Langmuir Probes at the DSE n_e^{DSE} is not equal to n_e^{MPSE}. If the MPS is collisionless and continuity is valid then the relation between those two densities is simply related to the magnetic angle of incidence α_B [61].

$$n_e^{MPSE} = \frac{n_e^{DSE}}{sin(\alpha_B)} \tag{1.23}$$

Equation (1.23) is valid if $\alpha_B \gtrsim 1\ deg$ that's because for very small grazing angles plasma ions are not magnetized inside the MPS and the physical model applied break. According to fluid models, the potential drop inside the MPS is strictly related to α_B while the total drop doesn't depend on it.

$$V_{MPS} = log(sin(\alpha_B)) \tag{1.24}$$

According to equation (1.24) there is a critical angle α_B^* below which $V_{sf} = V_{MPS}$

implying the disappearance of the Debye Sheath [62]. Variations of the total potential drop can either eliminate or enlarge the Debye sheath. Figure 1.6 shows a series of one-dimensional profiles of potential drop in the sheath as a function of the distance perpendicular to the solid surface z. The profiles are calculated for a plasma in steady state and without fluctuations [58]. The potential drop can be changed by the application of an external potential (or bias) to the surface. The effect of a constant bias in direct current (DC bias) is illustrated in figure 1.6. The application of a voltage is the basis for the operation of one of the measuring instruments used in tokamaks: the Langmuir Probes, which will be discussed in the following chapter.

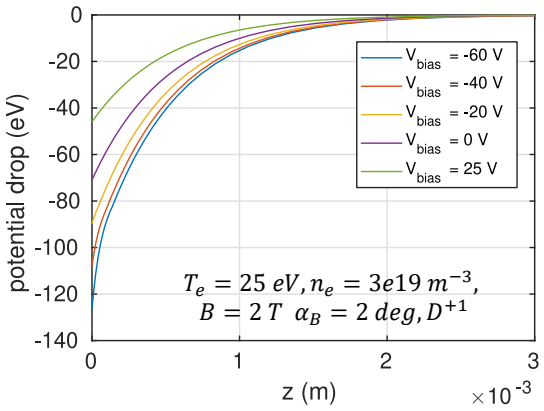

Figure 1.6: The 1D electric potential drop in the sheath is depicted as a function of the distance perpendicular to the solid surface (z) and the DC bias. The calculations are conducted using the formula proposed in [58] imposing the sheath width equal to 2 times the deuterium Larmor radius. The presented results pertain to a pure deuterium plasma. Temperature and electron density conditions at the sheath entrance, along with the magnetic field configuration, are specified in the graph.

1.3 Langmuir Probes

In this chapter, the unmagnetized theory of Langmuir Probes will be briefly discussed. For further details, it is suggested to look into [49] and references therein. The aim here is to explain why the DiMES system [63] used to study sputtering as a function of a DC voltage in chapter 4.1, is comparable to a single flush mounted Langmuir Probe (LP).
Langmuir Probes are essentially metallic rods plunged into a plasma and measuring a current. A solid material immersed into a plasma receives a current only if the electron and ionic fluxes differ ($\Gamma^e \neq \Gamma^i$). This occurs when the solid material in contact with the plasma is not electrically floating with the rest of the machine. Despite Langmuir Probes being electrically linked to the machine vessel, their potential is altered through an external voltage (or bias) allowing a net current to flow into the probe. The voltage is applied via a power generator controlling the LP potential with the specific intention

of retrieving a characteristic current signal as a function of the applied voltage called $I-V$ characteristic. This characteristic is employed to infer plasma quantities such as T_e or n_e at the LP location. The simplest LP design is the so-called single Langmuir Probe, it consists of a single metallic rod connected to a voltage or power generator whose potential is controlled with an input time signal. The reference potential is the machine potential (or V_{return}). The disadvantage related to the single configuration is that V_{return} changes to accommodate the introduced bias. Because of that the $I-V$ characteristic interpretation for the single LP is complicated. The V_{return} variation depends on the ratio between the LP collecting area (A_{LP}) and the current area of return into the vessel (A_{RT}). Indeed, without ambipolarity the induced current travels through the plasma before returning back into the unbiased vessel. In unmagnetized plasma, the current spreads causing $A_{RT} \gg A_{LP}$ and it is reasonable to think that V_{return} is almost insensible to the single LP potential. However, in the presence of a magnetic field currents may follow preferential paths reducing the return area. Anyway, as stated in [49] the standard approach is to consider $B = 0$ and to assume that $V_{return} \approx V_{sf}$ and constant. According to this approximation, the bias V_{bias} can be summed to the floating potential resulting in $V_{LP} = V_{sf} + V_{bias}$ with respect to plasma potential, again, $V_{LP} = V_{bias}$ with respect to the machine potential. Just for the record, the more expensive LP design called double LP, avoid this issue by relating V_{return} to a second identical LP.

1.4 Erosion

1.4.1 Gross erosion

In a plasma device, components facing the plasma are subjected to erosion. Each exposed component is called **P**lasma **F**acing **C**omponent or PFC and similarly, each exposed material is called **P**lasma **F**acing **M**aterial (PFM). If the sputtering regime is linear, for any given couple of incident and target species (s_i, s_t) the effective mean amount of sputtered particles per incident particle denoted as effective sputtering yield $\overline{Y}$ (see equation 1.25) is strictly given by the integration of the sputtering yield $Y_{s_i \to s_t}(E_0, \alpha)$ times the **I**mpact **E**nergy and **A**ngular **D**istribution $IEAD_{s_i}(E_0, \alpha)$ of the impinging species. As shown in equation(1.26) the $IEAD$ is the impacting species' probability density function in energy and angle at the target position $\mathbf{x}_t$.

$$\overline{Y}_{s_i \to s_t} = \int\int Y_{s_i \to s_t}(E_0, \alpha) IEAD_{s_i}(E_0, \alpha) dE_0 d\alpha \tag{1.25}$$

$$IEAD \equiv \frac{f(\mathbf{x}_t, E_0, \alpha)}{\int\int f(\mathbf{x}_t, E_0, \alpha) dE_0 d\alpha} \tag{1.26}$$

Finally, the effective sputtering yield times the incident flux is the total (also called gross) eroded flux Γ_{gross} from the surface because of the bombardment from the species s_i. In most cases, plasma can consist of various species, each one with a different concentration c_i such that $\sum_i c_i = 1$. Given a certain total incident flux Γ_{inc},

the combined or total contribution of these species to Γ_{gross} is expressed as follows.

$$\Gamma_{gross} = \Gamma_{inc} \sum_i c_i \overline{Y}_{s_i \rightarrow s_t} \tag{1.27}$$

From equation(1.27) it follows that two essential quantities needed to correctly assess Γ_{gross} are the concentrations of impurities and plasma species (per charge state) and the Incident Energy Angle Distribution IEAD associated with each of them. While to date species concentrations are still unknown and left as an input parameter, the IEAD has been extensively studied both experimentally, [64], [65], and through numerous theoretical and numerical works [66] [67] [68]. Generally, the energy distribution at the sheath entrance is approximated with a half-Maxwellian distribution accelerated within the Debye sheath [69], or within the Debye and Chodura sheaths [70], both assumed non-collisional. The presence of collisions in the sheath is typically negligible unless the magnetic field intensity is relatively small [66]. The effect of collisions in the sheath is to demagnetize the incident particles increasing the population of particles with incident angles perpendicular to the wall. Finally, the IEAD can be influenced by applying a voltage that modifies the potential drop in the sheath and by modulating the magnetic field. For time-varying sinusoidal potentials, the incident distribution exhibits two peaks in energy corresponding to the maxima and minima. In [68], the IEAD was calculated in front of ICRH antennas where a non-static radio frequency (RF) sheath is present.

1.4.2 Net erosion

Initially, sputtered particles are neutral, then they are ionized as a result of electron excitation. Subsequently, following a short period of neutrality, these particles experience electromagnetic forces. The electric field within the sheath exerts a force that directs some of the sputtered particles back toward the wall. Typically, as a surface expels particles, it simultaneously recaptures a portion of them. This concept gives rise to the definition of net flux, calculated as the outward flux of sputtered particles minus the inward flux. In a broader context, if each PFC is an erosion source, the inward flux associated with each of them equals the portion of the gross flux that undergoes **redeposition** f_{redep}, in addition to the fraction of flux f_{dep} originating from other sources and subsequently **deposited** onto the specific surface under examination. In a system with N_c PFCs, the net flux for each source j is defined as follows.

$$\Gamma^j_{net} = \Gamma^j_{gross} - \left(\Gamma^j_{gross} f^j_{redep} + \sum_{i \neq j}^{N_c} \Gamma^j_{gross} (1 - f^i_{redep}) f^{ij}_{dep} \right) \tag{1.28}$$

In equation (1.28) the inward flux is the second term between parenthesis. It is interesting to note that to calculate the mutual deposition term (the summation in equation (1.28)) it would theoretically be necessary to solve the transport of eroded particles throughout the whole plasma domain, as done in codes such as ERO2.0 [22] and GITR [23]. Conversely, the redeposition term predominantly accounts for

transport taking place within the plasma sheath, encompassing a relatively confined region of the plasma near the solid material, typically extending on the order of the first ionization Larmor radius of the sputtered species. If the separation distance between sources is significantly greater than the first ionization Larmor radius, it becomes feasible to differentiate between localized redeposition and mutual deposition.
As mentioned in section 0.3, the main objective of the thesis is to provide a source term that can be used in conjunction with fluid codes such as SolEdge [71] and SOLPS [72] to simulate plasma transport and mutual deposition in a fluid manner. Therefore, within the scope of the thesis, the net flux is approximated as a local phenomenon and is thus equal to the gross flux multiplied by the fraction of particles not locally redeposited.

$$\Gamma^{j}_{net} \approx \Gamma^{j}_{gross}(1 - f^{j}_{redep}) \tag{1.29}$$

2 Monte Carlo modelling of local erosion and redeposition

Sommaire

2.1 Definitions and context . . . 35
2.1.1 Energy of sputtered ions . . . 35
2.2 Sheath model employed . . . 36
2.2.1 Boundary condition - distributions at the Sheath Entrance . . . 38
2.2.2 W erosion and redeposition . . . 39
2.2.2.1 Neutral W transport . . . 40
2.3 Monte Carlo simulation . . . 41
2.3.1 Numerical setup . . . 42
2.3.2 Model validation . . . 44
2.4 Results . . . 45
2.4.1 Neutral W non redeposition dependence on plasma parameters and boundary conditions . . . 45
2.4.1.1 Probability distributions of non redeposition and cone of loss . . . 47
2.4.1.2 Magnetic field configuration influence on W redeposition 50
2.4.2 Effective sputtering yield . . . 51
2.4.2.1 IEAD, the Impact Energy and Angular Distribution . . . 52
2.4.3 Plasma ions erosion - Deuterium . . . 53
2.4.4 Potential drop model uncertainty . . . 54
2.5 Discussion . . . 55

In the following chapter, the model employed for computing local erosion and redeposition is introduced. The majority of the details are derived from the corresponding paper [73]. Monte Carlo techniques are employed to determine the redeposited fraction f_{redep} defined in the previous section 1.4.2. The principal innovation shown in this chapter lies in the incorporation of an analytical model to obtain a more accurate distribution of sputtered neutrals. This refinement, compared to prior literature, involves considering the entire energy distribution of incident particles instead of employing an averaged approach, as will be elucidated later in the text.

2.1 Definitions and context

As introduced in Chapter 1.4.2, a portion of the gross sputtered flux does not enter the plasma, redepositing on its original surface. Redeposition pertains to the transport of particles within a confined volume approximately equal to the Larmor radius of the plasma species, encompassing the plasma sheath and its immediate vicinity. Over time, various definitions of redeposition have emerged. The first, proposed in [74], views redeposition as limited to the first gyroperiod of sputtered ions, depending solely on the gyromotion of the sputtered ions. The fraction of particles redepositing before the gyroperiod is denoted as the promptly redeposited fraction f_p (non-prompt fraction being $f_{np} = 1 - f_p$). It is used to adjust the sputtering yield, redefined as the 'net' sputtering yield, leading to a distinction between the gross flux $\Gamma_{gross} = \Gamma_{inc} \times \overline{Y}$ (equal to the incident flux Γ_{inc} times the effective sputtering yield) and the net flux $\Gamma_{net} = \Gamma_{gross} \times f_{np}$. However, [75] demonstrated that the definition of f_{np} in [74] was inaccurate for high-Z plasma-facing materials (PFMs). Specifically, through a set of local Monte Carlo simulations, they observed that while the characteristic redeposition time is indeed the Larmor period of the sputtered ion, f_{np} is significantly overestimated without considering the effect of the plasma sheath electric field. Consequently, in [75], the fraction of redeposited particles was redefined from 'prompt redeposition' to 'total-redeposition' (with relative fraction denoted as f_{redep}). According to this new definition, particles are considered redeposited if they reach the wall or if their parallel to magnetic field velocity is directed towards a wall or their energy is smaller than the potential barrier where they fall after one Larmor period. Furthermore, in [76], similar Monte Carlo simulations to those in [75] were conducted. However, the simulation times were extended to more accurately evaluate the overall quantity of particles undergoing redeposition. In this study, the fraction $f_{non-redep} = 1 - f_{redep}$ calculated using the prolonged Monte Carlo simulations is the considered output.

2.1.1 Energy of sputtered ions

In the presented set of simulations, a new analytical model is introduced to provide a more precise estimation of the energy distribution of sputtered ions. Accurately characterizing the energy distribution of sputtered particles is crucial due to its significant impact on erosion and redeposition. For instance, the prevalence of sputtered particles in the high-energy tail tends to surpass the electric field in the plasma sheath, especially for grazing poloidal magnetic field angles. In a related study [77], it was observed that the electric field played a predominant role in the sheath, leading to redeposition at the divertors, even in the presence of drag and temperature decays. Again, in [76], it was noticed that the net flux of particles is mostly populated by the fast tail of eroded particles. Hence, the resulting $f_{non-redep}$, was affected by the angular and energy distribution of sputtered particles. This is because of essentially two reasons: i) faster neutral particles tend to ionize further from the wall, thus, in a zone of low electric field strength, ii) faster particles have a higher chance to overcome the electric field potential in case they are ionized inside the sheath. So it is clear

that in order to describe the net sources a good description of the sputtered particles' energy and angular distribution is needed. In current codes such as ERO [78], ERO2 [22], DIVIMP [79], IMPMC [80], and GITR [23] the sputtered particle flux distribution is generally represented with a Thompson distribution [81] or by some variants adopted for the impact of low-energy plasma particles ([82], [83]). These distributions are calculated experimentally through mono-energetic beams of incident particles. While they are applied, impinging ions are approximated with a mono energetic beam whose energy E_0 is expressed as a function of integrated or 'fluid' plasma quantities, e.g. $E_0 = 2T_i + \Delta\phi Z$, with $\Delta\phi$ being the potential drop in the plasma sheath, see [84]. Neglecting the kinetic distribution by applying averaged 'fluid' quantities has its limitations, for example, in [85] and [23] it was shown that considering kinetic effects leads to a refined estimate of the sputtering yield for gross erosion. In this work, the goal is to go a step further by including the kinetic energy distribution of impinging ions in the assessment of net erosion. Results show that accounting for the whole energy distribution of impinging ions on W is mostly relevant when the incidence energy is close to the sputtering threshold energy limit. In general, only impurities ionized once and plasma ions were close to the sputtering threshold in the simulation here tested. Comparisons between the W net source related to once-ionized impurities and Deuterium (D), the contribution of D is not always negligible. Moreover, it is discussed the dependence of $f_{non-redep}$ with respect to the magnetic field vector and the applied electric potential drop model inside the sheath. Finally, the energy distribution of incident particles shows a good agreement with the one obtained via Monte Carlo simulations.

2.2 Sheath model employed

A Deuterium plasma background is considered, plasma oscillation modes and turbulent fluxes are neglected if compared to convective particle flux. It is considered a steady state flux of impinging ions distributed as $f_i(\vec{v})$ at the sheath entrance (SE) accelerated inside the plasma sheath. Ions are immersed in a uniform magnetic field B oblique with angle α_B respect to an ideal flat surface (no $\nabla\vec{B}$ forces and roughness considered) see figure 2.1. The electric field is considered one-dimensional and normal to the surface. Ions at the SE respect the Bohm criterion and their energy gain both inside the scrape-off layer (SOL) and the sheath is supposed to follow the rule proposed in [60]. Reflections of impinging ions on the target material and redeposition-related sputtering are neglected. The sheath is supposed collisionless and isothermal $T_e \approx constant$, with no gradients along x,y directions. These are working assumptions, in reality, because of charge-exchange collisions the sheath presents a certain degree of collisionality especially for low electron temperature at the sheath edge ($T_e < 10\ eV$), and densities $n_e > 10^{19}\ m^{-3}$ [55]. At the same time, it was already shown in PIC simulations [86], [87] that T_e drops inside the sheath due to the deceleration caused by electric repulsion. According to the mentioned assumptions, the Vlasov equation for impinging ions reads:

$$v_z \partial_z f_i + \frac{Ze}{m}(\vec{E} + \vec{v} \times \vec{B}) \cdot \nabla_v f_i = 0 \tag{2.1}$$

While energy and flux conservation can be expressed with the following equations.

$$f_i(\vec{v})\, v_z\, d\vec{v} = f_i(\vec{v'})\, v'_z\, d\vec{v'} \tag{2.2}$$

$$v_z{}^2 = v'_z{}^2 + \frac{2Ze\Delta\phi}{m} \tag{2.3}$$

Explicitly solving the equation (2.1) would require numerical techniques based for instance on PIC methods, and would lead to expensive simulations. Nonetheless, considerations about the energy distribution of particles at the wall are still possible. Similar to how the Boltzmann factor is usually derived for electron density in a retarding electric field, it can be shown that by neglecting the $\vec{v} \times \vec{B}$ term in equation (2.1) and by combining it with the flux and energy conservation equations (2.2), (2.3), it follows that:

$$f_i(|\vec{v}|) = f_i(|\vec{v'}|) \tag{2.4}$$

$$f_i(|\vec{v}|)\, d|\vec{v}| = f_i(E_0)\, dE_0 \tag{2.5}$$

Where $|\vec{v'}|$ is the velocity module at the SE, $|\vec{v}|$ is the velocity module at the PFM surface, and $E_0 = E'_0 + \Delta E$ is the total energy at the wall. Neglecting the magnetic field entails a wrong evaluation of the impinging ions' angle of incidence α (see figure 2.1). Indeed, as shown in [88], incident ions are still magnetized inside the sheath. Therefore, it was assumed a uniform incidence angle $\alpha = 40°$ for all impinging particles, similar to what was reported in [84]. Finally, the sheath electric potential decay ϕ was approximated using the fit proposed in [58]. An illustration of the electric potential decay ϕ is reported in figure 1.6. The data-set showed in section 2.3.1 was calculated assuming the sheath width equal to two Larmor radii of Deuterium at sonic speed times the cosine of the magnetic field incidence angle ($2\rho_D cos(\alpha_B)$). This width well represents the potential decay described by Brooks [89]. Since for grazing magnetic fields the potential decay might be better described with the model proposed in [62], as done in [75], a comparison between the two potential decay models is discussed in section 2.4.4. Finally, for sputtered W atoms only electron-ion ionizations are considered, collision rates were taken from ADAS [90], and no metastable states were considered.

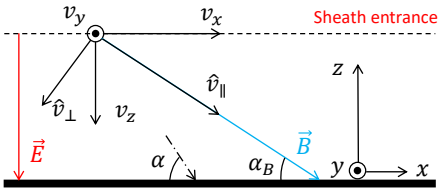

Figure 2.1: Coordinate systems, top left for incident ions, bottom right for sputtered W. Particles and magnetic field $\vec{B}$ etching with angles α and α_B respectively.

2.2.1 Boundary condition - distributions at the Sheath Entrance

In the present work, three different probability density functions $f_i(\vec{v'})$ were tested as boundary conditions at the Sheath Entrance (SE) to assess the relevance of kinetic distributions in the matter of W erosion and redeposition.

1. Delta (δ) distribution. It is extensively used in the state of the art as mentioned in the introduction, it represents the average energy of impinging ions (fluid description).

$$f_i(E_0') = \delta(E_0' - \overline{E_{SE}})$$

   Where $\overline{E_{SE}}$ is the average energy of ions at the SE taken from [60]. For low ionization states $\overline{E_{SE}} \approx 2T_i$ that is, the one-way heat flux associated with a zero-centered Maxwellian velocity distribution.

2. Gamma (Γ) distribution. It represents the parallel velocity distributions of ions accelerated in a collisionless SOL. The term Gamma distribution is used in this work to refer to the case where the parallel velocity distribution is described with a Gamma function while a zero-centered Maxwellian is used for the perpendicular component.

$$f_i(v_\parallel', v_\perp') = \frac{{v_\parallel'}^{k_0-1}}{\Gamma(k_0)\theta^{k_0}} e^{-\frac{v_\parallel'}{\theta_0}} \sqrt{\frac{B_\perp}{\pi}} e^{-B_\perp {v_\perp'}^2}$$

   where k_0, θ_0 are the shape and scale parameters. The average $v_\parallel$ of impinging ions at the sheath-edge was expressed in terms of the function $f(A,Z)$, taken from [60].

   The variance was assumed to be equal to the particles' thermal velocity $\sigma = v_{th} = \sqrt{\frac{eT_i}{m_i}}$. Where T_i is the main ion temperature at the SE and m_i is the incident particle mass. A Gamma probability density function was adopted to represent the parallel velocity distribution because it was in good agreement with a set of parallel velocity distribution functions calculated using the 1D collisionless PIC model of the SOL and sheath, detailed in [91]. As shown in figure 2.2, the gamma function well represents the PIC model results both at the SE and at the plasma-wall interface. To calculate the parallel velocity distribution at the wall, the distribution at the SE is accelerated through the Liouville's theorem. Essentially a gamma function approximates the parallel velocity distribution at the SE of a stream of particles originating upstream in a collisionless SOL.

3. Truncated Maxwellian (TM) distribution. It represents the parallel velocity distributions of ions accelerated in a strongly collisional SOL. The term Truncated Maxwellian distribution is used in this work to refer to the case where the parallel

velocity distribution is described with a flowing Maxwellian truncated at zero for $v_\parallel$ to respect the Bohm criterion. A zero-centered Maxwellian is used for the perpendicular component.

$$f_i(v'_\parallel, v'_\perp) = \sqrt{\frac{B_\parallel}{\pi}} e^{-B_\parallel {v'_\parallel}^2} \sqrt{\frac{B_\perp}{\pi}} e^{-B_\perp {v'_\perp}^2} H(v'_\parallel)$$

This case aims to model the distribution of ions accelerated in a collisional SOL, while the sheath will be still considered collisionless. H is the Heaviside function, necessary to remove backward ions thus respecting the generalized Bohm criterion [49]. It is known that because of the so-called Knudsen layer [52] the distribution at the SE is characterized by two kinetic ionic temperatures $T^i_\parallel$ and $T^i_\perp$. Nonetheless, in this work it was imposed $T^i_\parallel = T^i_\perp$.

Incident kinetic distributions were compared at equal mean speed and variance.

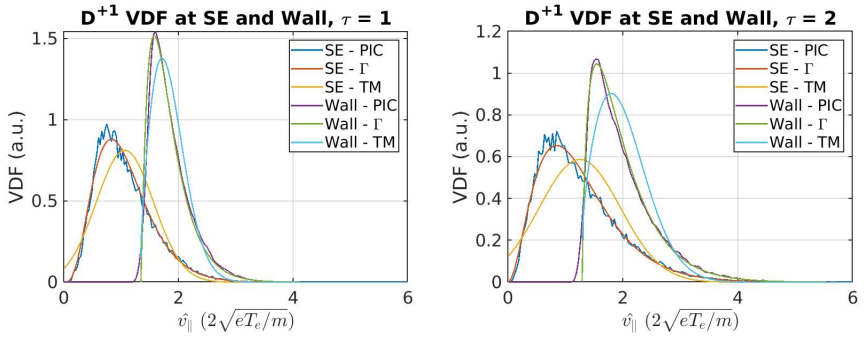

(a) (b)

Figure 2.2: Velocity Distribution Functions (VDF) of Deuterium (D) parallel velocity both at the SE and wall according to the PIC model [91] used as reference, the Gamma (Γ) and Truncated Maxwellian (TM) approximations. a) $\tau = T_i/T_e = 1$ equipartition b) $\tau = 2$.

2.2.2 W erosion and redeposition

For a mono energetic beam of impinging ions, the energy and angular distribution of sputtered W atoms as a first approximation can be represented with a Thompson distribution as done in [60]. The angular distribution is considered cosinusoidal with respect to the polar angle (θ) and constant with respect to the azimuthal one (ϕ). The sputtered W energy-angular distribution is here shown.

$$\Gamma^{Th}_{W^{+0}}(E_0, E, \Omega) dE d\Omega \propto \frac{1}{2\pi} \frac{E}{(E+E_b)^3} \left[1 - \sqrt{\frac{E+E_b}{E_{max}(E_0)+E_b}}\right] cos(\theta) dE d\Omega \qquad (2.6)$$

Where E_0 is the incident projectile energy; E_{max} is the maximum energy of sputtered W, whose formula was taken from a previous work [60]; $E_b = 8.67\ eV$ is the W binding energy and $d\Omega = sin(\theta)d\theta d\phi$. The Thompson distribution coincides with the sputtered neutral W distribution caused by a mono-energetic stream of incident particles. Normally, impinging ions' energy is taken to be equal to their average energy. Hence, their distribution is approximated with a delta function, see section 2.2.1. The key test assumption here is to understand if the distribution of sputtered W changes with respect to the Thompson one when the whole impinging ions energy distribution is included. For doing so it was assumed that every impinging ion with energy E_0 greater than the sputtering threshold energy, sputters W according to a Thompson distribution $\Gamma^{W^{+0}}_{Th}(E_0, E, \Omega)$ as in equation (2.6). The neutral W sputtered distribution was then calculated as the convolution between the normalized Thompson distribution $\Gamma^{Th,n}_{W^{+0}}$ and the impinging flux distribution, all weighted with the sputtering yield (y), as shown in equation (2.7).

$$\Gamma^{0}_{W^{+0}}(E, \Omega) = \int_{E_0} \Gamma_i(E_0)\, y(E_0, \bar{\alpha}) \Gamma^{Th,n}_{W^{+0}}(E_0, E, \Omega)\, dE_0 dE d\Omega \tag{2.7}$$

$$\Gamma_i(\vec{v}) = f_i(\vec{v})\, v_z \tag{2.8}$$

$\Gamma_i(E_0)$ is the incident flux energy distribution along z and $\Gamma^{Th,n}_{W^{+0}}$ is the Thompson distribution, equation (2.6), normalized. Finally, $\alpha = arctan\left(\frac{\sqrt{v_x^2+v_y^2}}{v_z}\right)$ is the impinging ions' incidence angle. As previously mentioned, the incidence angle was assumed to be fixed and equal to $\bar{\alpha} = 40°$.

2.2.2.1 Neutral W transport

Once sputtered, W neutral atoms transport in steady-state is described by the following Vlasov equation.

$$v_z \partial_z f_{W^{+0}} = C \tag{2.9}$$

Neutral tungsten is subjected only to a sink term C representing ionization by electronic collisions. Therefore, $C = -f_{W^{+0}} n_e S(n_e, T_e)$ where n_e is the local electron density and $S(n_e, T_e)$ is the ionization rate coefficient taken from ADAS [90]. As previously mentioned metastable states were neglected, thereby the ionization rate coefficient S dependance on electron density was not included. It was again assumed a uniform target and it was considered only a plasma volume in which thermal gradients are negligible. Equation (2.9) allows assessing the density profile of neutral W inside the sheath $f_{W^{+0}}(z, \vec{v})$, see equation (2.10).

$$f_{W^{+0}}(z, \vec{v}) = f_{W^{+0}}(0, \vec{v}) e^{-\int_0^z \frac{n_e(z) S(Te)}{v_z} dz} \tag{2.10}$$

As expected, $f_{W^{+0}}(z, \vec{v})$ decay is related to the ionization mean free path of neutral

W along the z axis:

$$\lambda_{ion,z} = \frac{v_z}{n_e(z)S(T_e)} \tag{2.11}$$

The same decay applies to the flux distribution as neutrals propagate with conserved momentum.

$$\Gamma_{W^{+0}}(z,\vec{v}) = \Gamma^0_{W^{+0}}(\vec{v})e^{-\int_0^z \frac{dz}{\lambda_{ion,z}}} \tag{2.12}$$

The sink term C defined in equation (2.9) is equal to the divergence of the neutral W flux expressed in equation (2.12), and hence, it is the volumic source of firstly ionized sputtered tungsten (W^{+1}).

2.3 Monte Carlo simulation

Instead of explicitly solving the Vlasov equation for W ionized states, it was decided to sample the W^{+1} source and push the ionized particles via Monte Carlo techniques. Firstly ionized sputtered tungsten atoms were followed within a Monte Carlo simulation to assess the probability density function of non-redeposition $P_{nr}(z,E,\Omega)$. Assuming that the first ionization ($W^{+0\rightarrow+1}$) happens at a distance z, $P_{nr}(z,E,\Omega)dEd\Omega$ is the probability a W^{+1} atom with energy in $(E,E+dE)$ and direction in $d\Omega$ has to not redeposit. The simulation time was set to 5 times the W^{+1} Larmor period as a consequence of a parametric study, see figure 2.3 and section 2.3.1 for more details. Particles were pushed into the monodimensional plasma background via the Boris algorithm [92] simulating the Lorentz Force. The simulation domain was limited only along the z-axis while particles were free to fly into the lateral dimensions as much as they could during the simulation period because no boundary was applied. Further ionizations in the sheath were assumed to follow an exponential distribution time as suggested in [93]. Finally, particles striking back the PFM or with parallel velocity directed towards the wall (for this work $\vec{v}\cdot\hat{v}_{\parallel} > 0$) at the end of the simulation were counted as redeposited; otherwise they were considered as not redeposited. Since ionizations are an intrinsically stochastic phenomenon, more Monte Carlo simulations were performed to get a better assessment of P_{nr}. The iteration was assumed to reach convergence with respect to the estimation of Γ_{net} when an imposed criterion was satisfied, see equation (2.14) in section 2.3.1. In past works such as in [75], and [76]. Monte Carlo simulations were performed to estimate the $f_{non-redep}$ i.e., the average probability of non-redeposition. In those works, it was defined $f_{non-redep} \equiv N_{non-redep}/N$ where N is the number of simulated particles while $N_{non-redep}$ is the number of non-redeposited particles. In a nutshell, P_{nr} was approximated with a binary function of zeros and ones, zero for redeposits, and one for non-redeposits. As pointed out in [76] ionizations influence $f_{non-redep}$ thus the net flux Γ_{net}. For this reason, another path was followed in this paper. The probability P_{nr} is not approximated by a binary function, the Monte Carlo simulation's main output is not $N_{non-redep}$ but is P_{nr}. Having the non-redeposition probability, it is possible to directly calculate the non-redeposited flux of ionized particles $\Gamma^{nr}_{W^{+Z}}$ as the

$T_i = T_e$	$15, 20, 25, 30$	eV
n_e	$5e18, 1e19, 5e19, 1e20$	m^{-3}
B	$2, 3.7, 5$	T
α_B	$2, 4, 8, 20, 40, 75, 85$	deg

Table 2.1: Plasma parameters used to simulate W erosion.

product between P_{nr} and the neutral W sink term C, defined in equation (2.9).

$$\Gamma^{nr}_{W^{+Z}} = \int C(z,E,\Omega) P_{nr}(z,E,\Omega) dz dE d\Omega \tag{2.13}$$

Adding the flux of neutral W reaching the simulation domain upper limit, considered as not redeposited, gives the total net flux Γ_{net}. In the parameter domain studied the neutral W flux $\Gamma^{nr}_{W^{+0}}$ accounted at maximum for 0.1 % of the total net flux.

$$\Gamma_{net} = \Gamma^{nr}_{W^{+Z}} + \Gamma^{nr}_{W^{+0}}$$

Finally, $f_{non-redep}$ is defined as the ratio between the net and gross fluxes $f_{nr} \equiv \Gamma_{net}/\Gamma_{gross}$. In a nutshell, the model here proposed differs with respect to previous works as [76], [75] and [77] by i) considering the impact energy distribution of impinging ions; ii) solving analytically the W^{+0} decay and iii) calculating directly Γ_{net} instead of $N_{non-redep}$.

2.3.1 Numerical setup

A set of Monte Carlo simulation was performed to estimate P_{nr} for the 336 different Deuterium plasma backgrounds, see parameters listed in table 2.1. In order to have an acceptable estimate of the probability distribution $P_{nr}(z,E,\Omega)dEd\Omega$, and hence of Γ_{net}, each volume $dEd\Omega$ must be sampled enough for a considered set of z. For a fixed N number of simulated particles, only η of them will be sampled in $dEd\Omega$. Then, among the η particles sampled, a smaller number $\eta_{non-redep}$ will not be redeposited. For this reason, it was necessary to iterate the simulation n-times until the imposed convergence criterion, see equation (2.14), was satisfied for each simulated plasma background. Finally, $P_{nr}(z,E,\Omega)dEd\Omega$ was approximated as the corresponding fraction $\eta/\eta_{non-redep}$, averaged among the whole iteration process. The simulation stopped at the nth iteration when a relative 5 percent difference $\epsilon = 0.05$ between the net fluxes estimated at the nth and nth-1 iterations was attained. The convergence criteria and the non-redeposition probability updated to the nth iteration are here shown in equations (2.14) and (2.15), respectively.

$$\left|\frac{\Gamma^{n}_{net}}{\Gamma^{n-1}_{net}} - 1\right| \leq \epsilon \tag{2.14}$$

$$P^n_{nr}(z,E,\Omega)dEd\Omega \approx \frac{1}{n}\sum_i^n \left(\frac{\eta_{non-redep}}{\eta}\right)_i \tag{2.15}$$

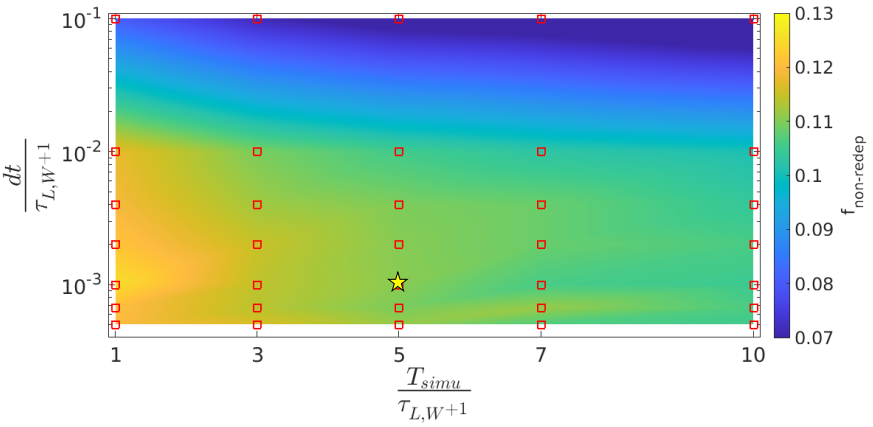

Figure 2.3: Parametric scan of $(dt,\ T_{simu})$ combinations normalized with respect to the W^{+1} Larmor period. Each tested point is represented with a red square, while the chosen combination is highlighted with a star. The interpolated 2D map refers to the following case: $n_e = 1e19\ m^{-3}$, $T_i = T_e = 20\ eV$, $B = 3.7\ T$, $\alpha_B = 2\ deg$, impinging species: O^{+1}, δ model.

A parametric scan over different combinations of total simulated time T_{simu} and time step dt, see figure 2.3 was performed for a specific plasma background. As expected, the more the time step is reduced, the better the final estimate of $f_{non-redep}$ is, since the trajectories and energy balances are more accurately represented [60]. At the same time, a reduction of T_{simu} is followed by an overestimation of $f_{non-redep}$ since the simulation time does not allow particles to redeposit. Finally, a time step equal to one-thousandth of the W^{+1} Larmor rotation period was imposed: $dt = 10^{-3} \times \tau_{L,W^{+1}}$ and a total simulation time $T_{simu} = 5 \times \tau_{L,W^{+1}}$. The whole code was written in the programming language MATLAB ver. R2021-a. Using one core, the simulation time was around 10 minutes per iteration with $N \sim 2.5 \times 10^5$ followed particles. It is worth noting that P_{nr} only depends on the plasma background and not on the impacting species, nonetheless, the convergence criteria does depend on it. Monte Carlo simulations were performed also to assess the IEAD discussed in section 2.4.2.1. In this case, another procedure was adopted, plasma ions coming from the SOL were followed to the wall, and no P_{nr} was estimated. It was imposed a time step $dt = 10^{-4} \times \tau_{L,W^{+1}}$ in order to better describe the ions' angle of incidence.
An $f_{non-redep}$ dataset was obtained by simulating the physical sputtering of a surface made of smooth bulk W subjected to erosion by light impurities such as Boron, Carbon, Nitrogen, Oxygen (B, C, N, O), main plasma ions: D, and self-sputtering (W). Except for Deuterium, the other impinging ions were simulated up to the third ionization state. The temperature, density, and magnetic field conditions are listed in table 2.1.

For each species, all 3 boundary conditions listed in section 2.2.1 were applied.

2.3.2 Model validation

Case #	T_e (eV) at sheath entrance	n_e (cm^{-3}) at sheath entrance
1	20	6×10^{13}
2	5	6×10^{13}
3	20	5×10^{11}
4	5	5×10^{11}

Table 2.2: List of investigated plasma n_e and T_e at the SE. Table adapted from [87]

The present model was validated by comparing its results with previous works. As shown in [76] if the sputtered W distribution is a Thompson distribution (see equation (2.6)) with $E_{max} = 2T_e$, $f_{non-redep} \approx 1/2\sqrt{\chi_{sheath}}$ for $\chi_{sheath} < 0.1$, where χ_{sheath} is the fraction of neutral W ionized outside the sheath region. It was possible to reproduce a similar cut-off energy $E_{max} = 2T_e$ by simulating C^{+3} as impacting species, and using a delta distribution at the SE. As shown in figure 2.4 our results do not follow exactly the equation $f_{non-redep} \approx 1/2\sqrt{\chi_{sheath}}$ proposed in [76], but they have a similar trend that can be approximated as a power of χ_{sheath} times a constant. This could be related to the difference in the applied potential decays and in the method used to infer $f_{non-redep}$. Another commonality with the work of [76] is that $f_{non-redep}$ increases with the charge of the impinging ion. The explanation is the following: higher charge states get more energy from the plasma sheath and so they transfer more energy to the target. In turn, sputtered W has higher energy and ionization mean free path, χ_{sheath} increases and so $f_{non-redep}$.
In addition to that, the model was also validated by comparing it with another previous attempt to numerically estimate W erosion, see figure 2.5. In [87] PIC data was used as input to the code ERO [78] to resolve the plasma sheath. Moreover, the neutral sputtered W energy and angular distribution were described again with the Thompson formula (2.6). Four different cases summarized in table 2.2 corresponding to four different electron densities and temperatures at the sheath entrance were examined. For each case, the fraction of promptly redeposited W (f_p), was assessed four times while varying the Thompson distribution cut-off energy (E_{max}), see equation (2.6). For those cases where $T_e = 20\ eV$, the cut-off energy was set equal to 50, 100, 200, and 300 eV. Similarly, for $T_e = 5\ eV$, the cut-off energy was set equal to 10, 20, 40, and 80 eV. Again, the delta distribution was applied, and the results show a good qualitative agreement. In cases 1 and 3 the average difference is around 8 % and 5 %, figure 2.5. On the other hand, for $T_e = 5\ eV$ (cases 2 and 4) the relative difference increases to 30 % and 100 % respectively. It is interesting to notice that except for case 3, the present model always overestimates f_p, this is probably caused by neglecting the electron temperature drop in the sheath, thus in turn, underestimating the average mean free path of neutral W. In any case, it can be seen that neglecting the T_e drop has

a smaller effect if the temperature at the SE is at 20 eV. This is due to the dependence of the neutral W ionization rate coefficient $S(n_e, T_e)$ on the electron temperature. The rate coefficient from ADAS [90], is less and less dependent from T_e as T_e increases if $T_e \in [5, 100]$ eV, that essentially means that $\partial_{T_e} S(n_e, T_e)$ drops for hotter plasma sheaths. Moreover, for low screening plasma conditions, that is, long ionization mean free path of neutral sputtered W, the fraction of sputtered particles influenced by the potential temperature drop decreases.

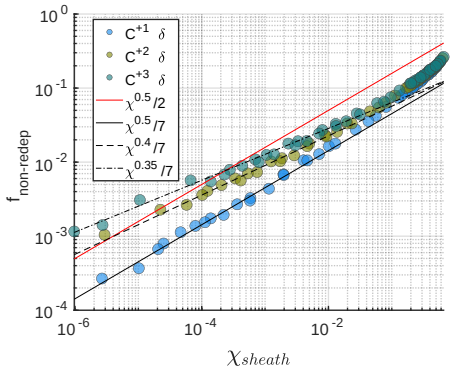

Figure 2.4: Incident δ distribution. $f_{non-redep}$ trends as function of χ_{sheath}, $\alpha_B = 2°$.

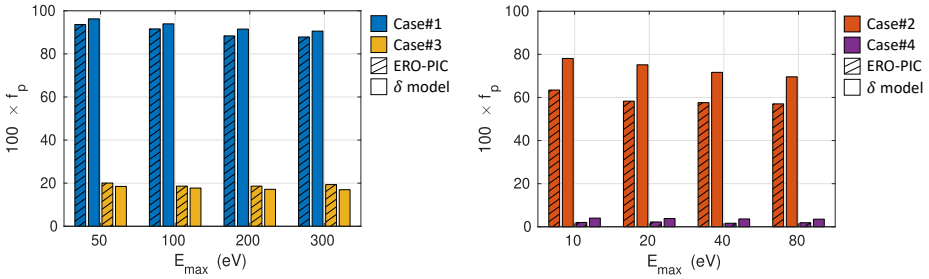

Figure 2.5: Numerical estimates of prompt redeposition f_p for the plasma conditions from table 2.1 in dependence on the cut-off energy. Comparison between ERO-PIC and present work results, a) $T_e = 20$ eV, b) $T_e = 5$ eV.

2.4 Results

2.4.1 Neutral W non redeposition dependence on plasma parameters and boundary conditions

As seen in section 2.3.2, the $f_{non-redep}$ value strongly depends on the fraction of neutral W ionized in the sheath. Equivalently, $f_{non-redep}$ is expected to depend on the average ionization mean free path of neutral W. Always considering [76] as a reference,

$f_{non-redep}$ is correlated with the mean normalized ionization length of neutral W $\hat{\lambda}$ which is defined as:

$$\hat{\lambda} \equiv \frac{1}{\Gamma_{gross}\lambda_{sheath}} \int \lambda_{ion,SE}\Gamma^0_{W^{+0}}(E,\Omega)dEd\Omega \tag{2.16}$$

Where $\lambda_{ion,SE}$ is the neutral W ionization mean free path defined previously in equation (2.11), calculated imposing n_e equal to its value at the sheath entrance (SE). The neutral W sputtered flux at the wall $\Gamma^0_{W^{+0}}$ is defined in equation (2.7). The normalization factor is the sheath width defined as $\lambda_{sheath} = 2\rho_D cos(\alpha_B)$ (as in [58]). The parameter $\hat{\lambda}$ was fitted with a scaling law to relate it to plasma parameters, see equation (2.17), (2.18). The fit here proposed has an accuracy within ± 40 percent. It is valid for magnetic field angles $\alpha_B \in [2,85]\ deg$, and for impinging ion mass ranging from D to W, see section 2.3.1 to see all the simulated conditions. Equation (2.17) was calculated assuming a fluid plasma description.

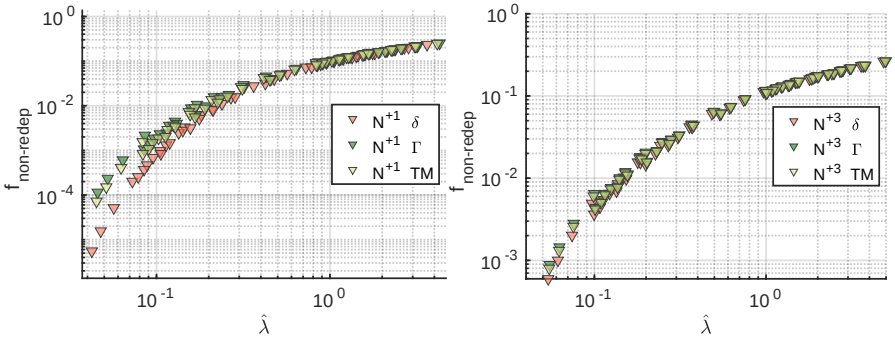

(a) (b)

Figure 2.6: Differences in $f_{non-redep}$ trends for the three different boundary conditions δ, Γ, TM. Grazing magnetic field, $\alpha_B = 2°$. a) N^{+1}, b) N^{+3}

$$\hat{\lambda} \approx g(\alpha_B)\ n_e^{-1} T_e^{-0.88} B m_i^{0.01} Z_i^{0.2} \tag{2.17}$$

$$g(\alpha_B) = 9.3\times10^{-6}\alpha_B^4 - 1.2\times10^{-3}\alpha_B^3 + 4.7\times10^{-2}\alpha_B^2 - 0.56\alpha_B + 5.4 \tag{2.18}$$

Where the units of measure are: $10^{19}\times m^{-3}, eV, T, deg, amu, 1$. It is worth noting that the normalized ionization mean free path depends roughly on the inverse of plasma pressure ($n_e T_e$) and that the impinging ion mass dependence is very weak, as in [94]. Figure 2.7 illustrates all numerically-calculated normalized mean free paths (λ_h) present in the database, plotted against the corresponding λ_h values obtained using the fitting function described in equation 2.18.

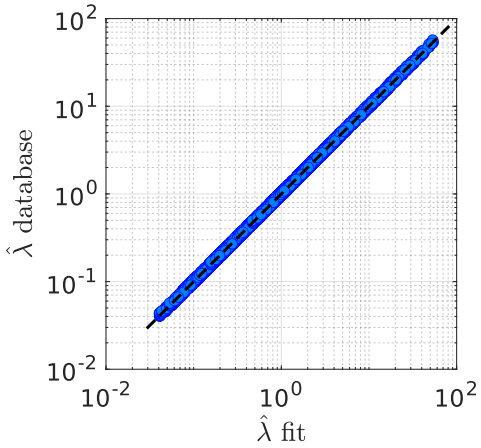

Figure 2.7: Plot of the all values of the normalized mean free path present in the database for the case of a δ boundary condition. The blue circles represent ($\hat{\lambda}\ database$) as function of the corresponding values calculated with the fit proposed in equation (2.18). The dashed black line represents the case $\hat{\lambda}\ database = \hat{\lambda}\ fit$.

The $f_{non-redep}$ trends as function of $\hat{\lambda}$ were compared using both the fluid (δ) and kinetic (Γ,TM) boundary conditions. From figures 2.6a and 2.6b the gap between Γ and TM is small, suggesting that a truncated Maxwellian (TM) in the parallel direction is already a good approximation for impinging ions distribution at the SE. Actually, this is not always true, since for light plasma ions such as Deuterium the gap between Γ and TM can be large, see figure 2.14. Due to its low mass, Deuterium distributions have a high variance. This makes Deuterium more sensitive to the chosen boundary condition. Moreover, it was seen that choosing a Gamma distribution always results in a higher $f_{non-redep}$ due to its longer high-energy tail. Finally, adopting the whole kinetic energy distribution is important only for highly screened plasmas $\hat{\lambda} \ll 1$, and for impinging ions with low ionization states. For N^{+1} using a delta function leads to an underestimation of $f_{non-redep}$ up to 10 times when $\hat{\lambda}$ is at its minimum value in the examined database ($\hat{\lambda} = 0.0404$). On the other hand, for N^{+3} the maximum difference is around 40 percent.

2.4.1.1 Probability distributions of non redeposition and cone of loss

The computation of P_{nr} provides insights about the redeposition phenomenon and will be used here to examine the concept known as the "cone of loss". This concept plays a significant role in gyromotion-related redeposition. As outlined in [74], sputtered ions have the capacity to redeposit due to the fact that, during their gyromotion, they cover a distance toward the surface from which they were initially eroded. This distance is directly proportional to their Larmor radius. Consequently,a larger Larmor radius corresponds to a greater amount of redeposited particles. The Larmor radius is proportional to the perpendicular-to-B velocity expressed in equation (2.19),

whose components can be represented in a magnetic coordinate system, which consists of a vector aligned with the magnetic field direction and two additional vectors perpendicular to the magnetic field. These relationships are expressed as follows.

$$\begin{pmatrix} v_{\parallel} \\ v_{\perp_1} \\ v_{\perp_2} \end{pmatrix} = \begin{pmatrix} cos(\alpha_B)cos(\phi_B) & cos(\alpha_B)sin(\phi_B) & sin(\alpha_B) \\ sin(\alpha_B)cos(\phi_B) & sin(\alpha_B)sin(\phi_B) & -cos(\alpha_B) \\ sin(\phi_B) & cos(\phi_B) & 0 \end{pmatrix} \begin{pmatrix} v_x \\ v_y \\ v_z \end{pmatrix}$$

$$v_{\perp} = \sqrt{v_{\perp_1}^2 + v_{\perp_2}^2} \tag{2.19}$$

The magnetic field direction and the velocity vector of a sputtered particle are depicted in figure 2.8.

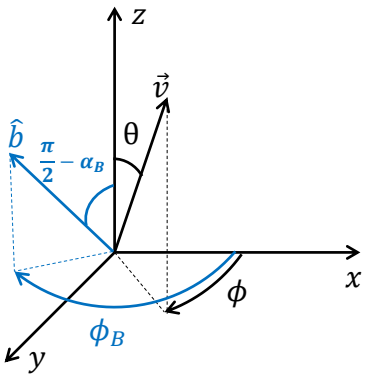

Figure 2.8: Coordinates system of sputtered particles

Where $v_{\parallel}$ is the component parallel to the magnetic field, while $v_{\perp_1}$ and $v_{\perp_2}$ are the perpendicular components which can be combined as in equation (2.19). For a given magnetic field orientation (α_B, ϕ_B), there exists a fraction of sputtered particles whose direction falls within a solid angle $\Delta\theta\Delta\phi$, where the Larmor radius tends to zero $(\rho_L \to 0)$, and as a result, these particles do not redeposit due to gyromotion. This solid angle where particles have a higher chance to escape is the cone of loss which may be important because it influences the redeposition probability of particles sputtered inside the solid angle $\Delta\theta\Delta\phi$.
The cone of loss translates in the probability $P_{nr}(\theta)$ has a preferential interval $\Delta\theta$ close to $\pi/2 - \alpha_B$, where the probability of non redeposition is higher. In figures 2.9, 2.10 are shown four examples of P_{nr} maps for different electron densities and temperatures at the sheath entrance. It is noted that for each case redeposition depends mainly on the distance along z of first ionization. If a particle has enough energy to ionize far away from the magnetic presheath entrance $(z \sim 10^{-2}\ m)$ then, its probability of non-redepositing is 100% and is roughly independent from the poloidal angle θ. Of course, a particle sputtered almost parallel to the wall $(\theta \to 90\ deg)$ will never reach such distances but in P_{nr} every possible scenario is accounted. In general P_{nr} includes a series of almost impossible conditions. For instance, since the ionization

distance z is proportional to the energy E, hardly there will be particles with high energy ionizing close to the wall, anyway in P_{nr} also such possibility is included. The cone of loss has a visible influence on the P_{nr} poloidal distribution for low electron temperatures and densities at the sheath entrance. For instance, figure 2.9a shows a P_{nr} map for $n_e = 5e18\ m^{-3}$ and $T_e = 5\ eV$. It is noticeable that sputtered particles whose $\theta \in [55, 80]\ deg$ have a higher chance to escape. This is because for such low temperatures and densities multiple ionization is unlikely and the Larmor radius length of sputtered ions only depends on $v_\perp$. Moreover, for low temperatures the electric potential in the sheath is small and even particles ionizing close to the wall ($z = 10^{-4}\ m$) may have enough energy to overcome the electric field, thus redeposition is mostly caused by gyromotion. Predictably, for higher electron temperatures the cone of loss influence vanishes as the electric field force inside the sheath dominates redeposition, see figure 2.9b. Similarly, higher electron densities result in a smaller influence of the cone of loss. In figure 2.10a, multiple ionization favours particle escaping for a broader range of poloidal angles if compared to the low density case of figure 2.10a. For high density and temperature the cone of loss is negligible, see figure 2.10b. Lastly, in the upper left corner of all P_{nr} maps the escaping probability is almost zero. This is because sputtered particles with large poloidal angles (hence, with direction more parallel to the eroded surface) and ionizing in the sheath, have not enough energy in the z-direction to overcome the sheath electric field. As density and temperature increase, the area where $P_{nr} = 0$ expands.

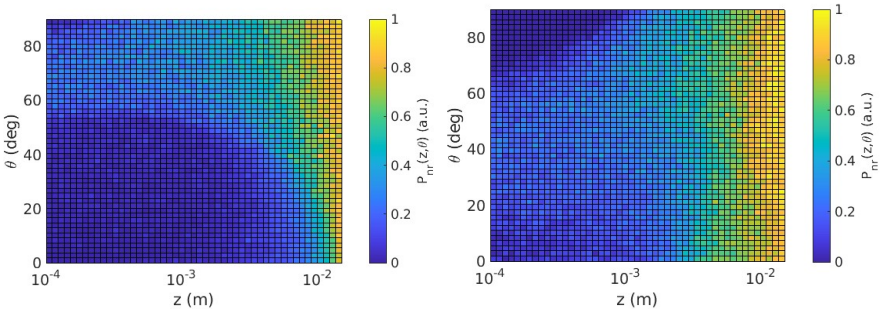

(a) $T_e = 5\ eV$ (b) $T_e = 30\ eV$

Figure 2.9: Normalized probability of non redeposition P_{nr} as a function of the first ionization distance z and the poloidal angle θ. Images depict a low density case $n_e = 5e18\ m^{-3}$ with magnetic field $B = 3.7\ T$ and angle $\alpha_B = 4\ deg$

To conclude, the poloidal distribution of sputtered W may play an important role when the electron density and temperature at the sheath entrance are relatively low because of the cone of loss. For higher densities and temperatures, the angular distribution still has an impact, since it modifies the energy along z hence the ionization mean free path along z of neutrals sputtered particles. Contrarily to the cone of loss the change in E_z persists, and if the distribution is peaked at large poloidal θ angles, more particles will redeposit due to ionization in the sheath.

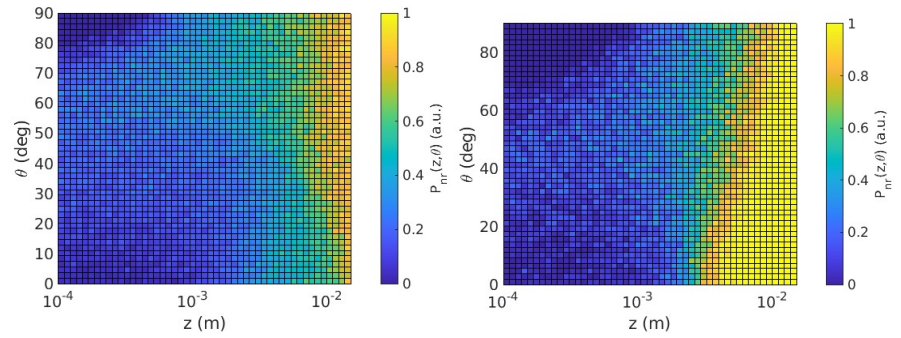

(a) $T_e = 5\ eV$ (b) $T_e = 30\ eV$

Figure 2.10: Normalized probability of non redeposition P_{nr} as a function of the first ionization distance z and the poloidal angle θ. Images depict an high density case $n_e = 1e20\ m^{-3}$ with magnetic field $B = 3.7\ T$ and angle $\alpha_B = 4\ deg$

2.4.1.2 Magnetic field configuration influence on W redeposition

Variations in the magnetic field intensity and angle of incidence affect the redeposited fraction. For instance, an increase in the intensity results in a decrease of the Larmor radius ρ_D thus in a decrease of the plasma sheath thickness or equivalently, an increase of the $\hat{\lambda}$ factor, see [76] and equation (2.17). Similarly, as the angle of incidence α_B increases, the sheath thickness decreases. In both cases, by reducing the sheath width there is an increase in $\hat{\lambda}$, hence an increase of the net W source. The increase in $f_{non-redep}$ as $|\vec{B}|$ or α_B increases depends on $\hat{\lambda}$. In general, the lower the electron density n_e and temperature T_e (higher $\hat{\lambda}$) the less $f_{non-redep}$ is sensitive to plasma conditions, see figures. 2.11a and 2.11b. Actually, for $\hat{\lambda} \gg 1$, since most particles ionize outside the sheath, also W falls in the redeposition ballistic regime described by Fussman [74]. The relationship between $\hat{\lambda}$ and $f_{non-redep}$ is not always perfectly monotonically increasing in our database. As a consequence, especially when it is calculated the ratio between two small $f_{non-redep}$ values some noise may appear as in figure 2.11b where an outlier is found at $\hat{\lambda} \approx 0.06$. Moreover, what is shown in the figure 2.11b, demonstrates that in order to compare W erosion studies done in different machines it is necessary to scale the data according to the difference in intensity between the applied magnetic fields. The effect of the magnetic field intensity can be explained as follows. It is noted that the Larmor radius scales linearly with B. Thus, for weak magnetic fields, the probability of redeposition related to gyro-motion is higher. On the other hand, if B increases, according to [58], the potential drop $|\phi(z)| \propto exp(-B)$, decreases, leading to a reduction of redeposition caused by the electric field. Since for small α_B the electric field is predominant, an increase of B means less redeposited particles. Thus, in tokamaks with shallow magnetic angles and strong magnetic fields more particles are foreseen to overcome the sheath.

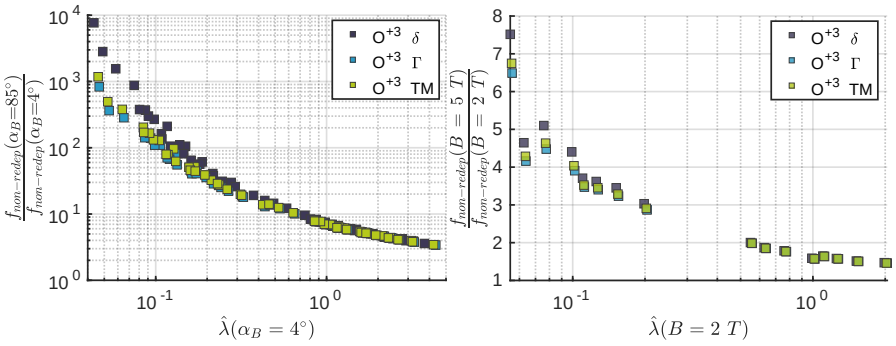

(a) (b)

Figure 2.11: Differences in $f_{non-redep}$ trends for the three different boundary conditions δ, Γ, TM. a) increase in $f_{non-redep}$ going from $\alpha_B = 4°$ to $\alpha_B = 85°$, b) increase in $f_{non-redep}$ going from $B = 2\ T$ to $B = 5\ T$ with fixed $\alpha_B = 4°$.

2.4.2 Effective sputtering yield

The sputtering yield $y(E_0, \alpha)$ is a function of the energy and angle of impact of the incident particles. It quantifies the number of eroded particles per incident particle and is fundamental for the quantification of the gross eroded flux $\Gamma_{gross} = \Gamma_{inc} \times \overline{Y}$. The sputtering yield formula for the database is that proposed by Garcia in [36]. As shown in [69], and done in [23], the sputtering yield function (y) shall be integrated with the distribution function of impinging particles at the wall $f_i(E', \alpha')$ resulting in an effective sputtering yield $\overline{Y}$.

$$\overline{Y} = \frac{1}{\Gamma_{inc}} \int \int \Gamma_i(E_0, \alpha) y(E_0, \alpha) dE_0 d\alpha \tag{2.20}$$

The assumption of incident distribution equal to a Truncated Maxwellian or a gamma function thus results in a different estimate of $\overline{Y}$ than in the fluid case where a δ distribution is instead considered. Fixing the impinging ion angle of incidence $\alpha = 40°$ remove the angular dependence, thus, $\overline{Y}$ depends only on the impact energy. The total impact energy in turn mainly depends on the electron temperature T_e, the ratio $\tau = T_i / T_e$ in the sheath, and the impinging ion ionization state. It was possible to express $\overline{Y}$ as a second-order polynomial function of the sputtered W temperature, which was defined as $T_{W^{+0}} \equiv \Gamma_{gross}^{-1} \int \Gamma_{W^{+0}}^{0}(E, \theta) E dE d\theta$.

$$\overline{Y} \approx C_1 T_{W^{+0}}^2 + C_2 T_{W^{+0}} + C_3 \tag{2.21}$$

Where, for the light impurities B, C, N, O, the temperature $T_{W^{+0}}$ can be approximated by a scaling law, $T_w \approx \xi_1 T_e^{\xi_2} Z^{\xi_3}$, with fitting errors less than 1 percent if $\tau = 1$. The C and ξ coefficients of equation (2.21) slightly depend on the ions mass (m_i). This is direct consequence of the sputtering yield being proportional to the energy transferred to the target, see equation (1.4). The power balance is given by the heat flux entering into the material brought by plasma species and impurities $q_i = \Gamma_{inc} \overline{E_0}$ minus the outgoing heat flux carried by the sputtered species $q_t = \Gamma_{inc} \overline{Y}\ \overline{E}$. The heat

flux transfer efficiency from plasma to sputtered particles is than defined as the heat flux ratio.

$$\eta_{E_0 \to E} = \frac{q_t}{q_i} = \frac{\overline{Y}\,\overline{E}}{\overline{E_0}} \tag{2.22}$$

Where the average sputtered energy $\overline{E}$ is proportional to the W temperature T_w. If the sputtered energy distribution is Thompson-like its average energy, hence $\eta_{E_0 \to E}$, depends on the mass ratio m_i/m_t, and material properties such as the binding energy [60]. As shown in figure 2.12, considering the incident energy distribution can bring up to a difference between 4 and 5 times in the sputtering yield of firstly ionized light impurities. On the other hand, for the second and third ionization states the difference is around 10 to 30 %. The energy distribution seems to have in general a negligible impact on more than once ionized particles. The ratio between the effective sputtering yield calculated with a delta and a TM functions according to equation (2.20) decreases as the electron temperature and the impinging ion charge increases. Essentially, the higher the energy gain inside the sheath the smaller the difference. As opposed to $f_{non-redep}$, an increase in T_e reduces the difference between the δ and TM distributions. This shows that for W redeposition ($f_{non-redep}$) the increase in ionization rate is faster than the increase in sputtered W ionization mean free path for increasing T_e.

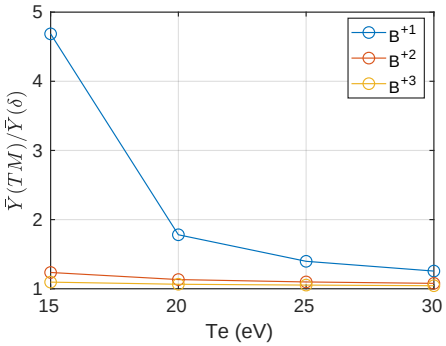

Figure 2.12: Ratio of $\overline{Y}$ calculated using (δ) and TM as incident distributions. Results are shown for boron in its first three ionization states, B^{+1}, B^{+2}, B^{+3} .

2.4.2.1 IEAD, the Impact Energy and Angular Distribution

In section 2.4.1 was shown the difference in $f_{non-redep}$ between fluid (δ) and kinetic (Γ or TM) sputtering description while considering a fixed impact angle. In the following section, we temporarily relax this assumption by adopting a Monte Carlo simulation to estimate $f_i(E_0, \alpha)$ hence the impinging ions energy and angular distribution (or IEAD). A TM distribution of impinging ions (see section 2.2.1) was sampled at the sheath entrance. Particles were pushed using the Boris [92] algorithm till the PFM surface. As a preliminary study it was simulated a stream of O^{+1} immersed in high screening plasma conditions ($\hat{\lambda} \ll 1$). First, we noted (see figure 2.13b) that the

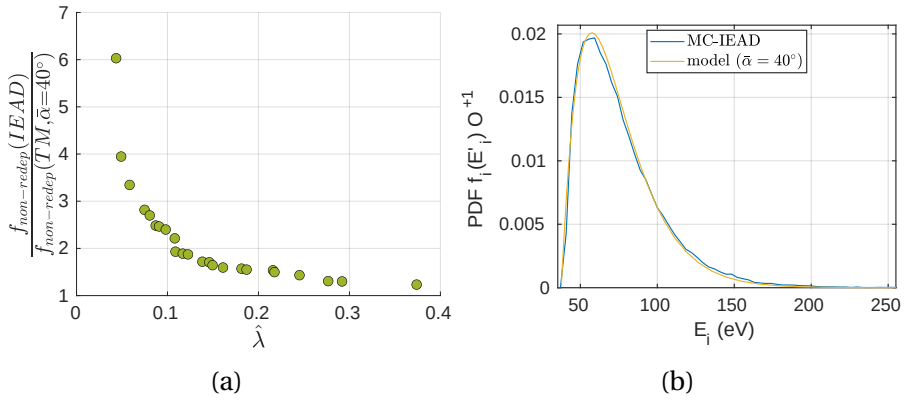

(a) (b)

Figure 2.13: a) Incident O^{+1} on W. Ratio of kinetic $f_{non-redep}$ both using a TM distribution with a fixed angle of incidence $\overline{\alpha} = 40°$ and the whole IEAD. b) Energy distribution at the target estimated for the two cases.

description of the energy distribution given by the equations (2.1 to 2.3) matches the Monte Carlo simulation estimate for O^{+1} and $T_e = 15\ eV$. Moreover, as shown in figure 2.13a, another factor of 6 rose up between $f_{non-redep}$ estimates with a fixed angle of incidence or by considering the whole IEAD when $\hat{\lambda} \ll 1$. Finally, a 30% to 60% increase in the sputtering yield was calculated. Again, this was verified only for O^{+1}, further studies should be done. However, a decrease in the $f_{non-redep}$ ratio shown in figure 2.13a is envisaged for higher charge states. Moreover, because of roughness [35], the sputtering yield angular dependence decreases reducing the effect related to the angular distribution of impinging ions.

2.4.3 Plasma ions erosion - Deuterium

By considering the whole energy distribution of impacting ions, also those species whose average energy was below the sputtering threshold can erode because of their high-energy tail. It was possible to calculate the $f_{non-redep}$ caused by D^{+1} in any conditions, see figure 2.14. Since D^{+1} is one of the most abundant species inside tokamaks operating with it as a fuel, assessing its relative contribution to W erosion could be of interest. First of all, if the erosion provoked by different impinging impurities is considered a linear process, the total flux Γ_{net} is given by the sum of all contributing species.

$$\Gamma_{net} = \Gamma_{inc} \sum_i \left(Cc \overline{Y^{net}} \right)_i \tag{2.23}$$

Where Γ_{inc} is the total incident flux, Cc is the impurity concentration, and $\overline{Y^{net}} \equiv f_{non-redep} \overline{Y}$ is the net sputtering yield. If we consider every impurity having the same concentration, in particular $Cc = 1$, their contribution can be compared looking at the net sputtering yield. In order to make an accurate comparison, it was decided to use the experimental sputtering yield values taken from Eckstein ([29]). Given the lack of

data, the comparison was made only between Deuterium, Nitrogen, and Tungsten. As mentioned in section 2.4.1, the net sputtering yield of Deuterium strongly depends on the boundary condition. From figure 2.14, it is clear that $(\overline{Y^{net}}_{D^{+1}})$ is always the smallest. Nonetheless, the net flux also depends on the impurity concentration. If impurities concentration with ionization state $Z = 1$ is around $\sim 10^{-2}$, Deuterium and impurities' $\overline{Y_{net}}$ is comparable. For instance, as shown in figure 2.14, Deuterium $\overline{Y_{net}}$ is expected to be less than 100 times smaller when $\hat{\lambda} > 0.3$. Hence, there is a set of plasma conditions for which Deuterium contribution to the total net flux is not negligible.

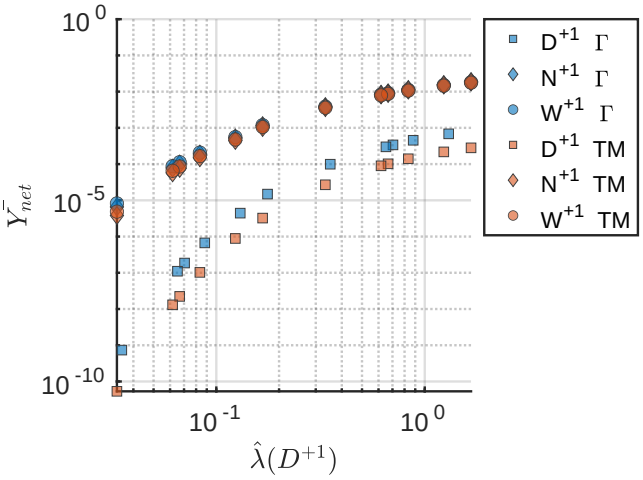

Figure 2.14: $\overline{Y} \times f_{non-redep}$ trends with respect to $\hat{\lambda}$ for D^{+1}, N^{+1}, W^{+1}. Incident TM and Γ distributions, $\alpha_B = 2°$ and $T_e = T_i = 30eV$.

2.4.4 Potential drop model uncertainty

Once plasma conditions $(\vec{B}, n_e, T_e, T_i)$ and the incident ion mass and charge (m_i, Z_i) are fixed, the fraction $f_{non-redep}$ depends mainly on the sheath thickness. The potential drop is usually described with the Brooks or Stangeby [62] models. The difference between the two models concerns the sheath thickness. In the electric potential drop fit proposed in [58] and used here, to reproduce Stangeby's electric potential profiles one has to enlarge the sheath thickness from $2\rho_D cos(\alpha_B)$ for Brooks model to $3\rho_D cos(\alpha_B)$ for Stangeby's. As shown in [75], the uncertainty on the model leads to a difference in the estimation of $f_{non-redep}$ as $\hat{\lambda}$ falls. Consequently, the difference in $f_{non-redep}$ made with a fluid or kinetic model also increases. Using the potential drop proposed by Stangeby, the $f_{non-redep}$ related to incident light impurities ionized once with a fluid model can be 3 orders of magnitude smaller than the one calculated considering the incident energy distribution, see figure 2.15a. Nonetheless, the kinetic correction saturates quickly with respect to the impinging ion charge. As shown in figure 2.15b, the kinetic correction becomes less important resulting in a factor of 2 difference when $\hat{\lambda} \ll 1$. Finally, there is also an uncertainty related to the ionization

rates. Evidence have been gathered as in [95] according to which neutral W metastable states should be considered to better estimate W ionization coefficients. This would in theory reduce the average ionization length of neutral tungsten, thus $\hat{\lambda}$.

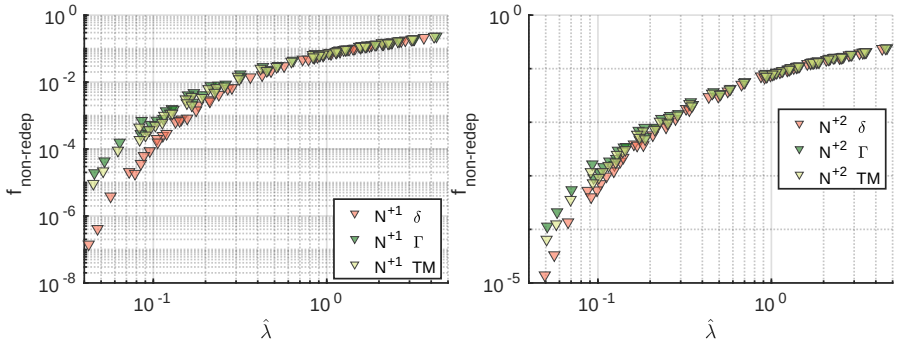

(a) (b)

Figure 2.15: Stangeby's potential drop; differences in $f_{non-redep}$ trends for the three different boundary conditions δ, Γ, TM for a grazing magnetic field, $\alpha_B = 2°$. a) N^{+1}, b) N^{+2}

2.5 Discussion

In this chapter, the fraction of non-redeposited W was calculated for a wide range of simplified 1D plasma conditions by a semi-analytical model based on Monte Carlo techniques. The model was benchmarked with previous attempts to numerically assess net erosion and it showed a good agreement in the parametrical range of this study. The results respected the expected physical trends. It was seen, for example, that the fraction of non-redeposited W depends mainly on the competition between the average ionization length of the sputtered neutral W and the sheath thickness. The scan of 336 plasma backgrounds and the sputtering induced by different impurities ranging from Deuterium to Tungsten showed that the kinetic description of sputtering accounting for the incident energy distribution, with fixed impact angle, has a nonnegligible effect only for impurities ionized once and for sputtering produced by plasma ions such as Deuterium (sections 2.4.1 and 2.4.3). The explanation is the following: the refined distribution of sputtered neutral W following the kinetic description is nothing more than a weighted average between the incident distribution, the sputtering yield, and the Thompson distribution. It is thus intuited that if the sputtering yield is constant, the distribution of the sputtered neutral W tends to the Thompson one caused by a mono energetic beam of particles whose energy is equal to the distribution average energy. The sputtering yield variation decreases rapidly when the energy of the impinging ion is greater than its minimum sputtering energy; $E_0 > E_{min}$. In general, the sputtering yield tends to a constant value for $E_0' + \Delta E >> E_{min}$. Since $\Delta E \approx \Delta\phi Z$ the impact energy of the incident ions is directly proportional to their ionization state Z and to the sheath electron temperature T_e. According to the model discussed here,

when $T_e \geq 15eV$, already for $Z = 2$ the sputtering yield is roughly constant. Thus, particles in the fast tails of the distribution will contribute about the same as the less energetic particles because of an overkill effect where the excess energy is not increasing much the sputtering yield. However, even higher ionization states are expected to benefit from kinetic correction if the electron temperature is very low. It is possible to demonstrate the above by taking the probability density function (PDF) associated with the equation (2.7).

$$\Gamma^{0,n}_{W^{+0}}(E,\Omega) = \frac{\int_{E_0} \Gamma_i(E_0)\, y(E_0,\overline{\alpha}) \Gamma^{Th,n}_{W^{+0}}(E_0,E,\Omega)\, dE_0\, dE\, d\Omega}{\int_{E_0} \Gamma_i(E_0))\, y(E_0,\overline{\alpha})\, dE_0}$$

If the incident particle energy distribution is such that the sputtering yield is approximately constant and thus independent of the incident energy, it can be simplified. Therefore, the PDF tends to that produced by a delta function centered in the mean value, i.e., to the fluid value.

$$\Gamma^{0,n}_{W^{+0}}(E,\Omega) = \frac{\int_{E_0} \Gamma_i(E_0) \Gamma^{Th,n}_{W^{+0}}(E_0,E,\Omega)\, dE_0\, dE\, d\Omega}{\int_{E_0} \Gamma_i(E_0)\, dE_0} = \Gamma^{0,n}_{W^{+0}}(\overline{E_0},E,\Omega)$$

With $\overline{E_0}$ being the average incident energy. So, for a fixed angle of incidence, the sputtering yield converges to a constant for most species. Despite that, the convergence actually depends on the angle of incidence as well. For example, for some angles, the convergence is reached for higher energies and the kinetic correction might be more pronounced, (section 2.4.2.1). In this work, the kinetic correction regards only the neutral sputtered W high-energy tail and not its angular distribution. The importance of this correction depends on how much the high-energy tail population increases by it and on plasma screening $\hat{\lambda}$. If plasma screening is low ($\hat{\lambda} \gtrsim 1$) most of the particles are not redeposited and the population fraction populating the tails is negligible if compared to the whole non-redepositing population. At the same time, the tail population is less affected by the kinetic correction for ionization states greater than one, see sections 2.4.1 and 2.4.4. On top of that, it shall be kept in mind that by considering reflections the transferred energy to the target decreases. Therefore, the sputtering yield is more sensitive to the energy distribution of impinging ions thus the kinetic correction could be more important. On the other hand, the electron temperature drop inside the sheath tends to diminish the kinetic correction increasing $\hat{\lambda}$. Lastly, the material roughness could also vary the sputtering yield sensitivity to the incident energy. For instance, it was seen that the sputtering yield angular dependence flattens out if the roughness is included [35]. The overall balance between these effects mentioned should be analyzed in future proceedings. Finally, in this work, it was possible to compare erosion from Deuterium with that produced by light and heavy impurities for $T_e \in [15,30]\ eV$. It was seen that the contribution of Deuterium is not always negligible if compared to once-ionized impurities.

3 Model reduction through Neural Network and analytical models

Sommaire

3.1 Neural Network-based estimation of W redeposition 58
3.1.1 Database production and data preprocessing 59
3.1.2 NN features and results 60
3.1.3 Prompt redeposition or total redeposition? What is best for a fluid plasma solver 63
3.2 Analytical model to estimate prompt redeposition 64
3.2.1 Energetic redeposition 64
3.2.2 Geometric redeposition 69
3.2.2.1 Multiple ionization 72
3.2.2.2 Redeposition for non grazing magnetic field angle . . . 73
3.2.3 Collisional sheath 76
3.2.4 Two-groups theory 77
3.2.5 Three-groups and tuning of the code 80
3.2.5.1 Fluid parallel velocity 84
3.3 Prompt self sputtering 86

3.1 Neural Network-based estimation of W redeposition

In order to produce an impurity source code capable of providing the necessary information regarding impurity sources in fluid codes, the Monte Carlo methodology previously shown cannot be directly applied. Indeed, conducting a Monte Carlo simulation for every grid point on the wall is prohibitively expensive. In this chapter, we delve into simplified models also known as reduced models, which aim to approximate the output data of Monte Carlo simulations while demanding fewer computational resources. The initial reduced model employed is a Neural Network (NN), utilized as a tool to predict only the fraction of non-redeposited particles ($f_{non-redep}$). Since gross erosion can be computed using simple fit formulas that can be implemented in any code, the NN could be used to rapidly estimate the main quantity of interest, the net flux. The NN is preferred over an analytical fit because despite $f_{non-redep}$ depends mostly on $\hat{\lambda}$ (equation (2.17)), an accurate fitting of $f_{non-redep}$ is nonetheless

challenging. Indeed, as shown in figure 2.4, it is evident that the fraction $f_{non-redep}$ depends also on the sputtered energy and angular distribution (SEAD). Anyway, the biggest turnaround of making a fit with Neural Networks (NN) is that such technique requires a large database of numerical results. Luckily, each calculated P_{nr} function (see chapters 2.3.1 and 2.4.1.1) can be used for any SEAD, thus it is independent from the incident energy and angular distribution. Computing $f_{non-redep}$ once P_{nr} is known, is extremely fast because no particle tracking is needed and only a numerical integration is required, see equation (2.13). Hence, a large database capturing both dependencies on $\hat{\lambda}$ and $\overline{E_0}$ is rapidly built and a NN approach becomes achievable.

3.1.1 Database production and data preprocessing

Despite the assumption of a stationary 1D noncollisional sheath has limited applicability [55], the range of sheath parameters fed to the NN has been expanded compared to the dataset in table 2.1. The updated list of sheath parameters is presented in table 3.1. It includes a total of 12600 sheath parameter combinations. For each combination, the associated P_{nr} function is computed and stored. The value of the fraction of non-redeposited particles ($f_{non-redep}$), besides P_{nr}, also depends on the energy and angular distribution (SEAD) of the eroded species. The SEAD of sputtered neutral W is calculated integrating the product between the incident energy distribution of the impinging ion, the sputtering yield for a fixed angle $\hat{\alpha}$, and the normalized Thompson distribution, as discussed in the previous chapter in equation (2.7). For this study, the Bohdansky sputtering yield formula [38] and an energy Γ distribution with fixed $\alpha = 4\hat{0}\ deg$ are considered. A set of different incident species species is utilized to include the dependencies on mass and charge state. The input species are H, D, He, B, C, N, O, and W in all their charge states, (from the first up to their atomic number) except made for W whose simulated charges are $Z_i = 1,2,3,4,5,6,8,9,10,11,12,20$. Finally, 43 SEAD are computed on the fly using equation (2.7) for each P_{nr}, resulting in a total of $43 \times 12600 = 541800$ $f_{non-redep}$ numerical estimates. The plasma sheath model employed for P_{nr} is the same as discussed in 2.2. Lastly, only smooth W as target material is considered. As a consequence, the NN is trained on a dataset with fixed sheath model, SEAD model, and target species. This makes the NN dependent only on 7 free parameters, i.e. depends on 5 sheath parameters plus the mass and charge of the incident ion. The primary drawback of this approach lies in its rigid fitting of a certain set of hypotheses which can only be generalized by adding other free parameters or dimensions to the problem. This would in turn require the calculation of further P_{nr} increasing the training cost.
To avoid the NN fit being skewed by $f_{non-redep} = 0$ values, all points whose $f_{non-redep}$ value is lower than 10^{-10} are eliminated. Additionally, instead of providing the NN with an output $out = f_{non-redep}$, the output is transformed to $out = log(-f_{non-redep})$ because the transformed output range covers a narrower span of orders of magnitudes, making the fitting by NN more manageable. As commonly done in literature [96, 97] each input parameter, see table 3.1, is normalized to improve the training process and the overall performance of the NN. In this case the most suitable neuron's

T_e	$1,2,3,5,10,15,20,25,30,35,40,45,80,120,160$	eV
$\tau = T_i/T_e$	$0.5,1,2,3$	
n_e	$0.01,0.1,0.5,1,3,5,7,9,10,100$	$1e19\ m^{-3}$
B	$2,3.7,5$	T
α_B	$2,4,8,20,40,75,85$	deg

Table 3.1: Sheath parameters scanned to feed the NN.

activation function proved to be the hyperbolic tangent (tanh), as a consequence, the input parameters are normalized between -1 and 1. The database was divided into three groups i.e., the training, validation, and test datasets. The training and validation datasets are used to tune the NN hyper-parameters and to reduce the loss; the test dataset is instead never used to train the network and it serves as an unbiased benchmark to check the NN performance. These values are within the common ranges recommended in the literature, as indicated in [98]. While these ratios are considered standard, it's important to note that no specific investigation into optimizing the dataset split was conducted.

3.1.2 NN features and results

The NN was built in Keras [99]. It is a Feed Forward kind (FNN), where the information flux is unidirectional going from input to output. Hidden layers are dense, that is, each neuron at the $n-th$ hidden layer is connected to every neuron at the $n-1$ layer. The standard optimizer in Keras has been chosen, which is based on the Adam algorithm for gradient stochastic descent [100]. Four hyper-parameters are tuned: learning rate, batch size, number of neurons per layer (n_N), number of layers (n_l). The learning rate and batch size were fixed to 5e-4 and 128 respectively, after manual experimentation. The remaining hyper-parameters were optimized using the function gp_minimize present in the Scikit-Optimize libraries [101, 102]. The function gp_minimize is utilized as follows: with fixed learning rate l_r and batch size, 11 pairs of (n_N, n_l) are randomly selected from a user-defined range. The validation loss is then evaluated after 30 epochs for each pair of (n_N, n_l). The pair exhibiting the optimal performance is employed in constructing the neural network. The activation functions for the neurons are configured as the hyperbolic tangent (tanh) for the hidden layers and the Rectified Linear Unit (ReLU) for the output layer. Figure 3.1 depicts the training and validation losses, measured in terms of Mean Absolute Percentage Error (MAPE), for the optimal pair $(n_N = 69, n_l = 7)$. It is observed that the loss curve reaches a plateau after a few hundred epochs, leading to the decision to halt the training process after 500 epochs to prevent overfitting.

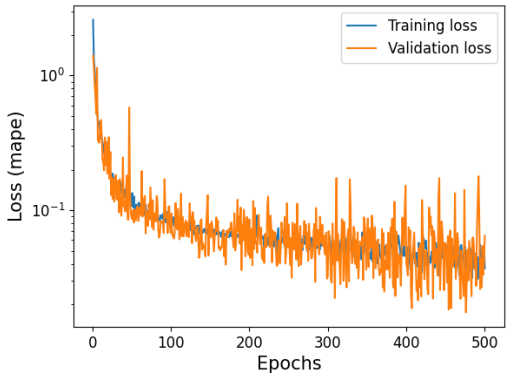

Figure 3.1: Training and validation loss with respect to the number of epochs.

The neural network exhibited strong agreement with both the trained and test data. A significant portion of the training dataset (97%) predicted by the neural network lies within a 40% deviation from the actual Monte Carlo values, as depicted in Figure 3.2. Moreover, 90% of the predictions fall within a 20% error range. Comparisons with the test dataset showed that the NN follows the expected $f_{non-redep}$ trends, for each input parameter, see figure 3.3. That being said, the Neural Network serves as a swift and accurate tool capable of estimating W redeposition across a broad spectrum of plasma parameters and incident species. In conclusion, this study demonstrates that, through the utilization of the P_{nr} approach, it is feasible to construct a NN that, in conjunction with gross sputtering formulas, can quantify net erosion fluxes in full-scale W-based machines like WEST [15]. This methodology can be adapted to more complex models that account for factors such as collisions and other target materials beyond W, although at the expense of recalculating the associated probability maps for non-redeposition. The following section 3.1.3, delves into the model's applicability upon which the NN is founded.

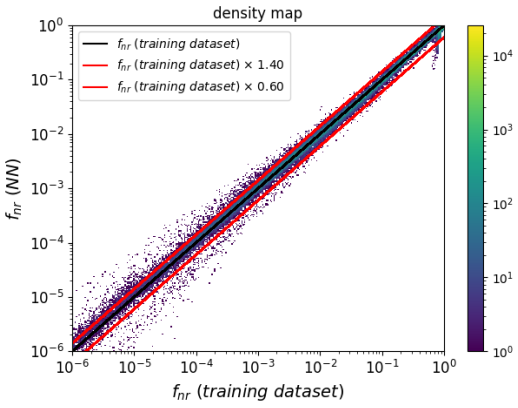

Figure 3.2: Density map of $f_{non-redep}$ calculated with the NN compared to $f_{non-redep}$ Monte Carlo values.

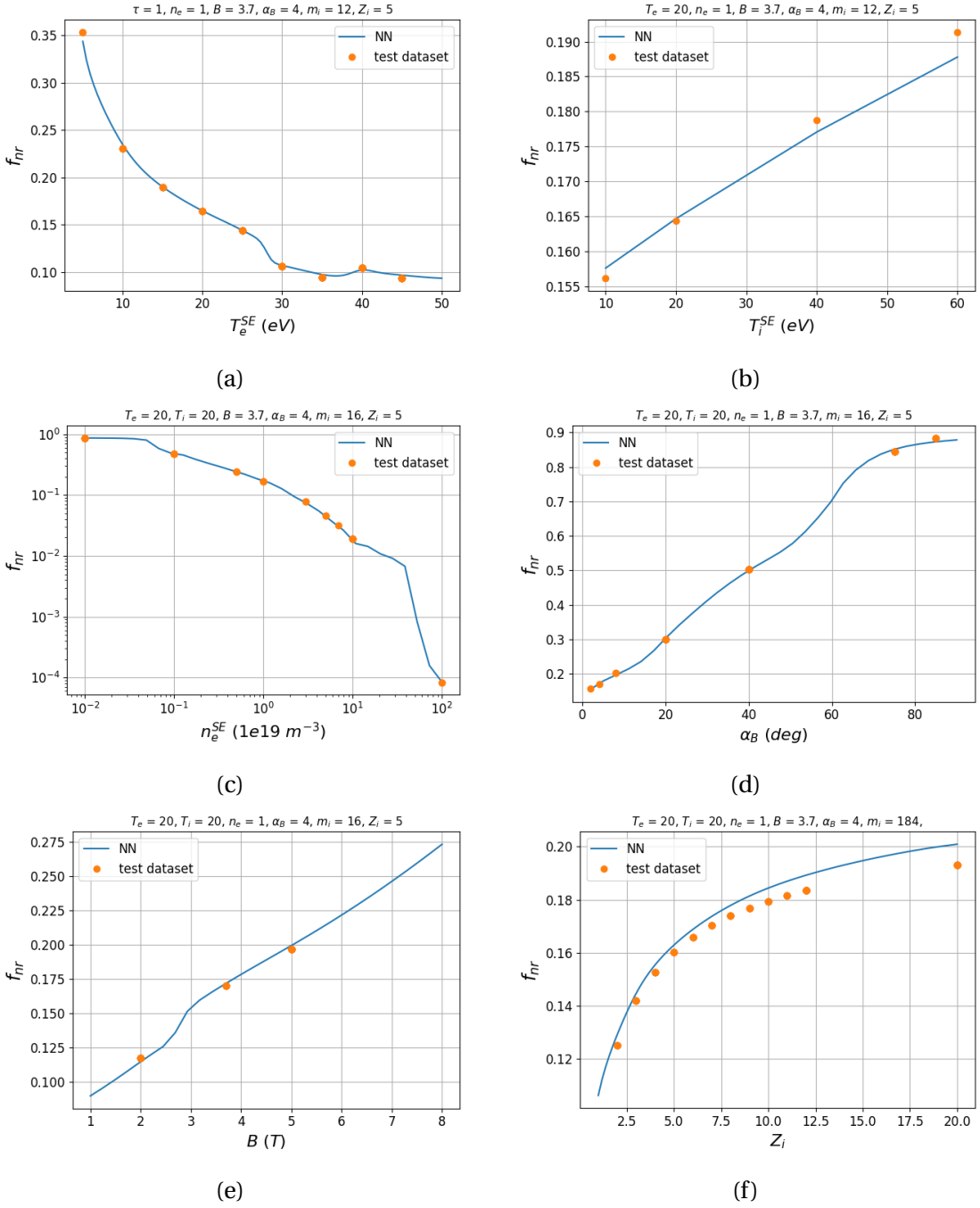

Figure 3.3: NN interpolation and extrapolation compared to test dataset. Title quantities are reported in the same units as in table 3.1

3.1.3 Prompt redeposition or total redeposition? What is best for a fluid plasma solver

Redeposition is approximately a local phenomenon with a characteristic length in the order of the first ionization Larmor radius $L_{redep} \sim \rho_L$. Nonetheless, if the concept of total redeposition is applied, non-promptly redeposited particles have a larger redeposition characteristic length which is on the order of the sheath width divided by the sine of the magnetic angle ($L_{redep} \sim \lambda_{sheath}/sin(\alpha_B) \sim \rho_L/sin(\alpha_B)$), see figure 3.4. Therefore, the redeposition of ions that are not promptly redeposited does not exhibit locality at shallow incident magnetic angles. As a result, the assumption of a collisionless domain and uniformity for parameters like T_e^{SE} and n_e^{SE} can be invalid depending on the specific situation. Essentially, this model cannot effectively account for the substantial uncertainty associated with non-promptly redeposited particles. A better strategy would be to limit the application of the model to prompt redeposition. In this way, locality is respected and collisions are incorporated in the fluid solver that will be coupled to this source model.

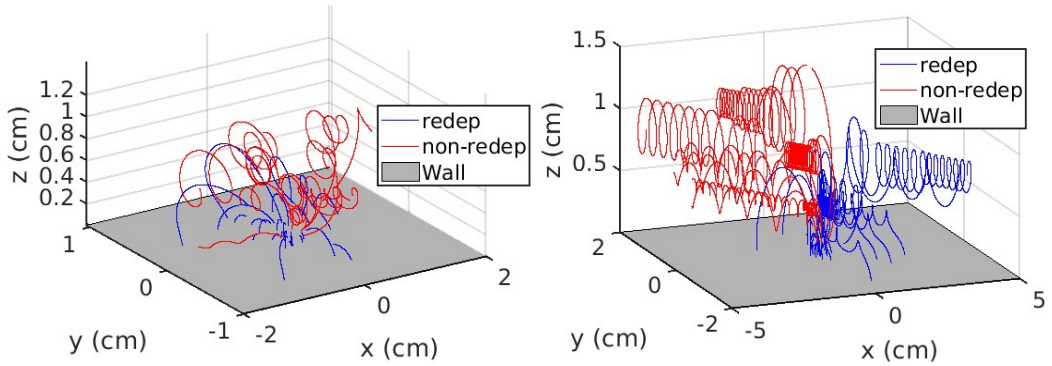

(a) prompt redep

(b) total redep

Figure 3.4: Trajectories of W ions in a collisionless plasma background with $T_e = 20\ eV$, $n_e^{SE} = 5e18\ m^{-3}$, $B = 3\ T$ and $\alpha_B = 4\ deg$. Prompt redeposition (a) has a smaller L_{redep} compared to total redeposition (b).

Given the previously discussed points, it is advisable to avoid integrating the neural network (NN) with a fluid solver, as the NN is specifically trained for total redeposition. Another challenge arising from NN utilization pertains to the potential drop. Training the NN to encompass all potential drop shapes would demand a substantial volume of data, making it difficult to produce. Consequently, these factors have steered the focus towards developing a flexible analytical reduced model for the W net source based on the prompt fraction instead of f_{redep}, and capable to deal with any stationary potential drop in the sheath.

3.2 Analytical model to estimate prompt redeposition

In this section, a one-dimensional analytical model is proposed to estimate the fraction of particles promptly redepositing, based on the same assumption listed in chapter 2. The eroded surface is planar and perfectly smooth, and the background plasma is considered static in time without fluctuations. Since the subject is prompt redeposition, the erosion time is limited to the first Larmor period T_L of the sputtered species ionized once. Collisions are assumed to be negligible and the only forces involved are the electric field and Lorentz force. Sputtered particle ionizations are only caused by electronic excitation while recombinations are neglected. Sputtered neutrals energy distribution is assumed to be Thompson-like (see equation (2.6)). The poloidal (θ) distribution is cosinusoidal while isotropy is assumed for the azimuthal (ϕ) distribution. Coordinates are spherical and Ω is the solid angle such that $d\Omega = sin(\theta)d\theta d\phi$. The resulting angular distribution is reported in equation 3.1.

$$SEAD(\theta,\phi) = \left(\int SEAD(E,\theta,\phi)dE\right)d\Omega = \pi^{-1}cos(\theta)sin(\theta)d\theta d\phi \tag{3.1}$$

Lastly, the potential drop within the sheath is adopted from [59], and all presented results in this chapter are computed under the condition of a sheath thickness of $2\rho_D \cos(\alpha_B)$.

3.2.1 Energetic redeposition

To begin, let us study the electron ionization of a neutral particle with velocity vector $\vec{v}$ immersed in a plasma. For a static plasma, its average ionization length λ is equal to the ratio of its velocity module (v) to the ionization frequency. In case of electron-ionization the frequency of ionization is $\omega_{ion} = n_e S(n_e, T_e)$, thus depends on plasma electron temperature and density.

$$\lambda = \frac{v}{\omega_{ion}} \tag{3.2}$$

Unless λ is relatively small, a neutral particle encounters variable density and temperature conditions during its path before ionization. Therefore, the average ionization length should be calculated by considering the average ionization frequency of the path (denoted as $\overline{\omega_{ion}}$) followed by the particle, as reported in equation (3.3). In the case of a sputtered neutral particle originated from a planar surface, if z is the direction perpendicular to the surface and z_0 is the surface position, the average ionization length $\overline{\lambda_z}$ is equal to the ratio of the initial velocity v_z to the average ionization frequency, equation (3.4).

$$\overline{\omega_{ion}} = \frac{1}{\overline{\lambda_z}} \int_{z_0}^{\lambda_z} \omega_{ion} dz \tag{3.3}$$

$$\overline{\lambda_z} = \frac{v_z}{\overline{\omega_{ion}}} \tag{3.4}$$

From the equations (3.3) (3.4) it is found that the velocity v_z required to ionize on average at a perpendicular distance $\overline{\lambda_z}$ is equal to the integral of the ionization frequency ω_{ion} along z. Therefore, if the plane located at $z_0 = 0$ identifies the eroded surface position, the average velocity v_z that a sputtered particle ionizing in $\overline{\lambda_z}$ has, is given by the equation (3.5).

$$v_z = \int_0^{\overline{\lambda_z}} \omega_{ion} dz \tag{3.5}$$

The mean perpendicular ionization distance, denoted as $\overline{\lambda_z}$, is equivalent to the first moment of the ionization probability density function (PDF) along the z axis for a neutral particle with a given initial velocity $\vec{v}$, as defined in equation (3.7). Assuming symmetry with respect to the azimuthal angle ϕ, the PDF, represented as $f(\lambda_z|E,\theta)$, depends solely on the particle's initial energy and poloidal angle. The ionization probability within the interval λ_z to $\lambda_z + dz$ is determined by the product of the probability of not ionizing up to λ_z times the probability of ionizing within the interval λ_z to $\lambda_z + dz$. The probability that a neutron does not ionize up to a distance λ_z was introduced in section 2.2.2.1 and derived through a simple static 1D Vlasov equation (equation (2.10)). Consequently, the ionization distribution can be expressed as shown in equation 3.6:

$$f(z|E,\theta)dz = \frac{1}{\lambda_z} e^{-\int_0^z \frac{dz'}{\lambda_z}} dz \tag{3.6}$$

As anticipated, the first moment of the ionization distribution $f(z|E,\theta)$ is equal to $\overline{\lambda_z}$ (see equation (3.7)), which is also equal to the velocity to ionization frequency ratio reported in equation (3.4).

$$\int_0^{\infty} f(z|E,\theta) z dz = \overline{\lambda_z} \tag{3.7}$$

The mathematical derivation to prove that equations (3.7) and (3.4) are equivalent, to date was not found. The challenge resides in analytically solving the integral of λ_z, since it is a function of the electron density decay n_e (see equation (2.11)), hence, of the Boltzmann factor. Anyway, the equivalence was proved numerically and was also compared with Monte Carlo results, see figure 3.5. It is worth noting that the numerical estimation of the mean free path deviates from the analytical one as energies increase. This discrepancy is attributed to the lower number of particles populating the high-energy tail, resulting in insufficient sampling for $E_z > 30$ eV, leading to a poor statistical representation.

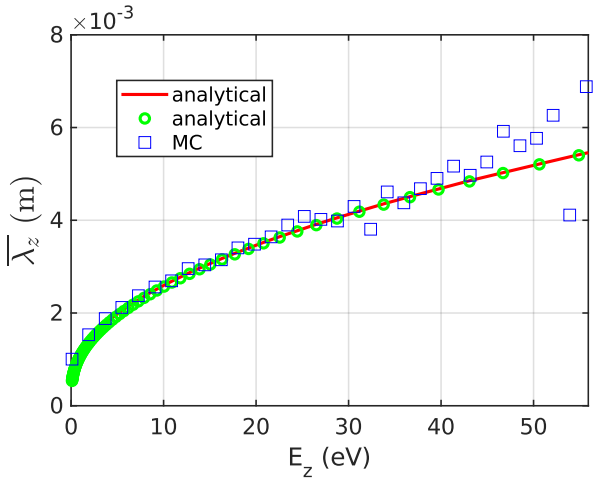

Figure 3.5: Bombardment of N^{+5} over W. Comparison of analytical (red line refers to equation (3.5), while green circles refer to equation (3.7)) and Monte Carlo (MC) results for the average ionization length $\overline{\lambda_z}$ as function of the initial kinetic energy of neutral sputtered W atom along the z axis. MC estimates are less accurate for higher energies since it is hard to analogically sample the tails of the sputtered distribution. The plasma background for this figure is characterized by a $n_e = 5e18\ m^{-3}$, $T_e = T_i = 20\ (eV)$, $B = 3\ T$, and $\alpha_B = 4\ deg$.

Once the ionization distance of a neutral particle is determined, it also establishes the force that the electric field will exert on it after ionization. Specifically, ionized particles within the sheath can overcome the electric potential barrier ϕ only when their initial kinetic energy along the z direction exceeds the potential drop at the ionization position, i.e., if $E_z > -\phi(z)$. If particles undergo ionization in a potential well greater than their initial kinetic energy, they will inevitably redeposit. If the electric potential within the sheath monotonically decreases there is a unique ionization length identifying the threshold distance λ_z^* below which a particle characterized by E,θ will redeposit. The length λ_z^* serves as a distinguishing factor between particles with $\lambda_z \leq \lambda_z^*$, which will re-deposit due to the electric field, and particles with $\lambda_z > \lambda_z^*$, which overcome the electric field and may have a chance to contaminate the plasma. Once the SEAD is known, it is possible to calculate the fraction, denoted as f_R^E, of redeposited particles due purely to the electric field force, as shown in equation (3.8).

$$f_R^E = \int SEAD(E,\theta)\left(\int_0^{\lambda_z^*(E,\theta)} f(z|E,\theta)dz\right)dEd\theta \tag{3.8}$$

To determine the threshold distance λ_z^*, the potential ϕ must be inverted to locate the point where it is equal to the initial energy along z: $E_z = Ecos(\theta)^2 = -\phi(\lambda_z^*)$. Following the same line of reasoning the threshold distance λ_z^* can also be used to calculate the SEAD of particles overcoming the electric field, as shown in equation (3.10). The fraction of particles $1 - f_R^E$ ionizing far enough (i.e. $\lambda_z > \lambda_z^*$) is denoted as

NE.

$$f^{NE} = SEAD(E,\theta)\left(\int_{\lambda_z^*(E,\theta)}^{\infty} f(z|E,\theta)dz\right) \tag{3.9}$$

$$SEAD^{NE} = f^{NE} \Big/ \int f^{NE} dE d\theta \tag{3.10}$$

An important parameter is the average threshold distance $\overline{\lambda_z^*}$ of the sputtered population. It is identified by reversing the average energy balance function (denoted as h) at zero, see equation (3.11). This parameter will be used in section 3.2.4 as a substitute of the sheath width λ_{sheath} to redefine the parameter $\hat{\lambda}$ introduced in section 2.4.1, equation (2.16).

$$h \equiv \frac{1}{2} m \left(\int_0^{\lambda_z} \omega_{ion} dz\right)^2 + \phi(\lambda_z) \tag{3.11}$$

$$\overline{\lambda_z^*} = h^{-1}(0) \tag{3.12}$$

The first moment of the ionization distribution $f(z|E,\theta)$ could provide a more computationally efficient way to estimate f_R^E compared to the calculations required by equation (3.8). This is accomplished by introducing the concept of the minimum average exit energy, denoted as $\overline{E_m}$. This represents the lowest mean energy required for a particle to overcome the potential drop at the average ionization position $\overline{\lambda_z^*}$.

$$\overline{E_m}(\theta) \equiv \begin{cases} \frac{|\phi(\lambda_z^*)|}{cos^2(\theta)}, & \text{if } \phi(\overline{\lambda_z^*}) < 0 \\ 0, & \text{otherwise} \end{cases}$$

An approximation of the fraction of energetically redeposited particles f_R^E is now computable if the SEAD at the wall is known, as reported in equation (3.13).

$$f_R^E \approx \int \int_0^{E_m} SEAD(E,\Omega) dE d\Omega \tag{3.13}$$

In figure 3.6a, $1 - f_R^E$ is depicted as function of the average ionization length $\overline{\lambda_z}$ of sputtered W neutrals, normalized by the distance $\overline{\lambda_z^*}$. If $\overline{\lambda_z} < \overline{\lambda_z^*}$, $1 - f_R^E$ falls rapidly and the difference between the full kinetic calculation with respect to the first moment approximation decreases. Figures 3.6a and 3.6b were obtained calculating the f_R^E associated with a population of neutral W particles sputtered by an incident flux of nitrogen ions (N^{+5}) while varying the electron density at the sheath entrance. Figure 3.6b show the same data points but in relation to the electron density.

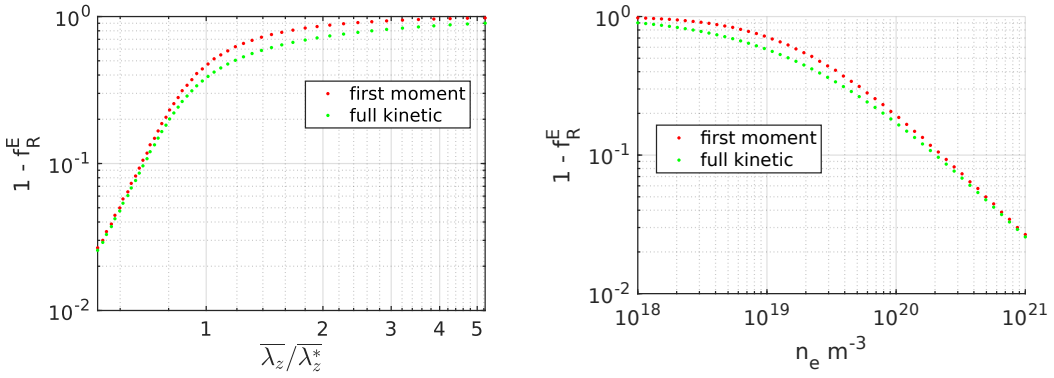

(a) (b)

Figure 3.6: Fraction of W particles overcoming the sheath potential according to equations (3.8) (full kinetic) and (3.13) (first moment). Depicted results refer to the sputtering of W due to a flux of nitrogen ions (N^{+5}) with a variable electron density at the sheath entrance. All other parameters were fixed: $T_e = T_i = 20\ (eV)$, $B = 3.7\ T$, and $\alpha_B = 4\ deg$.

Similarly as before, also the sputtered energy and angular distribution of the neutral fraction $1 - f_R^E$ can be approximated using the first moment. Particles surpassing the potential barrier and ionizing at $\lambda_z > \lambda_z^*$ exhibit a distinct energy and angle distribution from that at the wall. Since the low-energy portion f_R^E of particles is lost due to redeposition, the energy distribution will be shifted to higher values. At the same time, the angular distribution tends to peak towards $\theta = 0$ because particles with large poloidal angles, as indicated in equation (3.2.1), are rapidly lost. The angular distribution of the $1 - f_R^E$ fraction is therefore obtained by multiplying the angular distribution at the wall by the probability that a sputtered particle with a given poloidal angle θ will undergo energetic redeposition, see figures 3.7b and 3.7d.

$$SEAD(\theta)^{NE} \approx \frac{SEAD(\theta)\left(1 - \int_0^{E_m(\theta)} SEAD(E)dE\right)}{\int_0^{\pi/2} SEAD(\theta)\left(1 - \int_0^{E_m(\theta)} SEAD(E)dE\right)d\theta} \tag{3.14}$$

However, the particles are subsequently deflected by the remaining potential $\phi(\lambda_z^*)$ and their redeposition probability depends on other phenomenon such as gyromotion and the cone of loss, see section 2.4.1.1. Therefore, the equation (3.14) can't be used to represent the distribution of particles undergoing redeposition related to their gyromotion and it is only used to estimate the $1 - f_R^E$ average energy in equation (3.18).

The energy distribution is derived by eliminating the fraction of particles with energy lower than the minimum energy, as indicated in equation (3.2.1).

$$f_R^E(\theta) \approx \int_0^{E_m(\theta)} SEAD(E,\theta)dE \tag{3.15}$$

Therefore, the energy distribution function of particles not subject to electrical redeposition can be approximated as shown in equation (3.17).

$$SEAD(E|\theta) \approx \int \frac{SEAD(E)\,H(E-E_m(\theta))}{1-f_R^E(\theta)}d\theta \tag{3.16}$$

$$SEAD(E)^{NE} \approx \int f_{E|\theta} f_\theta d\theta \tag{3.17}$$

The average energy $\overline{E}_{NE}$ for the $1-f_R^E$ fraction is known.

$$\overline{E}_{NE} = \int SEAD^{NE}(E)EdE \tag{3.18}$$

The energy distribution of the non-promptly redeposited (NP) fraction, as presented in equations (3.10), (3.17), and (3.14), was compared with a series of Monte Carlo results. Figure 3.7 illustrates the analytical and Monte Carlo estimates of the SEAD for both the non-promptly redeposited (denoted as NP) and $1-f_R^E$ (denoted as NE) populations. In line with the overall text, the focus is exclusively on the SEAD dependency on energy and poloidal angle. Rather than representing the SEAD as 2D maps, the trends related to energy and poloidal angle are displayed into two distinct figures. Specifically, figures 3.7a and 3.7b illustrate the energy and angular distribution of the NE and NP populations when the electron density at the sheath entrance is set to 5e18 m^{-3} while keeping other sheath parameters constant. Similarly, figures 3.7c and 3.7d portray the energy and angular distribution of the NE and NP populations when the electron density at the sheath entrance is 5e19 m^{-3} with the remaining sheath parameters unchanged with respect to the lower density case. In figures 3.7a and 3.7c one sees that for both electron densities, the full kinetic description of the NE energy distribution accurately represents the energy distribution of the NP population, suggesting that the probability of redeposition associated with $1-f_R^E$ is indeed energy-independent. However, is anticipated here that this is not universally true. If the ratio $\overline{\lambda_z}/\overline{\lambda_z^*}$ is less than one, particles ionize on average inside the sheath, and the probability of redeposition for the NE fraction will also depend on energetic considerations. Conversely, the angular distribution of the NE and NP populations are different for both electron densities, see figures 3.7b and 3.7d. This is because the $1-f_R^E$ fraction redeposition is always angular-dependent. Therefore, the $SEAD^{NP}$ is influenced by other factors, such as gyromotion and the cone of loss (see section 2.4.1.1), which are not included in the derivation of $SEAD^{NE}$, thus, unless the sheath effect on redeposition is negligible, the angular distribution of the $1-f_R^E$ population cannot be used to approximate the NP angular distribution.

3.2.2 Geometric redeposition

As anticipated in the previous section, the fraction $1-f_R^E$ not energetically redeposited could still redeposit. There are two primary redeposition pathways, both linked to a

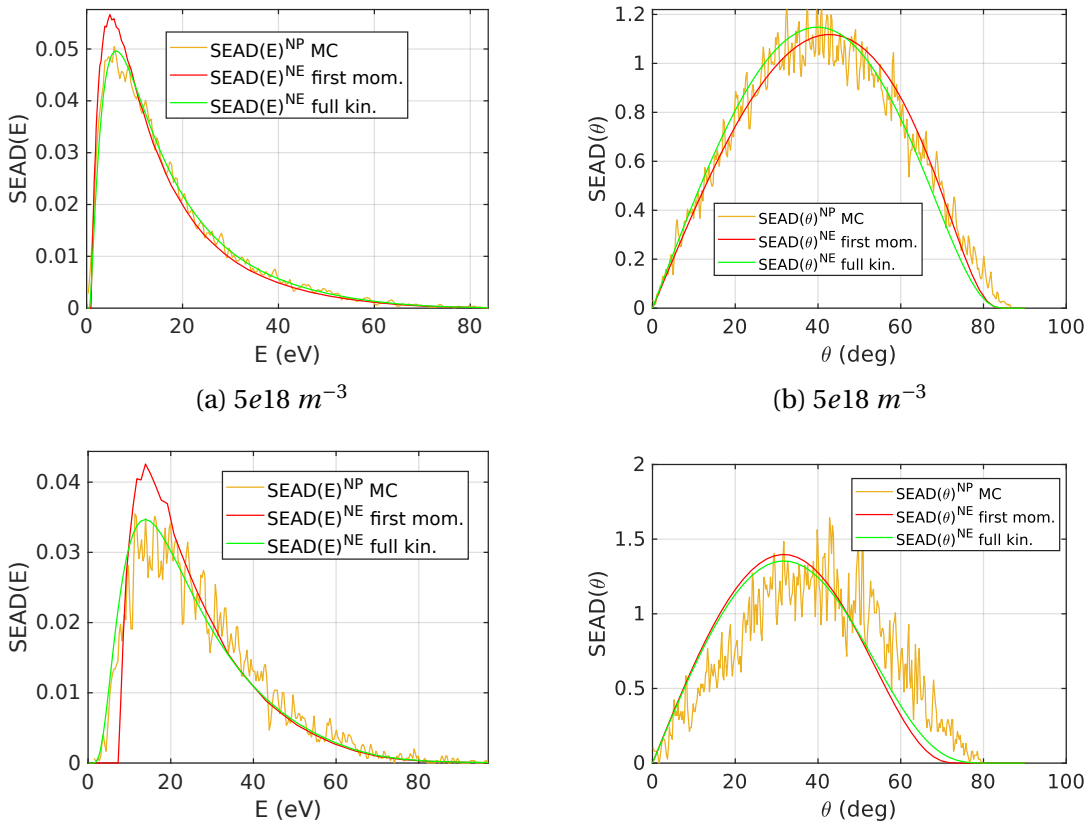

(a) $5e18\ m^{-3}$ (b) $5e18\ m^{-3}$

(c) $5e19\ m^{-3}$ (d) $5e19\ m^{-3}$

Figure 3.7: SEAD(E) and SEAD(θ) of sputtered neutral W caused by a flux of nitrogen ions (N^{+5}), estimated with Monte Carlo for two different electron densities at the sheath entrance $n_e = 5e18\ m^{-3}$ and $n_e = 5e19\ m^{-3}$. All other parameters are fixed: $T_e = T_i = 20\ (eV)$, $B = 3.7\ T$, and $\alpha_B = 4\ deg$.

corresponding redeposition probability or fraction. A particle can redeposit because of its gyromotion bringing it back to the surface, or due to a combination between gyromotion and electric field attraction. The corresponding probabilities are here denoted as f_R^G and f_R^{GE}, respectively. As demonstrated in prior studies [74] the redeposition probability f_R^G primarily depends on the parameter $p = \lambda/\rho_{L^{+1}} = \omega_L/\omega_{ion}$. This parameter represents the ratio between the ionization length of the neutrally sputtered particles to their first-ionization Larmor radius, and it is independent of both particle initial energy and azimuthal angle. According to this model the redeposition is also independent of the magnetic field direction, which is considered parallel to the surface. In figure 3.8 is depicted the geometrical redeposition according to this simplified model. Redeposition thus concerns all those particles whose θ angle is such that the ratio p_z reported in equation (3.19) is less then or equal to 1. There threshold angle such that $p_z = 1$ is denoted as θ_{lim}.

$$p_z = \frac{\lambda cos(\theta)}{\rho_L(1+sin(\theta))} = \frac{pcos(\theta)}{(1+sin(\theta))} \tag{3.19}$$

The fraction $f_p = f_R^G$ is than calculated integrating the poloidal angular distribution from θ_{lim} to $\pi/2$.

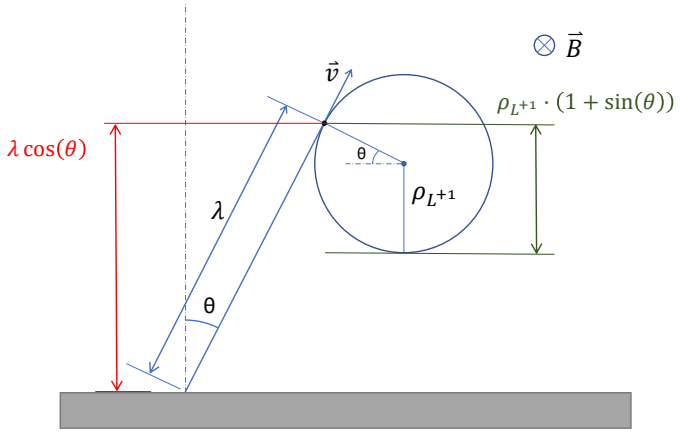

Figure 3.8: Redeposition according to [74]. λ is the ionization length, $\rho_{L^{+1}}$ is the Larmor radius of first ionization.

In equation (3.20) is reported θ_{lim} according to [74], which can be derived solving $p_z = 1$. The equation (3.20) is valid for any poloidal distribution.

$$\theta_{lim} = asin\left(\frac{p^2-1}{1+p^2}\right) \tag{3.20}$$

$$f_R^G = \int_{\theta_{lim}}^{\pi/2} SEAD(\theta)\, d\theta \tag{3.21}$$

In reality, the fraction f_p tends to f_R^G in the limit $\tilde{\lambda} = \overline{\lambda_z}/\overline{\lambda_z^*} \to \infty$. Conversely, if the ionization length is smaller than the distance $\overline{\lambda_z^*}$ redeposition is mostly related to the electric field. However, at least for grazing α_B angles and large, the model proposed in [74] provides a reasonable estimate of f_p even for $\tilde{\lambda} < 1$ because the lack of multiple ionization tends to compensate the non physical assumption of $f_R^E = 0$, see figure 3.9. Additionally, the inaccuracy becomes more pronounced with larger angles α_B. In the following chapters, an attempt is made to model f_R^G for any α_B and $\tilde{\lambda} < 1$. For clarity, it is important to note that the comparison in figure 3.9 was conducted without utilizing the formula proposed for the prompt fraction $f_p = 1/(1+p^2)$ in [74]. This is because the formula is valid only for SEAD$(\theta) = cos(\theta)$ which does not align with the conditions in this work, see equation (3.1).

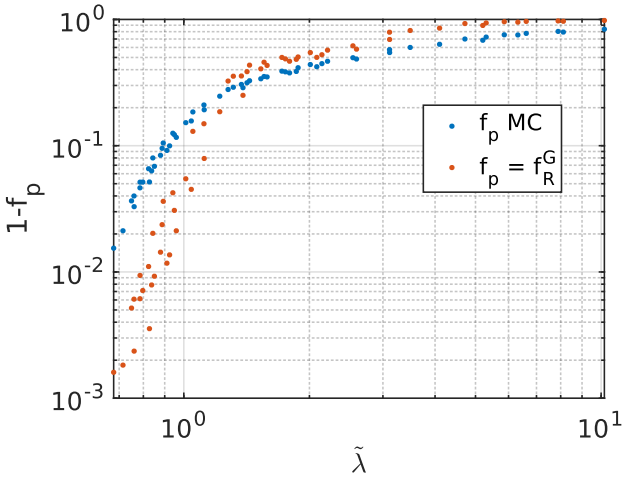

Figure 3.9: Fraction of non prompt redeposited W sputtered by a flux of W ions (W^{+15}). The angle of incidence is fixed $\alpha_B = 4\ deg$ while $T_e \in [15,30]$ eV, $n_e \in [1e18, 1e20]$ m^{-3} and $B \in [2,5]$ T.

3.2.2.1 Multiple ionization

When considering redeposition related to the gyromotion of ions, it is crucial to account for multiple ionization, as the Larmor radius depends on the ion charge. This section introduces an approximate model to estimate the average charge of non-promptly redeposited ions. The challenge is that an accurate model would require tracking particle trajectories. Fortunately, sputtered particles more likely to overcome the electric field are those ionizing closer to the sheath entrance, where the Boltzmann factor is close to unity and the density is roughly constant. Hence, escaping particles can be viewed as traveling in a homogeneous medium, and their transport does not need to be solved. In the limit of coronal equilibrium, where recombination is disregarded and only electron ionization is considered, the time evolution of each ionization state of the $1 - f_R^E$ population can be described by a series of first-order differential equations, as follows.

$$\begin{cases} \psi_1 = e^{-C_1 t} \\ \partial_t \psi_i = -\psi_i C_i + \psi_{i-1} C_{i-1}, \quad \text{if i} > 1 \end{cases} \tag{3.22}$$

Here, $\psi_i(t)$ represents the fraction of particles in the i-th ionization state at time t, and C_i stands for the ionization sink/source term denoting the transition from ionization state i to i+1, as previously introduced in equation (2.9). The C_i terms are calculated assuming all plasma being at the sheath entrance condition (e.g. $n_e = n_e^{SE}$) during the whole Larmor period. At $t = 0$ all particles are in their first ionization state ($\psi_1 = 1$ and $\psi_{i>1} = 0$). The time evolution of the average ionization state is then expressed as the summation of the population fractions ψ_i multiplied by their corresponding ionization states, see equation (3.23).

$$\overline{Z}(t) = \sum_i \psi_i i \tag{3.23}$$

Assuming a uniform background is a good approximation for the average charge of the non prompt fraction $(1 - f_p)$ because it is made up of those particles who did not redeposit, hence the average ionization $\overline{Z_{np}}$ is equal to $\overline{Z}$ at $t = T_L$. However, such approximation is not perfectly suited to get the average ionization of the $1-f_R^E$ fraction. In reality, particles that do not electrically redeposit can still travel partially inside the sheath where the density and temperature of electrons are lower. Additionally, redeposited particles are absorbed and have less time to undergo multiple ionization events. This is why the average ionization of the $1 - f_R^E$ population is expressed in equation (3.24) as an average between the charge of the non-prompt population and the charge state ($Z = 1$) of the electrically redeposited f_R^E fraction.

$$\overline{Z} \approx f_R^E + (1 - f_R^E)\overline{Z_{np}} \tag{3.24}$$

The approximation for $\overline{Z_{np}}$ was tested for a wide range of electron temperature, density and magnetic field vector showing a good agreement in almost all cases, see figure 3.10.

3.2.2.2 Redeposition for non grazing magnetic field angle

In addition to multiple ionization, another crucial parameter influencing redeposition is the magnetic angle α_B, which impacts both energetic and geometric redeposition. As α_B increases the magnetic presheath shrinks and as α_B approaches 90 degrees, most of the potential drop is narrowed in the Debye sheath, thus close to the eroded surface (see equation (1.24)). Consequently, only sputtered neutrals with small energy (i.e. small mean free path) will ionize in the Debye sheath where a strong electric field redeposit them. Most particles will not redeposit because of the electric field force, thus the $1 - f_R^E$ fraction is directly correlated to α_B. In other words is like saying that there exists a negative correlation between the average threshold distance $\overline{\lambda_z^*}$ and α_B. Concerning redeposition associated with gyromotion, the cosine of the magnetic angle α_B represents the projection of the helical motion onto the z-axis. Thus, as $\alpha_B \to \pi/2$, no particles will redeposit due to their gyromotion. Another impact of α_B on f_R^G is linked to the perpendicular component of the velocity (denoted as $v_\perp$) which is directly proportional to the Larmor radius. For varying α_B the solid angle where the perpendicular velocity tends to zero called Ω_{loss}, will vary, and with it the number of particles sputtered in that particular direction. It is interesting to notice that if the average potential drop crossed by ionized sputtered particles is not negligible compared to their average initial energy, ions will be deflected, altering the relationship between the sputtered number of neutral particles in $d\Omega_{loss}$ and the actual number of ions that ultimately fall within it.

While the relationship between α_B and f_R^E is already incorporated into the model, the effect of α_B on gyromotion has not been included yet. To address this, it is nec-

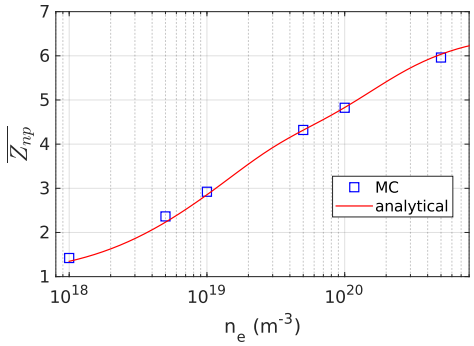

(a) $T_e = 20\ eV$, $B = 3\ T$, $\alpha_B = 4\ deg$

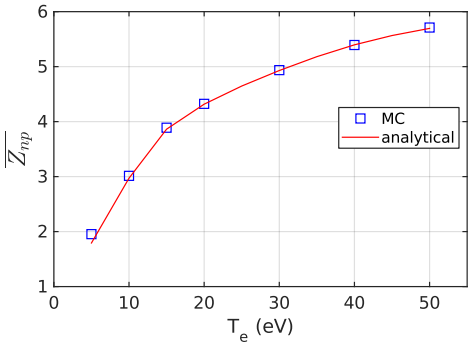

(b) $n_e = 5e19\ m^{-3}$, $B = 3\ T$, $\alpha_B = 4\ deg$

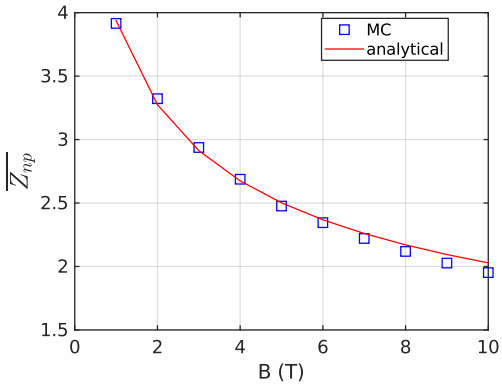

(c) $n_e = 1e19\ m^{-3}$, $T_e = 20\ eV$, $\alpha_B = 4\ deg$

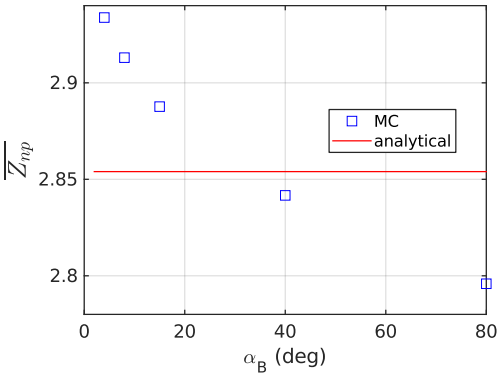

(d) $n_e = 1e19\ m^{-3}$, $T_e = 20\ eV$, $B = 3\ T$

Figure 3.10: average ionization state $\overline{Z_{np}}$ of non-promptly redeposited W atoms. Comparison between the simplified model (analytical - red line) proposed in section 3.2.2.1 and Monte Carlo results (MC - blue squares).

essary to look at the dependence of the perpendicular velocity with respect to the magnetic field direction. Once the magnetic field azimuthal angle is fixed, for instance $\phi_B = \pi$, the perpendicular velocity depends on α_B as reported in equation 2.19. Instead of using such complicated formula it is preferred to work with the perpendicular velocity averaged with respect to the sputtered particles' azimuthal distribution. The sputtered azimuthal ϕ distribution is considered uniform; thus, the averaged perpendicular velocity, denoted as $\overline{v_\perp}(\theta, \alpha_B)$, is expressed as in equation (3.25).

$$\overline{v_\perp} = v\sqrt{sin(\theta)^2\left(1 - 1.5cos(\alpha_B)^2\right) + cos(\alpha_B)^2} \tag{3.25}$$

Such a formula could be utilized to modify the p_z parameter reported in (3.19) to extend the previous geometrical redeposition model from [74] for all α_B angles. Here, an attempt is made to calculate the geometrical deposition by modifying the model from [74] using another definition of p_z that accounts for multiple ionization and varying α_B.

Once the perpendicular to B velocity is known, the average projection of the Larmor

radius of a population with average ionization state $\overline{Z}$ along the z-axis is then equal to the product of the Larmor radius, the cosine of α_B, and the ratio $\overline{v_\perp}/v$. Thus, p_z is redefined as follows.

$$p_z = \frac{v}{\overline{v_\perp}(\theta)} \frac{\overline{Z}\omega_L cos(\theta)}{\omega_{ion}^{SE}(1+sin(\theta))cos(\alpha_B)} \tag{3.26}$$

In analogy with equation (3.19), a novel definition for the parameter p is derived, and it is presented in equation (3.27). The ionization frequency is taken at the sheath entrance (SE) because the assumption is that particles undergo ionization outside the sheath. The estimate f_R^G is now expanded for each magnetic incidence angle and encompasses multiple ionization.

$$p = \frac{\omega_L \overline{Z}}{\omega_{ion}^{SE}(cos(\alpha_B))} \tag{3.27}$$

To find the solution for $p_z = 1$ it is required to solve a third-order polynomial, see equation 3.28. Mathematically, the polynomial has always three roots even if only real roots have a physical meaning, thus from 1 up to three values of θ_{lim} may arise. The emergence of three real solutions occurs for small $p \ll 1$, normally associated to $\lambda_z^* \ll 1$, where the cone of loss effect kicks-in as discussed in section 2.4.1.1. A comparison between equation (3.19) from [74] and the new definition proposed here in equation (3.26) is illustrated in figure 3.11.

$$\Theta = (y^3 + y^2)(1 - 1.5cos(\alpha_B)^2) + y(cos(\alpha_B)^2 + p^2) + cos(\alpha_B)^2 - p^2 = 0 \tag{3.28}$$

$$\theta_{lim} = asin(root(\Theta))$$

As in [74] , the redeposited fraction related to gyromotion f_R^G is obtained by integrating the poloidal distribution at the wall along the interval of θ where $p_z \leq 1$. In equation (3.2.2.2) is shown an example on how to calculate f_R^G in a spherical coordinate system with only one real root, complex roots are discarded.

$$f_R^G = \begin{cases} \int_{\theta_{lim}}^{pi/2} SEAD(\theta)d\theta, & \text{if } \theta_{lim} \geq 0 \\ \int_0^{-\theta_{lim}} SEAD(\theta)d\theta + 0.5, & \text{otherwise} \end{cases}$$

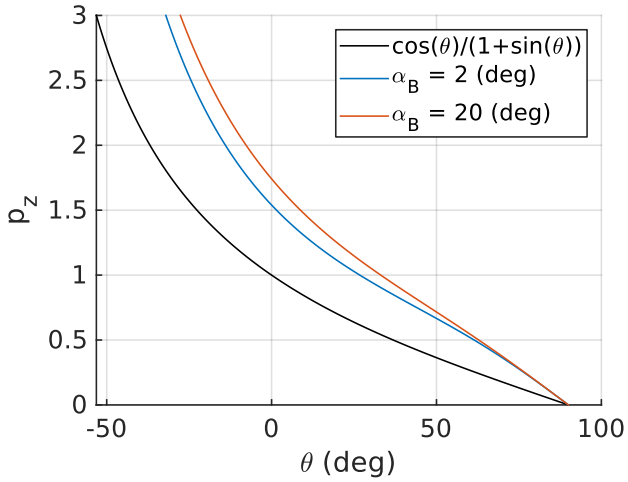

Figure 3.11: Z-projection of the ratio between the ionization length and Larmor radius, as per [74] (black line), and in accordance with Equation (3.26) for two distinct angles α_B, with imposed $\overline{Z} = 1$. In these conditions the polynomial in equation (3.28), has only one real root, hence there is a unique value of θ_{lim}.

The new definition of p is proportional to the average ionization state of sputtered particles. Equation 3.24 reports the approximation adopted for $\overline{Z}$.

3.2.3 Collisional sheath

Throughout the whole previous discussion collisions were neglected. The fundamental assumption is that the plasma sheath is characterized by low collisionality, and momentum exchanges between the plasma and impurities are considered negligible. The impact of collisions is not addressed, and the collisionless assumption persists. Anyway this section is dedicated to inspect the validity of this approximation.

Generally, collisions can either propel ions toward the plasma, thereby reducing f_p, or push them towards the eroded surface, increasing f_p. The force imparted by collisions can be decomposed into two parts: a drift force $\vec{F}_D$, and a thermal force $\vec{F}_{\nabla T}$ related to thermal gradients [103]. The two forces are competing; the drift repels particles toward the wall while the thermal force pushes them toward the plasma. As shown in [77] the predominant force for particles ionizing inside the sheath is the electromagnetic force. On the other hand, the thermal force of the background ions $\vec{F}_{\nabla T_b}$ just outside the sheath becomes more important increasing the number of nonredeposited particles by reducing f_R^G. That said, the second assumption of this model could result in an overestimation of the fraction f_R^G. Clearly, for very dense plasmas the drift force also becomes more important by counterbalancing the thermal force. Collisions can be neglected a priori for prompt redeposition only if the product between the interspecies collision frequency (ν_c) and the Larmor period (T_L) is smaller than one. Considering a background species b and a test particle a, the interspecies

ion collision is shown in equation 3.29, taken from [104]. The frequency depends on the background species density and temperature. For simplicity the Coulomb logarithm is considered constant $ln(\Lambda) \approx 17$ in the range of temperatures considered.

$$\nu_c = \frac{e^4}{12\sqrt{\pi^3 m_b}\epsilon_0^2} \frac{ln(\Lambda) n_b}{T_e^{\frac{3}{2}}} \tag{3.29}$$

In figure 3.12 the product $\xi = \nu_c \times T_L$ is plotted as function of sheath entrance temperature and density. As expected, collisionality becomes more and more important as temperature decreases and density increases. Conservatively a collisionless model should be applied only in the area where $\xi \lessapprox 1$. It should be kept in mind that in the sheath electrons experience both a temperature and density drop and the sputtered neutrals could ionize in a region where collisionality differs from that at the sheath entrance.

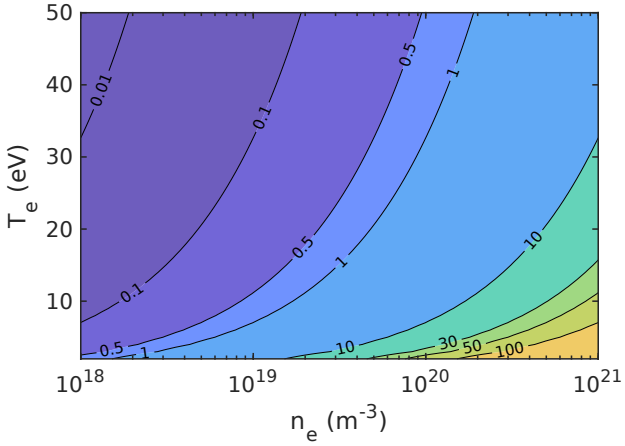

Figure 3.12: Collisionality ξ map for a range of electron density and temperatures at the sheath entrance

Despite in a large portion of operative conditions collisions cannot be disregarded, the purpose of this model is to be coupled with fluid solvers where collisions are included. Thus, at least the impurity transport outside the sheath will include the effect of collisions.

3.2.4 Two-groups theory

As mentioned in the previous chapter, the probability of prompt redeposition f_p can be described as the result of three distinct types of redeposition.

1. Energetic redeposition f_R^E
2. Geometric redeposition f_R^G
3. Geometric-energetic redeposition f_R^{GE}

It is called two-group theory, the model where f_R^{GE} is neglected, and the prompt fraction can be written as follows.

$$f_p = f_R^E + (1 - f_R^E) f_R^G \tag{3.30}$$

Where f_R^G is derived from Equation (3.2.2.2), and f_R^E from equation (3.8) or similarly from equation (3.13). The main assumption of the two groups theory is to consider the redeposition physics as if it were divisible into two distinct mechanisms, with the boundary located at a distance λ_z^* from the wall, defined in equation (3.12). The redeposition probability of the fraction of particles f_R^{GE} is assumed to be equal to that of the fraction f_R^G and they are treated as a single entity. In other words, it is assumed that the fraction $1 - f_R^E$ (whose ionization length is greater than λ_z^*) has much higher energy than the remaining potential drop $E(\lambda_z > \lambda_z^*) \gg \phi(\lambda_z^*)$. Consequently, the energy of the fraction $1 - f_R^E$ is approximately unaffected by the further deceleration due to the remaining potential barrier. To entirely remove the energy dependence for the $1 - f_R^E$ fraction, a second assumption is introduced. It is assumed that the angular distribution of the fraction $1 - f_R^E$ is equivalent to that at the wall, and consequently, the fraction f_R^G is calculated accordingly.

In figure 3.13 is depicted the comparison between numerical results from MC simulations taken as a reference and the estimate of the 2 groups theory, using a full kinetic description for f_R^E as reported in equation (3.8).

Data are plotted against the average ionization distance along z of the sputtered population at the sheath entrance, normalized with the energy-related redeposition threshold distance λ_z^* from the wall, defined in equation (3.12): $\hat{\lambda} \equiv \overline{\lambda_z}(n_e^{SE})/\overline{\lambda_z^*}$. This normalized distance is similar to the definition proposed in equation (2.16) in chapter 2, with the distinction lying in the normalizing quantity. In equation (2.16) the ionization distance is normalized with the sheath width considered proportional to the Deuterium Larmor radius $\lambda_{sheath} \propto \rho_D$. In contrast, here, the sheath width is redefined as equal to $\overline{\lambda_z^*}$ from equation (3.12). The redefinition of $\hat{\lambda}$ has demonstrated improved correlation with f_p compared to its previous definition in equation (2.16), as well as the normalized distance $\tilde{\lambda} = \overline{\lambda_z}/\overline{\lambda_z^*}$ used in figures 3.6 and 3.9.

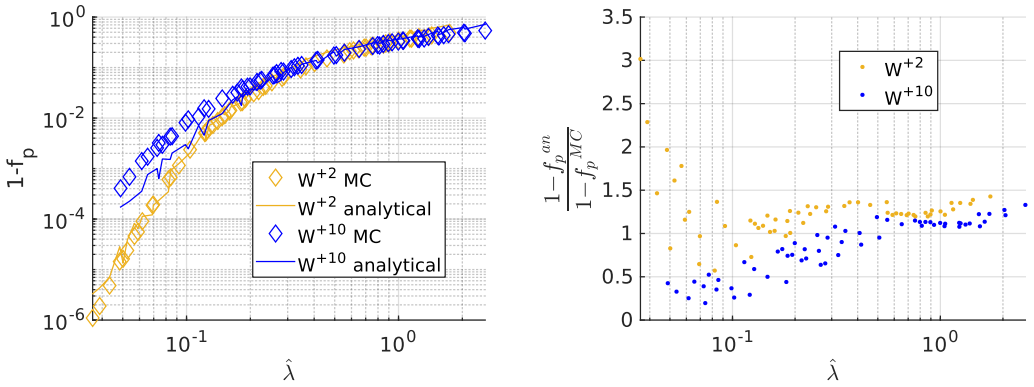

Figure 3.13: Ionic bombardment of W^{+2} and W^{+10} on W at a fixed magnetic angle $\alpha_B = 4\ deg$. The other parameters varied, $n_e \in [5e18, 5e20]$ m^{-3}, $T_e \in [15, 30]$ eV and $B \in [2, 5]\,T$.

Results show that the f_R^G can be considered energy independent only in the limit $\hat{\lambda} \gg 1$. This is clearly visible when sputtering is caused by two impinging ions with different ionization state, see figure 3.13. Indeed, as $\hat{\lambda}$ decreases, the curve $1 - f_p(\hat{\lambda})$ calculated with Monte Carlo splits into two branches, more rapidly than the analytical approximation. This indicates that f_R^G becomes energy dependent. To verify it, in figure 3.13b illustrates that the analytical model consistently underestimates (overestimates) the non-prompt redeposited fraction associated with W^{+10} (W^{+2}). The discrepancies become more pronounced as $\hat{\lambda}$ decreases. This behavior was consistently observed even with other impinging species. Another clue supporting the idea that the redeposition of the $1 - f_R^E$ fraction is energy-dependent is derived from the energy distribution SEAD$(E)^{NE}$ mentioned in section 3.2.2. When the ionization length of sputtered ions falls within the sheath, the analytical SEAD$(E)^{NE}$ diverges from the energy distribution of non-promptly redeposited ions, indicating that the energy of the $1 - f_R^E$ fraction is not conserved. This further implies that f_R^G becomes energy-dependent as well, in figure 3.14 is shown a dedicated example where the electron density was further increased compared to figure 3.7 to shorten $\overline{\lambda_z}$. As expected, the energy distributions of the NE and NP populations differ.

The model was also tested with respect to the angle α_B and results are presented in figure 3.15. The angular dependence introduced in equation (3.26) qualitatively reproduce the numerical trends, except made for the high density scenario where also a trend deviation for sputtering induced by high charged ions (e.g. W^{+10}) was observed. The deviation with respect to Monte Carlo results peaks around $\alpha_B \approx 60\ deg$, see figure 3.15d, while the sensitivity of f_R^G with respect to α_B is less pronounced than in Monte Carlo simulations. In conclusion, the two-groups theory is more accurate than the model proposed in [74], it includes more physics such as redeposition related to the electric field, multiple ionizations and the effect of a varying magnetic field angle α_B. As a consequence, the model can be applied for a wide range of plasma conditions

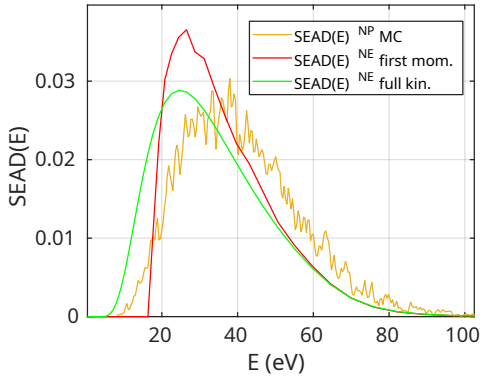

Figure 3.14: SEAD(E) of sputtered W caused by a flux of nitrogen ions (N^{+5}), estimated with Monte Carlo for the following conditions: $n_e = 2e20\ m^{-3}$, $T_e = T_i = 20\ (eV)$, $B = 3.7\ T$, and $\alpha_B = 4\ deg$.

at the sheath entrance. Unfortunately, the model breaks when the ionization length of sputtered ions falls within the sheath. Moreover, the model is less sensitive to the incident energy and magnetic angle α_B with respect to the Monte Carlo simulations used as a reference. Generally, the error is less than ±50% inside its regions of validity and for angles $\alpha_B \leq 20\ deg$. Furthermore, the model provides useful information about the non-prompt redeposited population, such as the average ionization charge ($\overline{Z_{np}}$), ionization state population fractions (ψ_i), and the average energy ($\overline{E}$).

3.2.5 Three-groups and tuning of the code

The two-groups theory can be refined by incorporating the fraction of particles redeposited due to both geometrical and energetical redeposition, denoted as f_R^{GE}. An analytical method to address the redeposition probability associated with this category of eroded particles has not been found. Hence, an adjustment of parameters in the two-groups theory was performed to align the model outcomes more closely with the numerical results, particularly in those scenarios where the two-groups theory exhibits limitations. Essentially, the code was fine-tuned by adding certain physical details derived from observations in numerical data. A resume of all modifications and tuned parameters is reported in table 3.2. Finally, since also $f_R^G E$ is included, the prompt redeposited fraction is calculated as shown in equation (3.31).

$$f_p = f_R^E + (1 - f_R^E) f_R^{GE} + 1 - \left[(1 - f_R^E) f_R^{GE}\right] f_R^G \tag{3.31}$$

Once surpassing the electric field, a particle's motion can still be influenced by it. For instance, a particle in the $1 - f_R^E$ fraction might undergo ionization in the sheath and decelerate. Additionally, due to gyromotion, particles may return inside the sheath. Therefore, even if in the absence of an electric field the trajectory does not cross the solid surface, there is still a probability to redeposit related to the electric field. The fraction f_R^{GE} is reported in equation (3.32). It is defined as the fraction of particles in

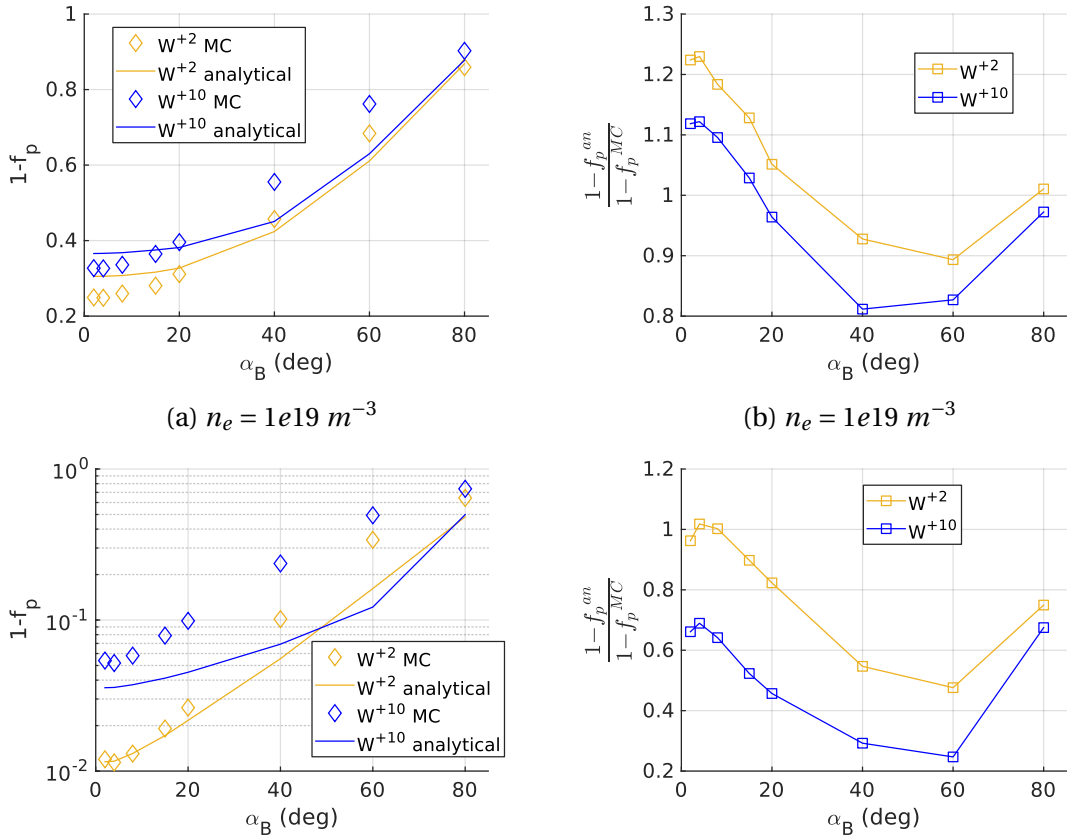

(a) $n_e = 1e19\ m^{-3}$

(b) $n_e = 1e19\ m^{-3}$

(c) $n_e = 1e20\ m^{-3}$

(d) $n_e = 1e20\ m^{-3}$

Figure 3.15: Ionic bombardment of W^{+2} and W^{+10} on W. A scan of $1 - f_p$ along the magnetic angle α_B is conducted using both Monte Carlo (MC) simulations and the analytical two-groups theory. The simulations are performed under fixed plasma conditions: $T_e = 20$ eV, $B = 3.7$ T, $n_e = 1e19\ \mathrm{m}^{-3}$, and $n_e = 1e20\ \mathrm{m}^{-3}$.

$1 - f_R^E$ having less energy than the potential drop at the averaged ionization distance ($|\phi(\overline{\lambda_z^*})|$).

$$f_R^{GE} = \int_0^{-\phi(\overline{\lambda_z^*})} SEAD(E)^{NE} dE \tag{3.32}$$

The deceleration is introduced in the sputtered energy of the $1 - f_R^E$ distribution by slightly modifying the threshold distance λ_z^* (as opposed to $\overline{\lambda_z^*}$ that does not change). After experimenting with various values manually, the decision was made to redefine the threshold distance as the point where the particle retains 35% of its initial kinetic energy, see equation (3.33). The sputtered energy distribution is then recalculated as done in equation (3.10). Thanks to this tuned definition of the threshold distance, the energy distribution of the $1 - f_R^E$ fraction is a good approximation of the NP energy

distribution even if most particles ionize within the sheath. The physical meaning of this tuning is the following: if a particle lose more than 65% of its initial energy because of electric deceleration in the sheath, its probability of escaping is negligible.

$$-\phi(\lambda_z^*) = 1.35E_z \tag{3.33}$$

Figure 3.16 depicts the energy distribution of the NE population both with and without tuning. The distribution deriving from the tuned model is in better agreement to the NP energy distribution from MC simulations. This suggests that the refined definition of λ_z^* partially reproduces the additional electric filtering.

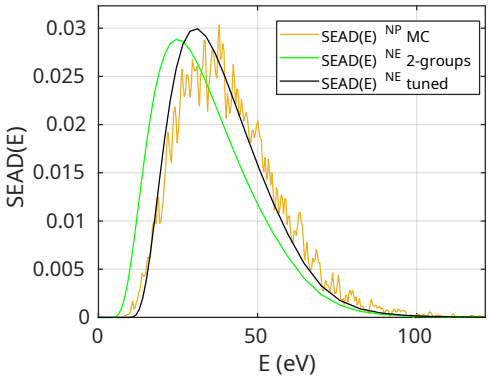

Figure 3.16: SEAD(E) of sputtered W caused by a flux of nitrogen ions (N^{+5}), estimated with Monte Carlo for the following conditions: $n_e = 2e20\ m^{-3}$, $T_e = T_i = 20\ (eV)$, $B = 3.7\ T$, and $\alpha_B = 4\ deg$. Comparison between two-groups theory and tuned SEAD with equation (3.33).

The energy distribution can be utilized to get the temperature $T_s = 2/3\overline{E}_{NE}$ of the $1 - f_R^E$ fraction. If no further energetic filter is present T_s is approximately equal to the temperature of the non-prompt population, thus it can be used to represent the temperature of the impurity source. Figure 3.17 illustrates the temperature estimates of T_s based on the two-groups theory, the tuned case, and Monte Carlo as function of the magnetic incidence angle α_B. The tuned model is in better agreement with MC results. Anyway, when the ionization mean free path is smallest ($n_e = 1e21\ m^{-3}$ case) the temperature is underestimated compared to the MC estimation suggesting that for such conditions even the tuned model does not well grasping the additional deceleration and thus filtering of low energy sputtered ions. Probably, this is because the fraction f_R^{GE} becomes non negligible and its description should be improved.

Another modification made to more accurately account for the energy dependence of the parameter p involves the probability of redeposition associated with particles reentering the electric field during their motion. This probability is calculated using the average ionization length along the z-axis of the sputtered population at the wall ($\overline{\lambda_z}$) and the corresponding average Larmor radius (ρ_L) of the first ionization, as expressed in equation (3.34).

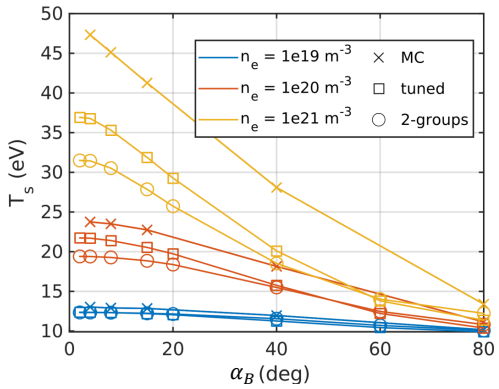

Figure 3.17: Temperature of non-promptly redeposited W sputtered by a flux of Nitrogen ions (N^{+5}) for three different electron densities at the sheath entrance and varying α_B. The other parameters were fixed as follows: $T_e = T_i = 20\ (eV)$, $B = 3.7\ (T)$.

$$p = \frac{\overline{\lambda_z Z}}{\overline{\rho_L}(cos(\alpha_B)) + a) f(\alpha_B)} \tag{3.34}$$

$$f(\alpha_B) = \frac{4}{3\pi}\alpha_B^2 - \frac{8}{3\pi}\alpha_B + 0.9 \tag{3.35}$$

Where $f(\alpha_B)$ in equation 3.35 is a second order polynomial added to compensate the error observed in figures 3.15b and 3.15d for the two-groups model. The polynomial could also be directly applied to equation (3.27) in the two-groups theory. The distance a is introduced to mimic the redeposition probability related to those particles that will not reach the wall but yet they return into the sheath electric field because of their gyromotion. A particle is considered reposited if, during its pure gyromotion, it re-enters the sheath at a distance a where the electrostatic potential matches or exceeds its own energy level. For a population of particles the value of the distance a is determined by inverting equation (3.36).

$$-\phi(a) \equiv \overline{E_{NE}} + \phi(\lambda_z^*) \tag{3.36}$$

$\overline{E_{NE}}$ is the average energy of the $1 - f_R^E$ fraction, see equation (3.18). Introducing a is equal to assuming that for the fraction $1 - f_E$ the wall is closer. This proximity depends on the average energy of the $1 - f_R^E$ fraction ($\overline{E_{NE}}$) and the ionization distance λ_z^*. If $\overline{E_{NE}} > -\phi(0)$ than $a = 0$ and no redeposition related to this phenomenon is included. Similarly to the previous section 3.2.4 results of the tuned model are compared to Monte Carlo numerical results and are shown in figures 3.18 and 3.19. Despite the tuning, still the code does not precisely reproduce Monte Carlo assessments of $1 - f_p$ when $\hat{\lambda} \lessapprox 0.1$ overestimating $1 - f_p$ as $\hat{\lambda}$ decreases, see figures 3.18a and 3.18b. Anyway, the spreading of the difference is reduced with respect to the two-groups model, see figure 3.13. Furthermore $1 - f_p$ is more sensitive to the impact energy of incident ions

showing a larger ramification for smaller $\hat{\lambda}$.

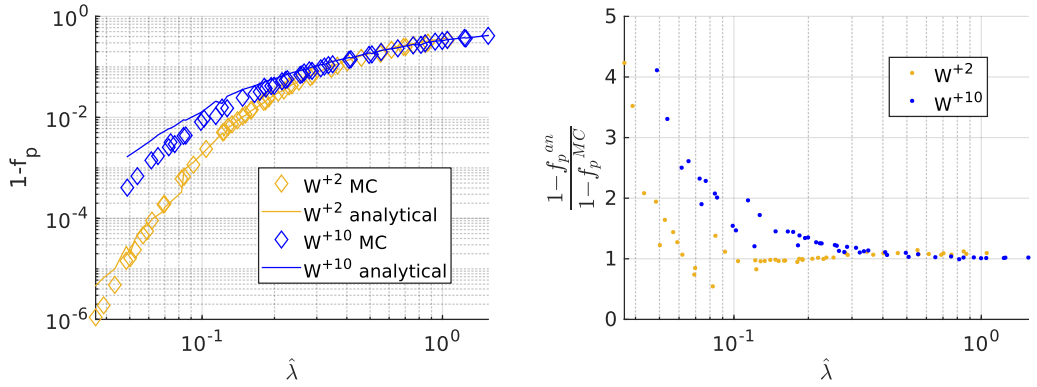

(a) (b)

Figure 3.18: Ionic bombardment of W^{+2} and W^{+10} on W at a fixed magnetic angle $\alpha_B = 4\ deg$. The other parameters varied, $n_e \in [5e18, 5e20]$ m^{-3}, $T_e \in [15, 30]$ eV and $B \in [2, 5]\,T$.

Testing with respect to the magnetic angle of incidence are improved mainly thanks to the polynomial in equation (3.35). However, the error remains significant (approximately 40%) for larger values of α_B when dealing with highly charged ions and elevated electron densities, as depicted in figure 3.19d. This suggests that another corrective function $f(\alpha_B)$ more suitable should be used.

3.2.5.1 Fluid parallel velocity

To characterize a fluid source it is necessary to estimate also the mean parallel velocity of the sputtered distribution. As energy, this is another quantity that do conserves even after ionization, in a collisionless plasma. Hence, the average parallel velocity $\overline{v_\parallel}$ can be calculated if the SEAD^{NP} of neutrals associate to the $1 - f_p$ fraction is known, as illustrated in equation (3.37).

$$\overline{v_\parallel} = \int SEAD^{NP}(E,\theta,\phi)\, v_\parallel(E,\theta,\phi)\, dE d\theta d\phi \tag{3.37}$$

Unfortunately, the sputtered angular distribution (SEAD^{NE}) reported in equation (3.10) associated to the fraction $1 - f_R^E$ do not well represents the angular distribution (SEAD^{NP}) of the neutrals non-promptly redepositing, see figure 3.7d. Indeed, the fraction $1 - f_R^E$ captures only the energetic redeposition, while redeposition is also related to other phenomenon, such as gyromotion, depending on the angle. Strictly speaking assuming SEAD$^{NP} \approx$ SEAD^{NE} is not correct. The parallel velocity is thus fine-tuned as shown in equation (3.38). Essentially the initial average parallel velocity of the sputtered species is divided by an exponential function of the angle α_B. The exponential function $1 + 1.6exp(-\alpha_B/15)$ fits the ratio $\overline{v_\parallel}^{NE}$ of the NE fraction to $\overline{v_\parallel}^{NP}$ of the NP fraction. From a first preliminary comparison with Monte Carlo results the

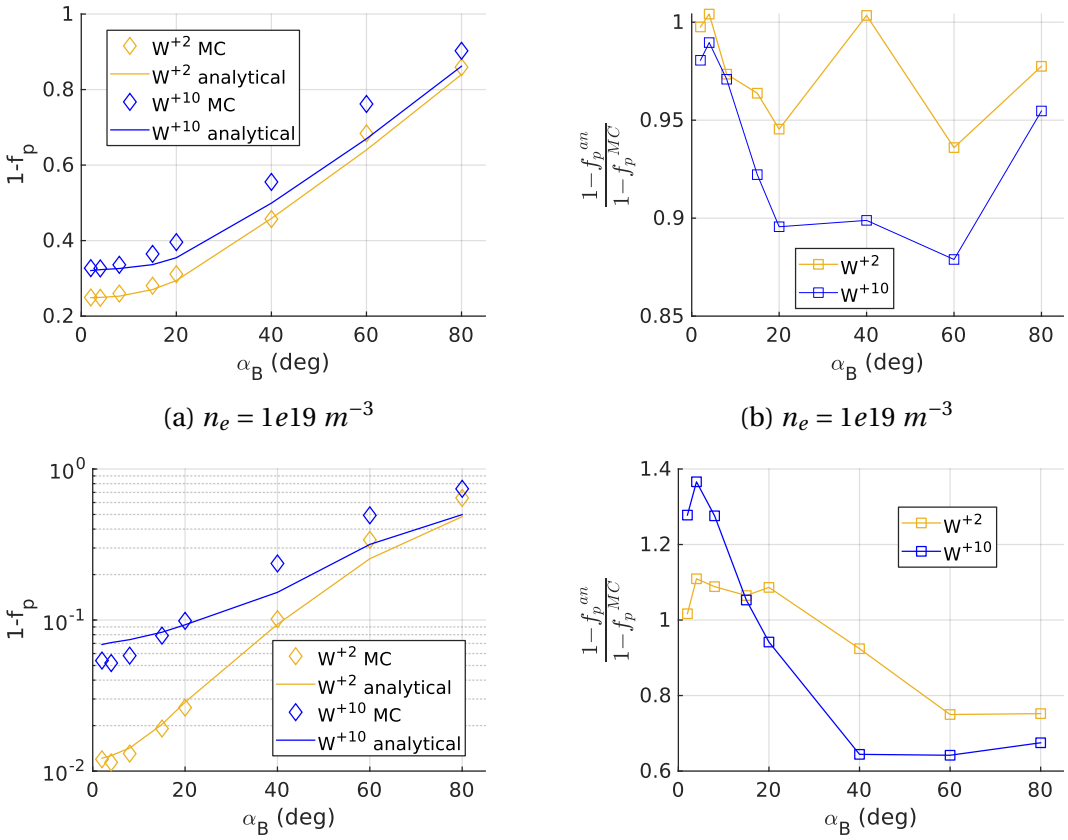

(a) $n_e = 1e19\ m^{-3}$

(b) $n_e = 1e19\ m^{-3}$

(c) $n_e = 1e20\ m^{-3}$

(d) $n_e = 1e20\ m^{-3}$

Figure 3.19: Ionic bombardment of W^{+2} and W^{+10} on W. A scan of $1 - f_p$ along the magnetic angle α_B is conducted using both Monte Carlo (MC) simulations and the analytical two-groups theory. The simulations are performed under fixed plasma conditions: $T_e = 20$ eV, $B = 3.7$ T, $n_e = 1e19\ \mathrm{m}^{-3}$, and $n_e = 1e20\ \mathrm{m}^{-3}$.

tuned estimation seems to hold even for a fairly large window of electron densities, see figure 3.20.

$$\overline{v_\parallel} \approx \int SEAD^{NE}(E,\theta,\phi)\, v_\parallel(E,\theta,\phi)\, dE d\theta d\phi \Big/ \big(1 + 1.6exp(-\alpha_B/15)\big); \tag{3.38}$$

Where α_B is in degrees.

All the modifications and tuning parameters added in the three groups theory are resumed in table 3.2.

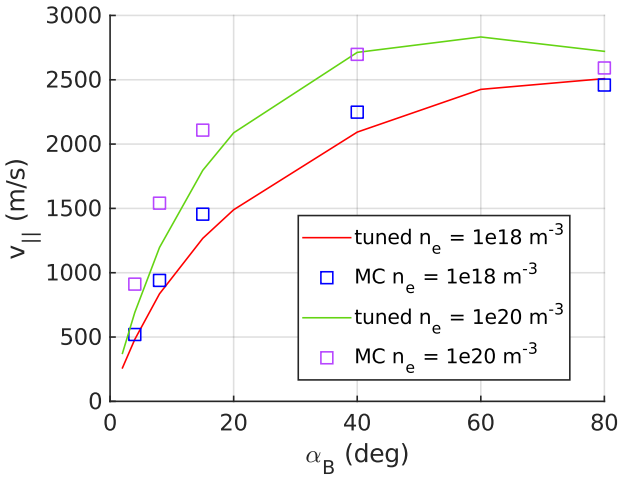

Figure 3.20: The average parallel velocity of sputtered W due to a flux of incident nitrogen ions (N^{+5}) is examined across a range of magnetic angles α_B. The results from both Monte Carlo (MC) simulations and the tuned version of the two-groups model (equation (3.38)) are compared under two different electron densities at the sheath entrance: $n_e = 1e19\ m^{-3}$, and $n_e = 1e20\ m^{-3}$, in the following conditions: $B = 3.7\ T$, $T_e = 20\ eV$.

two-groups	**tuned**
$-\phi(\lambda_z^*) = Ecos(\theta)^2$	$-\phi(\lambda_z^*) = 1.35Ecos(\theta)^2$
$p = \frac{\omega_L \overline{Z}}{\omega_{ion}^{SE}(cos(\alpha_B))}$	$p = \frac{\overline{\lambda_z} \overline{Z}}{\overline{\rho_L}(cos(\alpha_B))+a) f(\alpha_B)}$
$f_R^{GE} = 0$	$f_R^{GE} = \int_0^{-\phi(\overline{\lambda_z^*})} SEAD(E)^{NE} dE$
$\overline{v_\parallel} = \overline{v_\parallel}^{NE}$	$\overline{v_\parallel} = \overline{v_\parallel}^{NE} / (1 + 1.6exp(-\alpha_B/5))$

Table 3.2: Recap of all tuning parameters highlighted in red.

3.3 Prompt self sputtering

The fraction of redeposited particles f_p may erode again the surface at the same position increasing the net flux. Erosion by any projectile particle species (p) impinging over a target species (t) is followed by prompt self sputtering. Essentially the target material will erode itself because of prompt redeposition. Each prompt self sputtering event is followed by another one, thus a fading cascade of self sputtering is initiated when a projectile erodes a material. We will refer to each step of the cascade with an order, the order zero being the absence of prompt self sputtering. In the zero

order approximation prompt self sputtering is neglected and the eroded net flux is approximated as the gross flux provoked by the projectile p on target t ($\Gamma^{p\to t}_{gross}$), times the fraction of non prompt redeposited particles ($f_{np_0} = 1 - f_{p0}$), where subscript 0 indicates that these are the values associated with order 0 of the series, see first term on the RHS of equation (3.39). Continuing the sequence of events, the first order involves the occurrence of the first self sputtering event. When no collisions are present, the incident particle flux responsible for self sputtering equals the redeposited flux from the prior step, the prompt-self incident flux from the zero order is equal to $\Gamma^{p\to k}_{gross}(1-f_{np_0})$. Similarly, the gross self sputtering in the first order is equal to the self incident flux multiplied by the first order effective self sputtering yield, denoted as $\overline{Y_{1_{t\to t}}}$. As usual, also in the first order, the net flux is given by the gross flux times the associated non prompt redeposition fraction f_{np_1}. In general, the net flux of a generic number of orders N_o can be written as in equation (3.39).

$$\Gamma_{net} = \Gamma^{p\to t}_{gross}\left(f_{np_0} + \sum_{j=1}^{N_o}\left(\prod_{k=1}^{j}\overline{Y_{k_{t\to t}}}(1-f_{np_k})\right)f_{np_j}\right) \tag{3.39}$$

Starting from zero, the sequence can either converge or diverge going towards infinity. A simple example to understand whether the divergence will happen or not can be calculated assuming that f_{np} and $\overline{Y_{k_{t\to t}}}$ are constant along the whole series, thus are equal to their zero order counterpart. In such a scenario, the net flux can then be expressed as follows.

$$\Gamma_{net} = \Gamma^{p\to t}_{gross}\left(f_{np_0} + \sum_{j=1}^{N_o}\left(\overline{Y_{0_{t\to t}}}(1-f_{np_0})\right)^j f_{np_0}\right) \tag{3.40}$$

In this case, the ratio r between two consecutive orders is constant.

$$r = \overline{Y_{0_{t\to t}}}(1-f_{np_0}) \tag{3.41}$$

Since $1 - f_{np_0} \leq 1$, the ratio $r(f_{np_0}) < 1$ if and only if the prompt self sputtering yield is less than one ($\overline{Y_{0_{t\to t}}} < 1$). Of course, the presented framework is idealized because the parameters vary along the series. The energy source for prompt self sputtering are the electric field and collisions (which are neglected). The energy sink instead is the eroded material, where most of the incident energy is lost as heat. As further evidence, it is sufficient to consider that the energy of sputtered particles is always lower than the energy of incident particles. Therefore, if the prompt self sputtering energy source is constant, except made for the zero order where sputtering could be caused by a different species maybe accelerated in the SOL, f_{np} and $\overline{Y_{t\to t}}$ decrease for higher orders. For this reason, it can be inferred conservatively that if $\overline{Y_{0_{t\to t}}} < 1$ the series converges. In the analytical model, the average energy of promptly redeposited particles is approximated assuming energetically redeposited particle to be at their first ionization state, while the rest of redeposited particles ionization state is considered

equal to Z_{np} defined in section 3.2.2.1.

$$\overline{E_0} \approx \left(f_R^E + (1 - f_R^E) Z_{np}\right) \Delta\phi \tag{3.42}$$

The average angle of incidence is fixed equal to $\overline{\alpha} = 20\ deg$ which is in the range of incident angles calculated using Monte Carlo, see figure 3.22a where sputtering yield is lower than one.

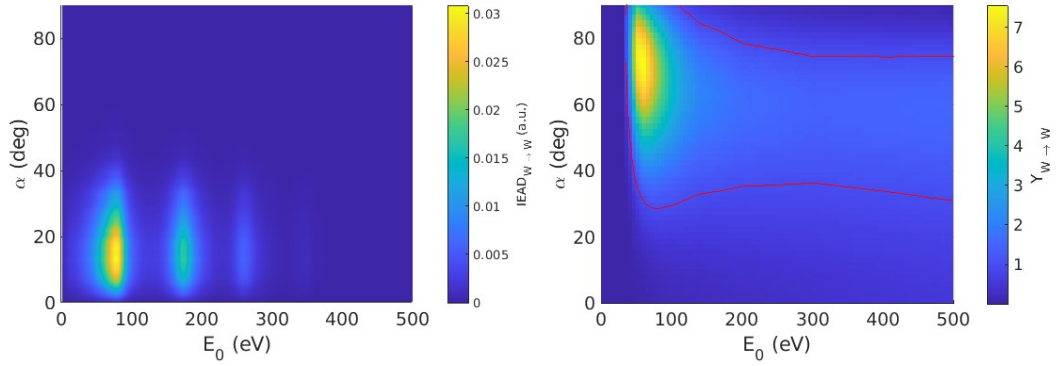

(a) IEAD prompt self

(b) Sputt. yield self

Figure 3.21: a) Example of $IEAD$ of W prompt self-sputtering calculated with MC (first order) . b) Sputtering yield of W self sputtering, contour line $Y_{W\to W} = 1$ in red [41]

The fluid approximation of prompt self-sputtering particles' incident energy distribution shown in equation (3.42) can underestimate f_{np} since a kinetic $IEAD$ would be more appropriate for such low charge states and low impinging energies, as discussed in section 2.5. Figure 3.21a shows the $IEAD$ of prompt redeposited W. The energy distribution shows the different charge states, while the angular distribution peaks at almost perpendicular angles. Contrarily to the sputtering cause by light impurities (see figure 1.2), the sputtering yield of W on W is more sensitive to the incidence angle α then the incidence energy, see figure 3.21b. For $E_0 \leq 500\ eV$ if $\alpha \lesssim 30\ deg$ the sputtering yield is below one and no divergent cascade effect can happen. It is possible though that the incidence angle is less grazing and in that case prompt redeposition could theoretically trigger an uncontrolled cascade event. Physically, for such events, the sputtering model breaks, so it is difficult to predict what happens when the self-sputtering series diverges. To check whether Monte Carlo simulations based on the model described in chapter 2 predict convergent series, a similar (only different α_B) set of plasma parameters as the one in table 2.1 was scanned with respect to an incident beam of Nitrogen at its fifth ionization charge state (N^{+5}). The beam was considered monoenergetic and with a fixed average angle of incidence $\overline{\alpha} = 40\ deg$. The magnetic angles simulated are $\alpha_B = 2, 4, 8, 15, 20, 40\ deg$. Since the prompt self sputtering IEAD is not known, it is calculated numerically with Monte Carlo tracking. In this case then, no probability of non redeposition P_{nr} was used and particles were directly tracked.

An example of prompt W on W IEAD is shown in figure 3.21a, each ionization state populates a distinct energy interval centered around $\Delta\phi Z \approx (3 - V_{bias}/T_e)ZT_e$ and the majority of particles redeposit in their first ionization state. Numerical results show that the electric field is predominant and the average impact angle is below the $Y_{W\rightarrow W} = 1$ threshold. Furthermore, the incidence angle of promptly redeposit W peaks around $\alpha = 20\ deg$ as well as the effective sputtering yield whose mode value is approximately 0.4, see figure 3.22. In the range of parameter scanned the first order correction is always less than 35% (see figure 3.23a), thus, according to equation (3.41) orders greater than the first one are indeed negligible. The Monte Carlo first-order correction exhibits a broad peak around $f_{np_0} \approx 0.3$, indicating that $f_{np_0} \gtrsim f_{np_1}$ as hypothesized in equation (3.40). This supports the idea that only a self-sputtering greater than one can trigger an uncontrolled cascade event. Moreover, the peak value of the first-order correction is close to the one where f_{np_0} and $\overline{Y_{0_{t\rightarrow t}}}$ are constant. In this case, the series peaks for $f_{np_0} = f_{np_1} = 0.5$, reaffirming the similarity between f_{np} from orders zero and one. It is envisaged that since prompt self-sputtering is dominated by the first ionization state, only negative bias and/or high temperatures $(3 - V_{bias}/T_e)T_e \sim 1e3\ eV$ at the PFC can trigger a cascade event. For instance, a temperature $T_e = 100\ eV$ requires $V_{bias} = -700\ eV$, on the other hand if $V_{bias} = 0$ the temperature should be on the orders of the keV. These conditions significantly exceed typical values in front of PFCs within tokamak reactors in the absence of Edge Localized Modes (ELMs). In the presence of ELMs, a cascade effect related to prompt redeposition could be theoretically possible if the model assumptions hold true even for such high temperatures.

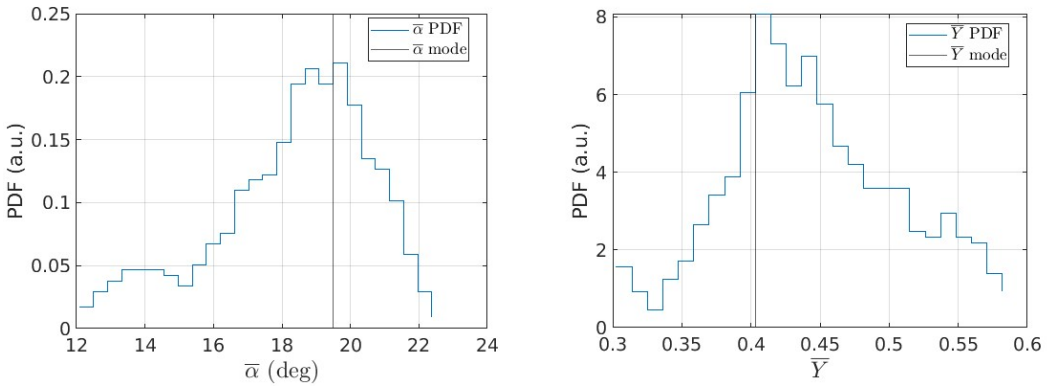

(a) (b)

Figure 3.22: prompt self-sputtering average angle of incidence (a) and effective gross sputtering yield $\overline{Y}$ (b)

The model presented in Section 3.2 is applied to the dataset mentioned here for the purpose of estimating f_{np_0} and the first order prompt self-sputtering contribution. This estimation is carried out by utilizing Equation (3.42) to determine the incident energy distribution of W particles promptly redeposited while the incidence angle is approximated with an average value $\overline{\alpha} = 20\ deg$ which is in agreement with Monte

Carlo output as previously mentioned. Results are shown in figure 3.23. MC and the analytical model f_{np} follow the same trend and have an agreement in the order ± 30 % suggesting that the analytical model could be also used to reproduce prompt self-sputtering.

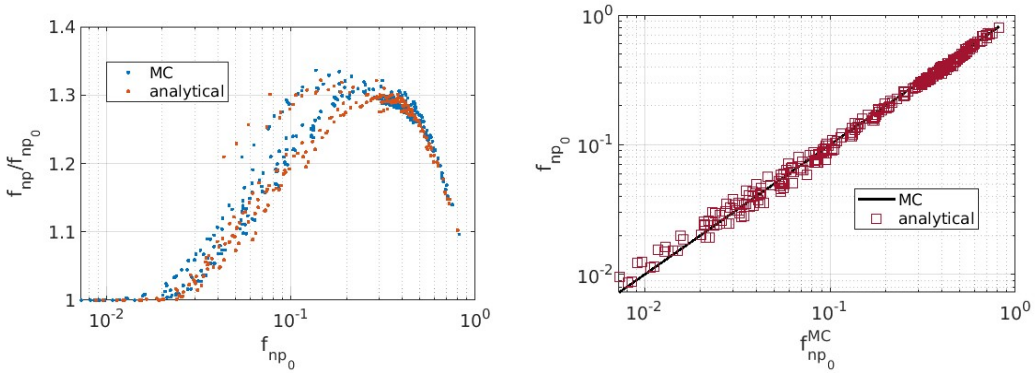

(a) (b)

Figure 3.23: First order prompt self-sputtering correction to both analytical and MC solutions (a). Comparison between MC and analytical model of f_{np_0} (b).

4 Experimental validation of the sheath model and application of the 3-groups model to the WEST database

Sommaire

4.1 Model validation of tungsten erosion and redeposition properties using biased tungsten samples on DiMES . . . 93
4.1.1 Introduction . . . 93
4.1.2 Materials and methods . . . 94
4.1.3 Numerical simulation . . . 96
4.1.3.1 ERO2.0 . . . 96
4.1.3.2 Plasma background . . . 97
4.1.4 Results . . . 98
4.1.4.1 Net erosion - RBS . . . 98
4.1.4.2 Gross erosion - UV . . . 99
4.1.5 Discussion . . . 100
4.2 Application of 3-groups model model for erosion and redeposition to the WEST database . . . 101
4.2.1 Post-processing of WEST C7 campaign . . . 101
4.2.2 Proxies of impurity ions at the WEST lower divertor . . . 103
4.2.2.1 Application of three groups model . . . 106

A portion of the thesis work was dedicated to the experimental verification of the assumptions beneath the reduced models discussed in chapters 2 and 3, followed by their application to experimental data from the tokamak WEST (section 4.2.2.1). The validation was conducted in the DIII-D National Fusion Facility hosted by General Atomics (GA) research laboratories in San Diego. The collaboration falls within the framework of the mobility projects offered annually by the INSTITUT SCIENCES DE LA FUSION ET DE L'INSTRUMENTATION EN ENVIRONNEMENTS NUCLÉAIRES (ISFIN) under the name of '2022 PhD Student Research International Mobility' (SRIM). The DIII-D tokamak was chosen because it features a divertor device called divertor material evaluation system (DiMES), designed for exposing small quantities of materials to plasma for the study of Plasma-Wall Interactions (PWI). The DIII-D research group brings extensive experience to DiMES, which stands as one of the most

thoroughly inspected components of the machine. It is observed from numerous diagnostics to facilitate both in-situ and post-mortem analyses at each discharge. Furthermore, the almost complete coverage of the machine in carbon enables the isolation of signals originating from the material under examination. All this makes the DIII-D tokamak an excellent environment for studying erosion and redeposition in great detail. An experiment was conducted using the DiMES system to expose W samples to the lower divertor of DIII-D. Experimental measures were then compared to ERO2.0 [22] numerical results.

4.1 Model validation of tungsten erosion and redeposition properties using biased tungsten samples on DiMES

The Monte Carlo model described in chapter 2 shares several approximations with the ERO code [87], against which it was benchmarked in section 2.3.2. A key point of similarity lies in the use of the same approximation for the electric potential drop in the sheath [59]. Thus, the validation of ERO2.0 indirectly supports the reduced models presented in this thesis. Another justification for employing ERO2.0 is that the reduced models of this thesis are not applicable to the experiment done in DIII-D due to the smaller characteristic length of the exposed material compared to the characteristic length of W redeposition. Redeposition is consequently non-uniform and a 1D approximation is impractical. Moreover, the reduced models do not account for material mixing, whereas carbon mixing is present in DIII-D. In such cases,a particle tracking code proves to be the most suitable solution. This section presents the validation of tungsten erosion and redeposition simulations performed with ERO2.0 [22], compared against experimental data. The majority of the information presented is taken from the article [105] whose subject was presented during the 19th International Conference on Plasma-Facing Materials and Components for Fusion Applications held in Bonn in 2023. The article has been adapted with additional details to integrate it with the broader context of the thesis.

4.1.1 Introduction

Future magnetic confinement fusion reactors might rely on high-Z metallic plasma-facing components (PFCs) such as tungsten (W), due to their low sputtering yield, high melting point, and low tritium retention [31]. Heavy impurities penetration inside the core causes unacceptable radiative losses. Understanding erosion and its modeling is necessary to design and operate high-Z PFCs. To date, numerical solvers use reduced models necessary to simulate erosion and transport of W without employing heavier simulations (e.g. particle in cell). It is important, however, to validate how well these models can describe the plasma wall interaction and whether there is any need to modify them. To this end, an experiment was performed on the DIII-D lower divertor

to validate reduced models embedded in ERO2.0 [22]. The main goal of this work was to experimentally assess the accuracy of current models in evaluating W net and gross erosion as a function of the applied DC voltage (or bias). In fact, for high-Z elements, net erosion is affected by the electric field inside the plasma sheath [75] which can be manipulated by biasing the target surface.

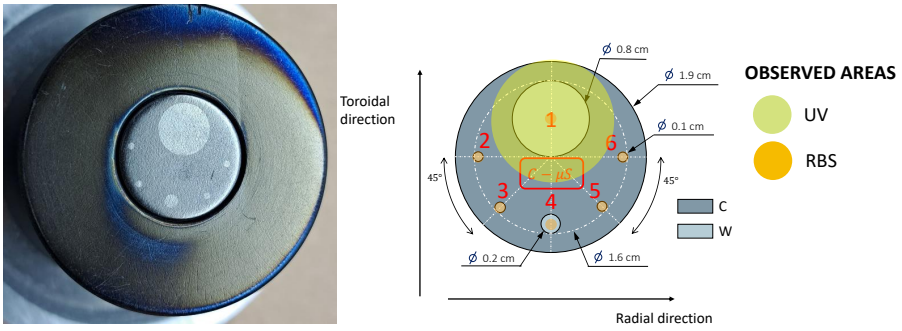

(a) Sample in DiMES (b) Sample design and viewing areas

Figure 4.1: DiMES setup top view (a) and viewing spots of the spectroscopy diagnostics employed(b). Also shown are pre and post-exposure RBS measurement locations.

4.1.2 Materials and methods

Five identical samples were inserted into the lower divertor of DIII-D via the Divertor Material Evaluation System (DiMES) [63], [106] as shown in figure 4.1a. Each sample was exposed to two discharges of an L-mode attached deuterium plasma and biased through a one-spear KEPCO power supply connected to the graphite samples with W coatings (the central part in figure 4.1a) electrically insulated from the grounded DiMES holder. After every two shots of exposure, the sample was exchanged and a different voltage was applied. Respectively 25 V, -60 V, 0 V, -40 V, and -20 V were applied, for a total of 10 shots. More precisely the experiment refers to shot numbers 192270 to 192280 of the DIII-D experimental campaign. Shot 192270 served as a sweep shot designed to characterize radial profiles of electron temperature and electron density while the remaining 10 regarded the actual experiment. For the sake of this work, the shot number enumeration goes from 70 to 80, corresponding to the DIII-D enumeration from 192270 to 192280 minus 192200. Biasing was quasi-DC, with regular voltage inversion pulses of 5 ms every 100 ms of constant bias at the nominal value to avoid arcing, as done in [107]. Electron temperature (T_e) and density (n_e) were maintained constant throughout the experiment (see figures 4.4a and 4.4b for T_e and n_e profiles). Temperature and density profiles were measured with a flushed Langmuir Probe (LP) positioned at a radial distance of 0.0177 meters relative to the DiMES center in the DIII-D lower divertor. The toroidal location of the LP is distinct from that of DiMES, so toroidal symmetry of plasma conditions is assumed. The electron density radially increase as a consequence of the reversed magnetic field

configuration. The reversed direction of drifts pushes particles radially outward, resulting in an increase in density. In addition, T_e and n_e were also checked via the Divertor Thomson Scattering (DTS) deployed in DIII-D [108]. Contrarily to LP, the DTS line of sight is directed towards the same toroidal position as DiMES. In figure 4.2c the DTS measurements from the line of sight corresponding to the same magnetic flux surface as the LP were compared to the LP measurements, demonstrating a good agreement. Furthermore, the LP and DTS demonstrated that for all shots T_e and n_e were well reproduced, figures 4.2b, 4.2a. The signal time traces were smoothed to reduce the spread related to plasma fluctuations in the SOL and I-V characteristic fitting errors, in order to make the figures more readable.

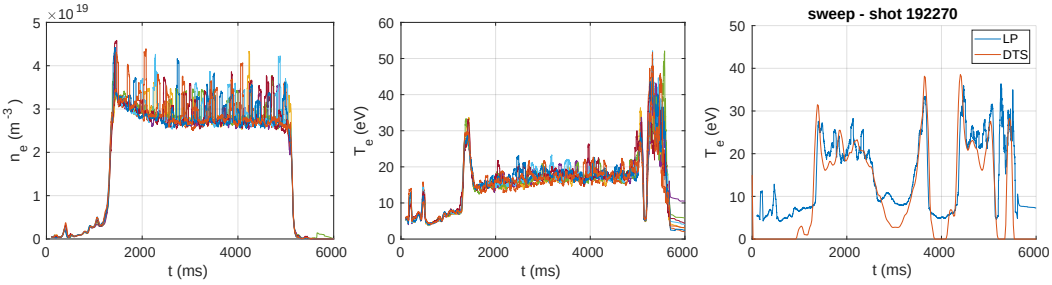

(a) (b) (c)

Figure 4.2: a) Smoothed LPs T_e time traces for shots s71 to s80. b) Smoothed LPs n_e time traces for shots s71 to s80. c) Smoothed LP vd DTS T_e signal during the sweep shot s70 (or 192270).

Biased samples consist of a carbon disk of about 0.75 cm in height and 1.9 cm top diameter (with a slightly larger bottom diameter to secure it in the holder) over which 6 W spots with thickness ranging between 21-27 nm were coated by magnetron sputtering at Sandia National Laboratories. W coatings were enumerated from 1 to 6, number 1 is large compared to the others with a diameter of 8 mm, number 4 is medium-sized being 2 mm in diameter, and the rest (2,3,5, and 6) are small with a diameter of 1 mm, see figures 4.1a and 4.1b. Carbon microspheres (labeled as C-μS in figure 4.1b) were manually placed on the carbon substrate to conduct experimental measurements of the incident ions' IAD. The findings from this measure are intended for future research and have not been presented here. Net erosion of the coatings was measured by comparing pre and post-exposure coating thickness via Rutherford Backscattering (RBS) and the gross erosion was estimated by applying the small/large spot technique [109]. Gross erosion was also measured in situ with the Auburn UV spectrometer (255.14 nm neutral W line), and the DiMES-TV (400.88 nm filter) which was excluded due to too low signal, see figure 4.3. Nevertheless, DiMES-TV imaging revealed that in both the DiMES outer case and the DiMES sample, there were leading edges exhibiting high plasma heat fluxes. This resulted in the carbon background radiation appearing as bright as the W radiation, even within the applied filter. Moreover, it could be that for the same reason the radiation emitted from small and medium W coatings positioned on the DiMES edge were brighter than the large

coating located in the center. Viewing areas of the UV and RBS are shown in figure 4.1b.

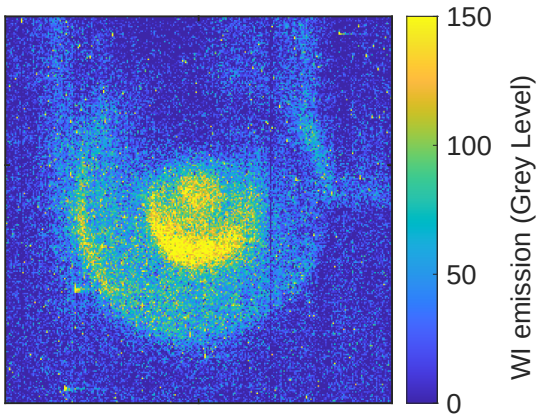

Figure 4.3: Greyscale representation of the DiMES-TV signal brightness at 400.88 nm for shot 192273.

4.1.3 Numerical simulation

4.1.3.1 ERO2.0

The Monte Carlo code ERO2.0 [22] was used to numerically estimate the net and gross erosion by tracking the sputtered species as a function of the applied bias. An average grazing impact angle of 80 deg with respect to the normal direction was fixed for the impacting species coming from the plasma, regardless of the bias. This was in line with experimental measures of D impact angle showing that the D Impact Angular Distribution (IAD) has a maximum between 79 and 86 deg [65]. Reflections of incident species over the targets were also considered. The Thompson distribution [81] was adopted for the sputtered particles' energy distribution and a cosinusoidal profile was applied for the angular component. Simulated particles were sampled from a realistic geometry representing the real design (figure 4.4) except made for the carbon substrate that instead of being circular is squared. Particle collisions, thermal forces, drifts, and anomalous diffusion were included. The anomalous diffusion coefficient was set to 1 m^2/s as reported in [49]. Redeposited particles could either reflect or implant into the target causing the mixing of C and W. Each W coating was simulated with a realistic thickness of 30 nm, in line with RBS pre-exposure measures mentioned in section 4.1.2. Reflection coefficients were taken from SDtrimSP databases present in ERO2.0. The surface temperature dynamic and the presence of oxides were not simulated. Finally, the domain was isolated by imposing an absorbing boundary condition, hence, particles reaching the simulation boundary were eliminated.

4.1.3.2 Plasma background

A local plasma background of 4 cm^3 over the samples was given as input to the code ERO2.0. Instead of solving it with fluid codes, it was manually designed through assumptions based on experimental data and plasma sheath theory. For instance, considering that the DiMES system in the lower divertor of DIII-D is subjected by a grazing and approximately uniform magnetic field angle $\alpha_B = atan(\frac{\sqrt{B_R^2+B_t^2}}{B_z}) \lesssim 2°$, the radial magnetic component was neglected ($B_t \gg B_R$ at the DiMES location), while B_t and B_z were considered uniform with $\alpha_B = 2°$. The plasma electron density and temperature radial profiles were taken from LP measurements ($n_{e,LPs}, T_{e,LPs}$) see figure 4.4, the uncertainty for LP measures is around 10%. The electron density variation along the perpendicular axis z was assumed to follow the Boltzmann factor: $n_e(R,\phi,z) = n_{e,LPs}(R)e^{-V(z)/T_e(R\phi,z)}$. Where $V(z)$ is the potential drop along z calculated by ERO2.0 using the fit formula proposed in [58].

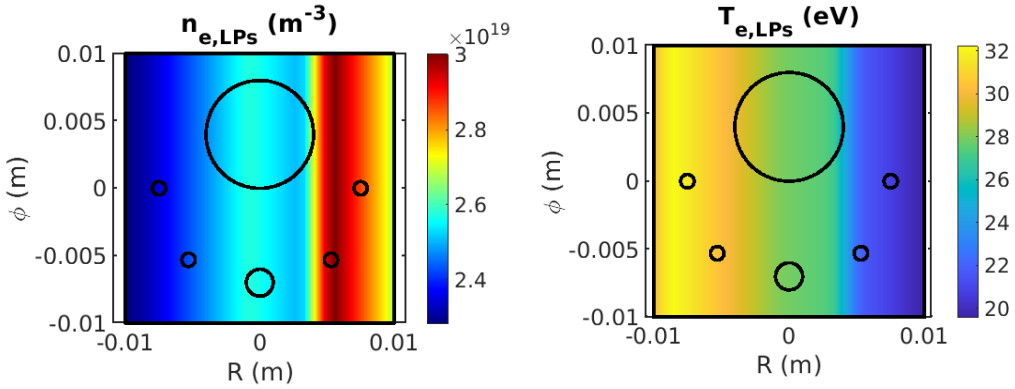

(a) (b)

Figure 4.4: Simulated target geometry within ERO2.0. LP measures of n_e at the sheath edge (a) and T_e (b) are here represented.

The temperature drop occurring inside the sheath is not considered, thus the electron temperature was considered uniform in the whole domain leading to $T_e(R,\phi,z) = T_{e,LPs}(R)$. Equipartition $T_i = T_{e,LPs}$ was imposed even inside the Debye sheath. Interestingly, at least for null or positive bias the whole plasma background can be quasi-neutral. Indeed, the Debye sheath formation is prevented if the angle α_B is smaller than the critical angle α_B^* [62]. However, in the range of bias explored the Debye sheath reappears already for $V_{applied} = -20\ V$ if equipartition is considered $T_i = T_e$ and $T_e \gtrsim 28$ eV, see equation 4.1 and figure 4.5. Lastly, Carbon was simulated as the only plasma impurity at 2 % concentration, and the Carbon population was approximated as 50 % C^{+2} and 50 % C^{+3} as suggested in previous works [110] for a similar experiment.

$$\alpha_B^* = sin^{-1}\left(\sqrt{2\pi\frac{m_e}{m_i}\left(1+\frac{T_i}{T_e}\right)}e^{\frac{V_{applied}}{T_e}}\right) \tag{4.1}$$

Where T_e and T_i are in eV, m_i is the main plasma ion mass, m_e is the electron mass, and $V_{applied}$ is the applied voltage.

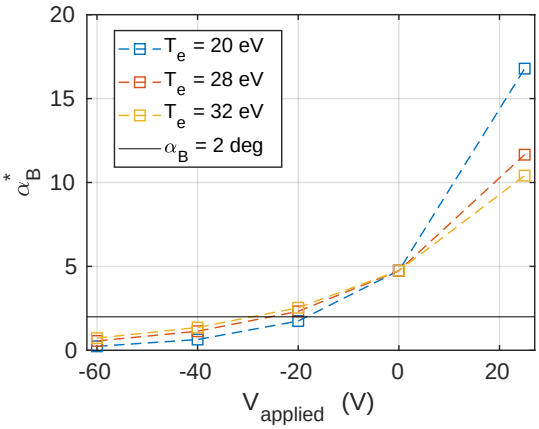

Figure 4.5: The critical angle α^*_B for 3 values of T_e if equipartition is considered.

4.1.4 Results

Varying the target surface potential influences the impinging ions' energy and angle of impact, and as a consequence, the sputtering yield. As shown in [82] and [107] the sputtering yield and the gross flux depend on the applied bias, increasing if the bias is negative and decreasing in the opposite case. In the range of bias applied in this work, the same dependence is expected for the net eroded flux. Indeed, the net flux of eroded particles from a finite surface $\Gamma_{net} \approx \Gamma_{gross} \times f_{non-redep}$ where $f_{non-redep}$, is the fraction of non-redeposited W. From [76] $f_{non-redep}$ is directly correlated with the ratio between the neutral W characteristic mean free path $\lambda_{ion} \propto V_{applied}$ and the sheath width λ_{sheath}, hence on the adimensional parameter $\hat{\lambda} = \lambda_{ion}/\lambda_{sheath}$. Anyway, since $\lambda_{sheath} \approx 1-2$ mm, is almost constant in the range of bias applied then also $f_{non-redep}$ and Γ_{net} are expected to be correlated to the bias. For lower biases (higher), $\hat{\lambda}$ increases (decreases) and so will Γ_{net}. Biasing influences also the reflection coefficients, as discussed

4.1.4.1 Net erosion - RBS

RBS was used to compare the thickness of all W coatings before and after the plasma exposure. The difference in thickness can be translated into a net erosion [111], which approximates the gross erosion if the W coating size is small (less than or comparable to the ionization mean free path of the sputtered W atoms) [109]. The net erosion was then converted into a net erosion rate by dividing it by the total exposure time (approximately 8 s). Results for small W coatings (No. 2,3,5 and 6) are directly correlated with respect to the applied bias, see figure 4.6b. Under positive biasing, data points overlap (2 with 3 and 5 with 6), making it challenging to distinguish them visually. Both experimental and numerical results show a radial asymmetry, where

the hotter inner side of the sample is more eroded than the outer one, see figure 4.4b. For both null and positive biasing, the ERO2.0 outcomes consistently underestimate erosion. It is worth noting that RBS accuracy diminishes as the cumulated erosion layers become smaller. Consequently, RBS can not measure the very small values of net erosion given by ERO2.0. Another point to consider is the possibility that data from coatings 2 to 6 may have been influenced by edge effects. This is because, as illustrated in figure 4.1a, coatings 2 to 6 were deposited closer to the edge gap between the biased sample and the unbiased DiMES support than originally intended in the design, as depicted in figure 4.1b. Finally, net erosion rates over the DiMES radial center where n_e and T_e are roughly constant (coatings 1 and 4), do not show a clear trend with respect to the applied bias even if the numerical outcomes are within the experimental uncertainties, see figure 4.6a. This might be attributed to insufficient statistical data, and additional experiments should be conducted to address this issue more comprehensively.

4.1.4.2 Gross erosion - UV

The gross flux from W coating No. 1 was measured with a UV spectrometer looking at the 255.14 nm line. Fluxes were converted into erosion rates assuming coatings W density to be 6.3×10^{22} cm^{-3} thus equal to the density of solid bulk W. Since two shots were performed for each bias, two different measures are reported when taken, figure 4.7a. UV gross erosion measurements are roughly one order of magnitude lower with respect to ERO2.0 results. Moreover, UV gross erosion rates are lower than the net erosion measured with RBS indicating that the associated S/XB, which was calculated with ColRadPy [95], could be underestimated. The ratios between the gross erosion rate of ERO2.0 and UV signal averaged over each couple of shots appear to be relatively constant (~ 5) with a slightly increasing trend for larger biases (more positive), across the inspected range. Interestingly, the UV time traces never reached a steady state showing a distinct pattern between the first and second shot at each bias. It seemed as if there was a different W erosion dynamic happening in the second shot compared to the first one. Langmuir Probes signal indicates that the pattern is repeated for each bias with fixed plasma conditions see figure 4.7b, this means that the samples were indeed identical. Furthermore, the count rate measured from the UV for the 255.14 nm neutral W line decreases over time during the first shot, while conversely, it increases during the second shot. A possible explanation would be the dynamic of carbon mixing and the erosion of oxydes that could have impacted the signal time evolution. It could also be that carbon microspheres enahnced mixing during the first shot. On the second shot, micro particles are not present anymore and the divertor come back to an erosive regime where C mixing is negligible, thus the increase in W signal. Currently, there is limited evidence supporting this theory and further research is needed. While a few couples of shots show a decrease in the C signal from the first to the second shot this alone is not enough to prove it.

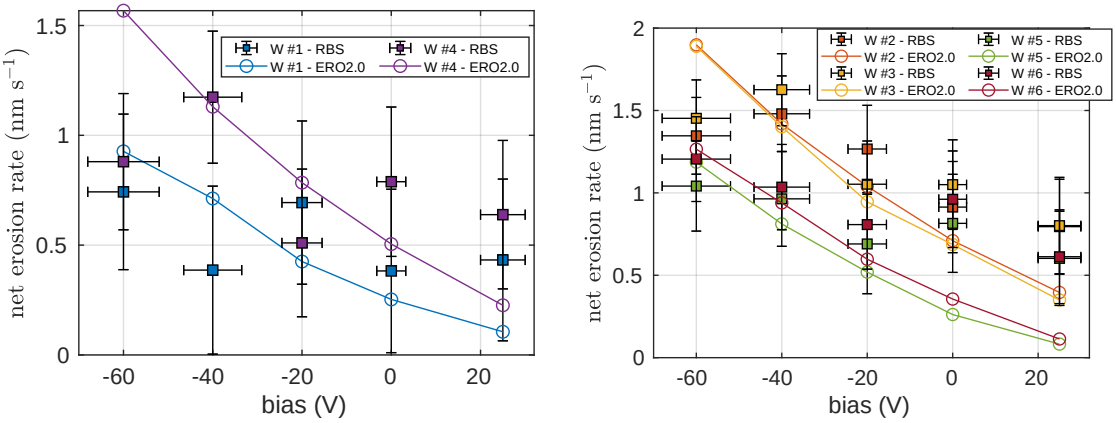

(a) RBS W coatings 1 and 4

(b) RBS W coatings 2,3,5 and 6

Figure 4.6: Resume of RBS experimental measures and simulation results

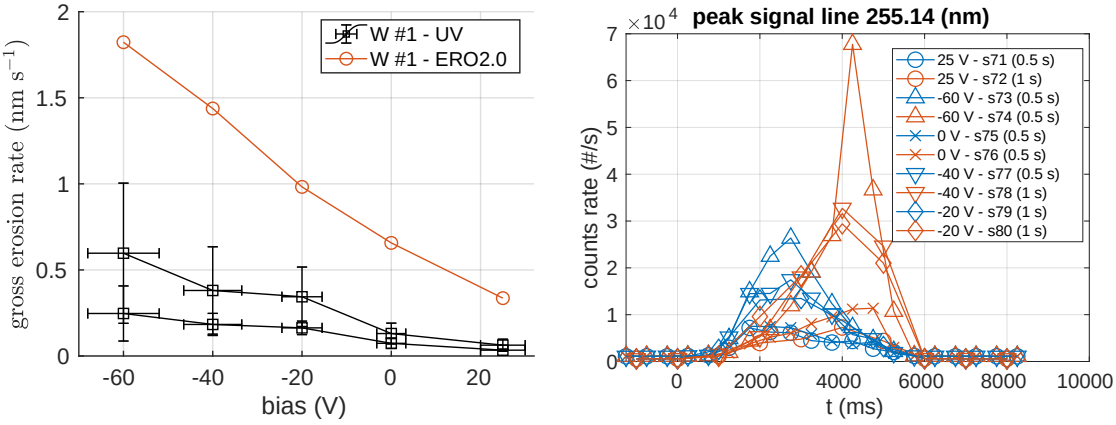

(a)

(b)

Figure 4.7: a) UV gross erosion compared to ERO2.0 results. b) UV count rate for the WI 255.14 nm line. The integration time is specified in the legend between parenthesis for each shot (e.g. 25V - s71(0.5 s) stands for shot No. 71, half a second of integration time and a bias of 25 V).

4.1.5 Discussion

An experiment was performed in the lower divertor of DIII-D to measure the effect of DC bias on the erosion of W targets of different sizes. The goal was to compare the experimental observations with numerical results reproduced with the ERO2.0 code. Erosion post-mortem RBS measurements of W coatings No. 2,3 5 and 6 were in agreement with ERO2.0 estimates both in trends and order of magnitude except made for the positive case. Contrarily, coatings No. 1 and 4 do not have a clear trend with respect to bias. These inconsistencies may be attributed to the limited cumulated erosion during the experiment, which can lead to less accurate RBS measurements, particularly under positive bias or for larger coatings where net erosion is minimal.

Moreover, it is suspected that an edge effect may be contaminating the measurements of coatings No. 2 to 6 since the targets were manufactured close to the boundary between the biased and unbiased sample regions. The edge effect was not included in ERO2.0 because only the biased surface was simulated. Gross erosion UV measurements are qualitatively in agreement with numerical results showing a nearly constant scaling factor of 5 when compared to the numerical findings. Finally, it can be concluded from the experiment that it is possible to qualitatively and quantitatively reproduce erosion as a function of bias at least for negative biases with ERO2.0. In the future, further studies should be performed to numerically reproduce the erosion of positively biased targets adopting longer exposure times.

4.2 Application of 3-groups model model for erosion and redeposition to the WEST database

The tungsten (W) Environment in Steady-state Tokamak WEST is a superconducting, actively cooled tokamak, hosted by the laboratory of IRFM (Institut de Recherche sur la Fusion par confinement Magnétique) as part of CEA's fundamental research division, in France [15], [112]. The tokamak is designed for extended operation, sustaining long pulses lasting up to 1000 s and it is one of the tokamak testing the tungsten monoblocks planned for ITER divertor. With the exception of boron nitride bumper limiters, all PFCs directly interacting with plasma are made out of tungsten.

Experimental measurements of electron density, temperature, incident magnetic angle and magnetic field intensity can be used as input parameters for the reduced analytical models presented in chapter 3. On the other hand, despite the existence of W density measurements in the core of WEST [113], the impurity concentration and composition in front of the PFCs is to date unknown. Photon fluxes coming from argon, carbon, boron, iron, nitrogen, oxygen, copper, and tungsten (just to mention a few) are frequently detected during pulses, thus a large number of possible impurity ions can provoke sputtering in WEST. To that end, a small sensitivity analyses is proposed hereafter regarding nitrogen and tungsten being used as proxies to represent light and heavy impurities present in the machine.

4.2.1 Post-processing of WEST C7 campaign

This section of the manuscript presents an application of the 3-group model to erosion data collected during the WEST experimental campaign called C7. In order to shrink the amount of data to be analyzed, a reduced database was produced by averaging every half-second of all signals. This approach is suitable only when the plasma remains stable within the half-second time step. However, there are instances, such as during the ramp up and ramp down, accidents, MHD instabilities, and disruptions, where plasma quantities vary too much, making averaged values inappropriate. To address irregular time steps, a criterion was applied: if the associated average value of the total radiated power deviates by more than 2 percent from its peak value within the time

interval, the data point is excluded. Furthermore, the database includes only spectroscopic measurements related to the lines of sight yielding the maximum brightness value around the lower divertor strike lines. Similarly, the electron temperature and density from LP are the maxima around strike lines. The peaks of brightness and LP measurements are typically spatially close, generally within a distance of less than 1 cm, as illustrated for one case in figure 4.8.

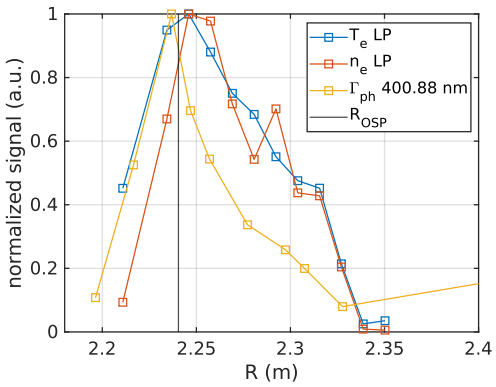

Figure 4.8: LP and visible spectroscopy (WI 400.88 nm line) radial profiles over the lower divertor OSP in WEST for shot #57453.

However, it should be noted that the automatic calculation and storage of the brightness peak position are not implemented. Therefore, the assumed spatial proximity may not always be accurate. An uncertainty study has not been conducted, and it is assumed that the dispersion within the dataset covers most uncertainties. In figure 4.9 are illustrated the frequency maps of maximum electron temperature and density for both outer and inner strike points (OSP and ISP) during the experimental campaign denoted as C7. It can be seen that the data collected by the LPs are grouped in two distinct areas of the diagram that are not connected to each other. The measurements represented are associated with stable plasma conditions. From the database, is observed that stability is achieved for two distinct divertor temperature ranges, a hotter one with T_e around 20 eV and a cooler one where T_e is around 3 eV. The stable conditions are classified as belonging to the hot divertor branch if $T_e \approx 20$ eV, equivalently if $T_e \approx 3$ eV, the plasma belongs to the cold divertor branch. In the C7 experimental campaign, approximately 80% of the stable points are situated within the hot divertor branch. Specifically, about 50% of all points fall within a narrow window of electron density in the hot divertor branch, ranging from 1×10^{19} to 3×10^{19} m^{-3}.

The analyses here shown concerns only the photon flux coming from the WI line at 400.88 nm. In section 4.2.2.1 an additional data filtering is implemented to eliminate photon flux measurements considered as outliers. Specifically, any photon flux measurements that deviate by more than three times the scaled Median Absolute Deviation (MAD) from the median are excluded from the dataset. This is the reason why less values of n_e and T_e are analysed compared to figure 4.9. Finally, photon fluxes are converted into gross erosion applying both the theoretical SXB coefficient

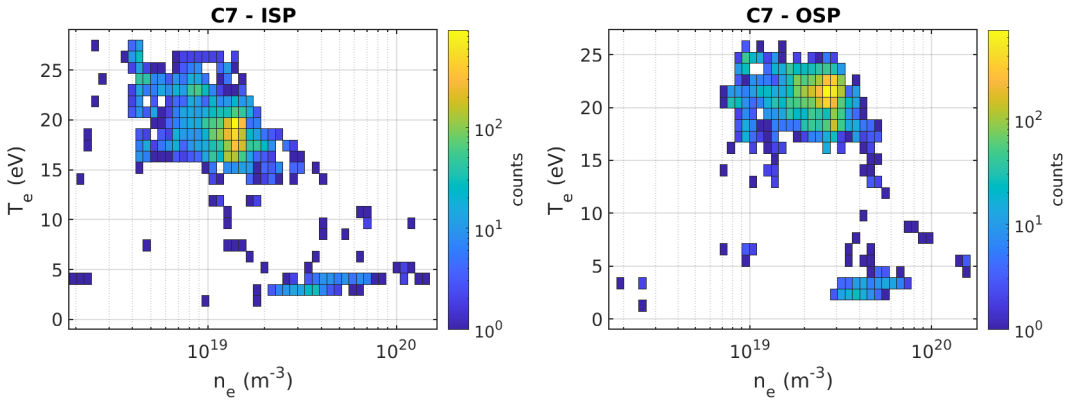

Figure 4.9: LP maximum values of electron temperature and density around the ISP and OSP of WEST lower divertor during the C7 campaign.

from ADAS [90] and the multimachine experimental fit proposed in [114].

4.2.2 Proxies of impurity ions at the WEST lower divertor

To apply the reduced models, it is necessary to know the mass and charge of the incident ions causing physical sputtering. To date, there are no direct measurements of the concentration and ionization state of the impurities near the tokamak walls. Undoubtedly, this is the biggest bottleneck in all erosion studies. In general, an equivalent or proxy species is used that theoretically averages out all impurities incident on the walls. The proxy species, ionization state, and equivalent concentration are educated guesses based on numerical simulations and/or inherent characteristics of the machine under investigation. At section 4.1.3.2 exactly the same thing was done, where the proxy species in DIII-D is carbon. In WEST, the species normally used as a proxy is oxygen [24, 25] since it is present due to microleaks related to the water cooling system. In this case, instead of using oxygen, a different approach based on experimental data is proposed.
As described in chapter 4.1.1, if convection is predominant and turbulence is averaged, the gross flux is equal to the incident flux multiplied by the effective sputtering yield (equations (1.27), (1.25) and (1.26)). An accurate calculation of the effective sputtering yield requires the Incident Energy and Angular Distribution (IEAD) of the impinging ion. In this case, the energy distribution is approximated using a gamma function for the parallel velocity and a Maxwellian distribution for the perpendicular component, as reported in section 2.2.1. Regarding the incident angular distribution, it is approximated as uniform and equal to the average incident angle $\overline{\alpha}$ calculated with a set of Monte Carlo simulations for a shallow incident magnetic angle $\alpha_B = 2$ deg, representative of WEST conditions at the lower divertor. For tungsten, nitrogen and deuterium the average angle is considered independent of the charge state and equal to 45,67 and 70 deg, respectively. The sputtering yield formula used is the fit proposed in [29, 41] which was tested against experimental data showing good

agreement both qualitatively and quantitatively [29]. The incidence magnetic angle α_B is assumed equal to the magnetic reconstruction calculated with the NICE code [115], while the magnetic field intensity is imposed equal to 3.7 T. Finally, the ion speed (c_s) at the sheath entrance is derived from the corresponding average energy at the sheath entrance from [60], imposing equipartition ($T_e = T_i$). The equation (4.2) depicts the numerical estimate of the gross flux of W resulting from the impact of a proxy species utilizing the approximations mentioned earlier. This calculation is based on the density and temperature values obtained from LP, while the equivalent concentration of the impinging species in front of the eroded surface is set equal to Cc_{eq}.

$$\Gamma_{gross}^{model} \approx Cc_{eq} n_e^{LP} c_s sin(\alpha_B^{NICE}) \overline{Y^{fit}}(\overline{\alpha}) \tag{4.2}$$

For a specific species and ionization state, the only unknown in equation (4.2) is the equivalent concentration Cc_{eq}. However, it may be feasible to estimate Cc_{eq} using experimental data. Indeed, since the gross flux measured experimentally via visible spectroscopy (denoted as Γ_{gross}^{exp}) should be similar to the numerical one (Γ_{gross}^{model}), then Cc_{eq} should be approximately equal to the measured gross flux divided by the numerical one calculated under the assumption of unitary concentration, i.e. $\Gamma_{gross}^{model}(Cc_{eq} = 1)$. Clearly, depending on the chosen ion the concentration value could be larger than one and oscillate in a nonphysical manner. In general, it is not enough to have one measurement to get the equivalent concentration and a statistical transformation of data has to be performed. The simplest approach, applied here, involves averaging the concentration over the entire campaign, as expressed in equation (4.3).

$$Cc_{eq} \approx \frac{1}{N} \sum_{i=1}^{N} \left(\frac{\Gamma_{gross}^{exp}}{\Gamma_{gross}^{model}(Cc_{eq} = 1)} \right)_i \tag{4.3}$$

The table 4.1 displays a list of ions examined as potential proxy impurities, along with their corresponding equivalent concentrations. This information is provided for both ADAS [90] and experimental inverse photon efficiencies [114]. Nitrogen was preferred over oxygen because the fitting parameter of the sputtering yield in [29] are not present for oxygen.

It is important to notice that the concentration of W are 5 to 10 times larger than the one (2e-4) measured in the core of WEST [113]. This may be related to the value of the impurity sound speed employed in equation (4.2). Despite the value of c_s applied includes the electric field acceleration in the SOL [60], it may still be underestimated. Indeed in [60] the acceleration of charged impurities is calculated in a collisionless and isothermal SOL. In reality, friction between highly charged W and plasma ions could accelerate particles up to Deuterium sound speed, thus the value of Cc_{eq} could be lower. For completeness, table 4.2 reports the values of equivalent concentrations calculated imposing $c_s = \sqrt{2T_e/m_D}$ where m_D is the Deuterium mass.

All combinations shown in the first two columns of tables 4.1 and 4.2 reproduce similar gross fluxes, the main difference resides in the Sputtered Energy and Angular distribution (SEAD) of the sputtered neutral particles they erode, which is funda-

proxy ion	Cc_{eq} (ADAS S/XB)	Cc_{eq} (exp. S/XB)
N^{+2}	3.3e-2	2.1e-2
N^{+5}	4.9e-3	3.2e-3
N^{+7}	2.9e-3	2e-3
W^{+5}	6.2e-3	4e-3
W^{+10}	2.4e-3	1.5e-3
W^{+14}	1.5e-3	9.8e-4

Table 4.1: Equivalent concentration of impurities at WEST lower divertor (OSP), for different ionization states of nitrogen and tungsten using both theoretical (ADAS) [90] and experimental (exp.) [114] inverse photon efficiencies.

mental to estimate the net flux. It is important to note that the three-groups model is founded on the SEAD model outlined in Chapter 2. This model incorporates a Thompson-like energy dependence (see equation 2.6), a cosinusoidal poloidal distribution, and a uniform azimuthal distribution. Notably, this SEAD is independent of the magnetic incidence angle α_B and the angular distribution of impinging ions, depending solely on the impinging ion's energy distribution. Figure 4.10 depicts the comparison between the experimental Γ^{exp}_{gross} at the OSP converted using ADAS inverse photon efficiencies, and the numerical gross flux estimate Γ^{model}_{gross} calculated using the two proxies N^{+7} and W^{+14} with equivalent concentrations $Cc_{eq} = 2.9e-3$ and $Cc_{eq} = 1.5e-3$, respectively. Both species reproduce the gross flux similarly when the electron temperature $T_e > 10$ eV, which correspond roughly to the hot divertor branch. Conversely, in the cold divertor branch approximated as $T_e \leq 10$ eV, nitrogen sputtering becomes small because its energy is too low. It is important to acknowledge that a portion of the spectroscopy measurements in the cold divertor branch involved nitrogen seeding shots. Consequently, the equivalent concentration is likely higher than $Cc_{eq} = 2.9e-3$ at some of the points represented in blue in Figure 4.10a. Nevertheless, the substantial difference between the experimental and numerical data is significant enough to suggest that if the impact of charge exchange neutrals is negligible, then the sputtering of the lower divertor in WEST is likely attributed to heavy, highly charged ions such as tungsten. However, it is observed that in the hot divertor branch all light impurities tested (see table 4.1) reproduce similar gross erosion fluxes.

It is important to emphasize that the results presented so far, based on the WEST database, are confined to the Lower Divertor OSP. Due to practical and technical constraints, the analysis has not been extended to other PFCs. Therefore, it is advised to not utilize divertor proxies for the rest of the machine.

proxy ion	Cc_{eq} (ADAS S/XB)	Cc_{eq} (exp. S/XB)
N^{+2}	1.4e-2	8.8e-3
N^{+5}	3.1e-3	2e-3
N^{+7}	2.1e-3	1.4e-3
W^{+5}	8.7e-4	5.6e-4
W^{+10}	4.8e-4	3.1e-4
W^{+14}	3.7e-4	2.4e-4

Table 4.2: Equivalent concentration of impurities at WEST lower divertor (OSP) for different ionization states of nitrogen and tungsten. Impurities are assumed to reach the OSP at the Deuterium sound speed. Both theoretical (ADAS) [90] and experimental (exp.) [114] inverse photon efficiencies are employed.

4.2.2.1 Application of three groups model

In the previous section, a method was presented to identify the proxy species that best represent the gross flow with respect to experimental data. Such method estimate that the most accurate proxy species for the OSP of the lower divertor is W^{+14}. Therefore, it is now possible to go a step further and calculate the net erosion and other relevant data related to tungsten sources using the three-group model described in 3.2.5. In the model, it is simulated a pure deuterium plasma polluted with a concentration Cc_{eq} (see table 4.1) of W^{+14} as eroding species. For simplicity, erosion related to prompt-self sputtering of W is neglected, although its contribution spikes (about 30% more erosion) approximately in the most common conditions of temperature, density and magnetic field angle, at the lower divertor of WEST, see section 3.3. In figures 4.11, the net flux is shown, which is approximated as the product of the gross flux from equation (4.2), multiplied by the fraction of particles not promptly redeposited $(1-f_p)$. It can be observed that the net flux is approximately equivalent to the gross flux for $\Gamma_{gross} \lesssim 10^{18}$ ($m^{-2}\ s^{-1}$). Such low gross flux values correspond to plasma shots belonging to the cold divertor branch, whose temperature $T_e \leq 3$ eV. The frequency of first ionization for such cold plasmas is very low, so the particles ionize far away from the eroded surface and their probability of promptly redepositing is small. Additionally, it is worth noting that the net flux, except for sporadic fluctuations, is directly proportional to the gross flux. Consequently, in the absence of direct experimental measurements of the net flux, one can assess the trend of net sources by examining the gross flux. Therefore, if the gross flux increases at the OSP of the lower divertor, the net flux will also grow.

The observed proportionality is not guaranteed. In reality, the net flux trend could reverse. This is demonstrated in figure 4.12, where eroded W net flux trends are shown for a fixed electron temperature and varying electron density. The net flux trend

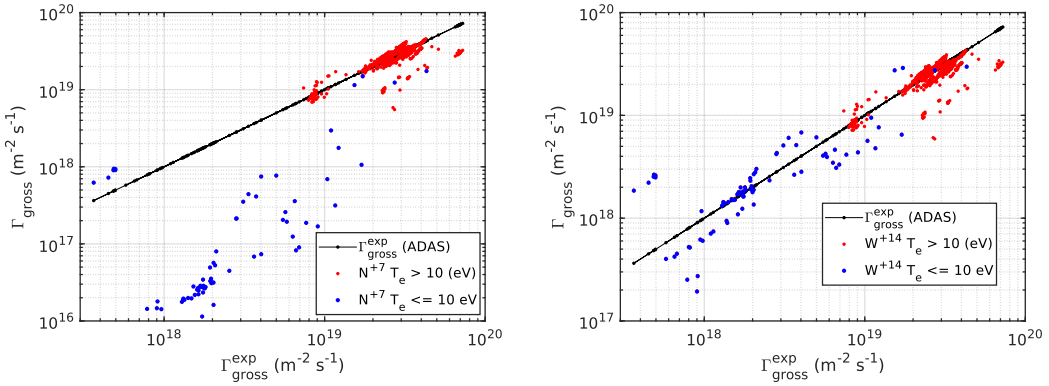

(a) (b)

Figure 4.10: Comparison between numerical estimates of the gross flux and experimental data for the OSP in the lower divertor of WEST. On the y-axis are plotted all kinds of Γ_{gross} both numerical and experimental. On the x-axis only experimental values of gross erosion are used. a) Proxy light impurity ion N^{+7}, b) Proxy heavy impurity ion W^{+14}. In blue(red) points relative to the cold(hot) branch.

reverse for different impinging ions, and an inflection point is identified beyond which the net flux decreases, even as the gross flux continues to rise. The position of this inflection point shifts towards higher density when the energy transferred from the incident particles to the eroded tungsten increases, thus the trend reversal is shifted toward higher densities for high charged ions impinging on the material.

In figure 4.12, only one eroded flux is shown because for the corresponding quantities ($B = 3.7$ T, $\alpha_B = 2$ deg and $T_e = 20$ eV), gross fluxes are approximately equal for all proxies used. Additionally, it is interesting to note that the fraction not promptly redeposited $(1 - f_p)$ depends strongly on electron temperature rather than density, see figure 4.13a. Furthermore, in figure 4.13b it can be observed that $\hat{\lambda}$ associated with W neutrals sputtered by a W^{+14} flux is greater than 0.4. So, as shown in figure 3.18b the 3-groups model faithfully represents the numerical results of Monte Carlo simulations. Since the range of values for $\hat{\lambda}$ at the OSP is already within the good-functioning zone of the 3-groups model, and the rest of the plasma edge is in similar if not lower density and temperature conditions, (i.e. $\hat{\lambda}$ even higher) it can be inferred that the 3-groups model could in theory be extended to the whole machine. So such a code is in general suitable for solving the net flow in WEST.

Other quantities of interest that the 3-group model reproduces regarding the net flux are illustrated in figure 4.14. These are the source temperature T_s, the average charge state $\overline{Z}$, and the average velocity parallel to the magnetic field and directed toward the plasma interior $v_\parallel$. Each of these has distinct behaviour between the hot divertor branch and the cold divertor branch. For example, the temperature T_s is almost always greater than the electron temperature in the cold divertor branch, while in the hot divertor branch there is $T_s \approx T_e$. Similarly, the average charge of tungsten

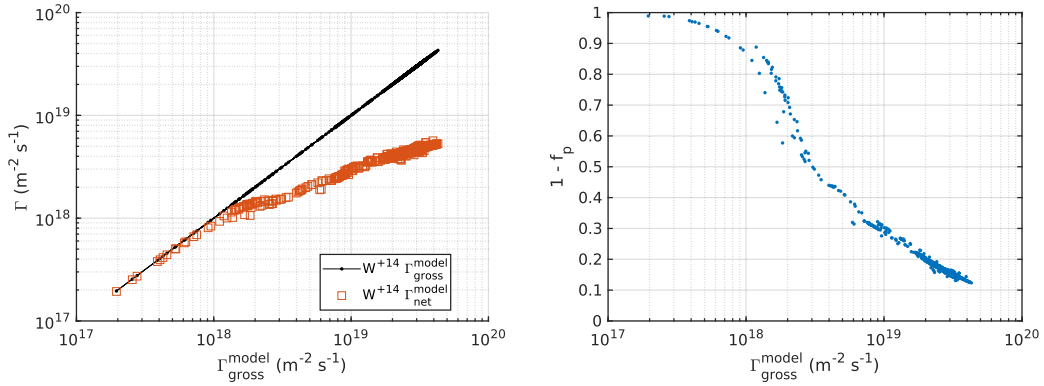

(a) (b)

Figure 4.11: a) Gross and net flux of sputtered W at the OSP, modeled with $Cc_{eq} = 1.5e-3$ and W^{+14} as impurity proxy. b) ratio of net over gross flux, for the same case.

is between 3 and 4 in the hot divertor branch, while it ranges from 1 to 3 in the cold divertor branch. Correctly assessing the average charge of W sources is vital in fluid codes to well represent collisions which depend on the square of the impurity charge. On the other hand, the parallel velocity turns out to be always negligible compared with the thermal velocity of Deuterium because of the very grazing incidence of the magnetic field at the WEST OSP where $\alpha_B \approx 2$ deg. A similar result is also shown in figure 3.20.

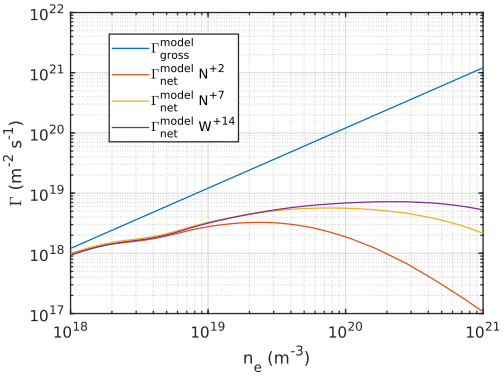

Figure 4.12: Gross and net flux of sputtered W modeled in the following conditions: $B = 3.7$ T, $\alpha_B = 2$ deg, $T_e = 20$ eV. Three impurity proxy are tested: N^{+2},N^{+7} and W^{+14} with equivalent concentration values Cc_{eq} (ADAS S/XB), taken from table 4.1.

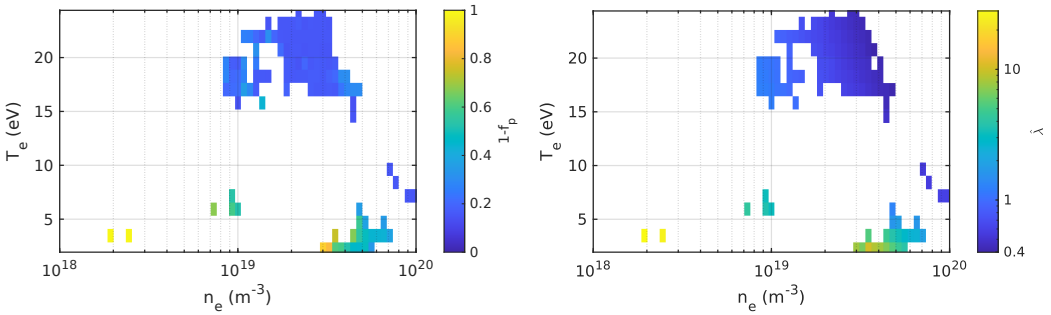

(a) (b)

Figure 4.13: W non-promptly redeposited fraction $(1 - f_p)$ and normalized ionization length $(\hat{\lambda})$ as function of electron density and temperature at the OSP of WEST lower divertor according to the three groups model.

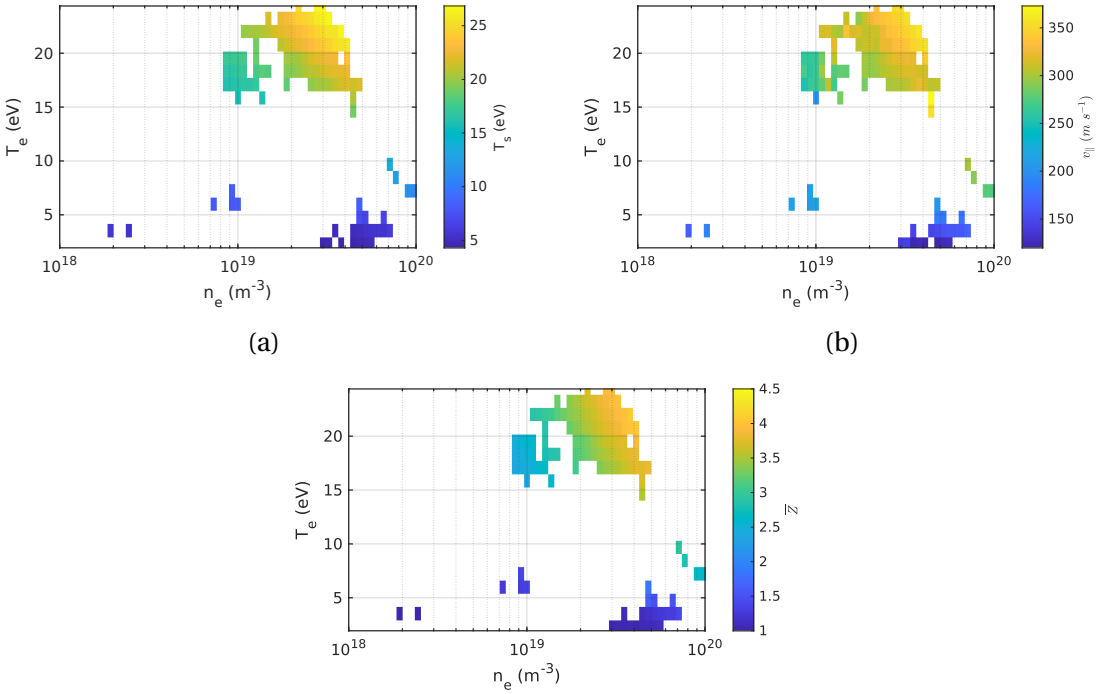

Figure 4.14: W source temperature (T_s), parallel velocity ($v_\parallel$) and average charge $\overline{Z}$, as function of electron density and temperature at the OSP of WEST lower divertor according to the three groups model.

Conclusion

In the context of developing future tokamak reactors featuring heavy metal components like tungsten (W), the need to predict erosion and transport of impurities becomes increasingly urgent. To date, multispecies fluid codes stand as a valuable numerical tool for modeling impurity transport. However, they lack the capability to resolve local redeposition, as they don't account for transport within the sheath; a crucial factor in heavy impurity contamination. This thesis introduces cost-effective and accurate models to address erosion and redeposition locally. These models are deigned to be integrated with multispecies fluid solvers as boundary condition tools for impurity sources.

The thesis specifically emphasizes W erosion and redeposition, given that W is among the most extensively studied and favored materials for future tokamak reactors. The study was conducted under the assumption of a collisionless-1D plasma background, with erosion and redeposition considered as local phenomena dependent solely on local plasma fluid quantities.

The thesis tackles its subject from various angles: utilizing numerical models such as Monte Carlo techniques and artificial intelligence, employing analytical models for erosion and redeposition, and finally, conducting experiments and analyzing experimental databases to validate the models being studied. The key findings and contributions of this research are here summarized.

In chapter 2 an analytical methodology to account for the whole energy distribution of incident ions is proposed. Monte Carlo simulations of W erosion and redeposition are than applied to assess the consequences of such methods on W erosion and redeposition. Results show that accounting for the energy distribution of incident ions increase both erosion and redeposition of W. This effect is particularly pronounced when sputtering is induced by plasma ions or by impurities in their first ionization state. In the same chapter, a novel approach for computing redeposition, based on the calculation of non-redeposition probability maps, is introduced. By utilizing probability maps, it is possible to directly correlate redeposition with the sputtered energy and angular distributions (SEAD) of sputtered neutrals for any given plasma background. This allows for the calculation of local redeposition through integration rather than particle tracking, resulting in accelerated simulations. These methods have demonstrated the ability to replicate results from earlier literature.

Calculating a probability map on-the-fly anytime the plasma background changes reamins costly and cannot be done in multispecies fluid simulations. In chapter 3 the probability maps are utilized to compute the non-redeposition probability of

physically-sputtered tungsten (W) across a broad spectrum of local plasma parameters and SEAD. These data points are then used to train a Neural Network (NN) with the aim of creating an interpolant function capable of accurately predicting the fraction of non-redeposited W for any local plasma parameters and impinging ions. The NN emerges as an efficient and rapid method for estimating W redeposition fraction, accurately reproducing Monte Carlo results from probability maps within a 20% error margin for 90% of cases, with a maximum error reaching 40%. The NN is the first tool developed in the thesis that could be integrated in multispecies fluid solvers as boundary tool for W local redeposition.

Unfortunately, the NN also has its limitations. In fact, redeposition not only reduces the number of particles entering the domain of the fluid simulation but also alters their charge state, average velocity, temperature, etc., thereby affecting their transport. In general, a comprehensive description of impurity sources requires solving the energy and angular distribution of non-redeposited particles. Indeed, the SEAD from the wall is altered due to redeposition. In the same chapter of the thesis, an attempt is made to find such a solution with an analytical model that takes into account the effect of the electric field, gyromotion, multiple ionization, and varying magnetic angles of incidence. Models from previous literature only considered redeposition related to gyromotion. The model was tuned with numerical data to calculate the SEAD of non-redeposited W particles in the case of a collisionless plasma. Such analytical model not only provides a new theory for redeposition but it can be also used as a valid alternative to NN providing more information about the impurity sources. On top of that, an analytical formulation for the calculation of W prompt-self sputtering is advanced based on numerical results.

Chapter 4 is dedicated to the experimental validation of the underlying assumptions upon which all the thesis work is based. A set of W coatings with different sizes were exposed to a Deuterium L-mode plasma at the lower divertor of DIII-D. Coatings were exposed to identical plasma with varying DC bias relative to the machine potential. Erosion was experimentally measured using Rutherford Back Scattering (RBS) and the Auburn UV spectrometer, which examined the neutral W line at 255.14 nm. Given the 2D nature of the eroded target, the ERO2.0 model was employed to replicate the measured data. Nonetheless, the same hypothesis applied in the thesis were reproduced (e.g. the Boltzmann factor was applied for the density decay, same potential drop, collisionless plasma, and so on) to mimic the fundamental assumptions employed in this study. Overall, numerical and experimental data of net erosion were found to be in agreement, at least for negative bias. The precision of Rutherford Back Scattering (RBS) limited the analyses concerning positive bias. On the other hand, experimentally measured gross erosion rates were six times lower than their numerical counterparts. This difference is likely related to an underestimation of the inverse photon efficiency used to convert the UV photon flux. The last key findings regards the application of the analytical reduced model on the WEST database of the C7 campaign at the Outer Strike Point (OSP) of the lower divertor. A method to estimate the

equivalent concentration of impurities is proposed and the most suitable impurity species to reproduce W erosion is W itself, suggesting that W self sputtering could be one of the major causes of W erosion in the lower divertor of WEST. Along the domain of parameter scanned net and gross flux are directly proportional. An asymmetry between the hot (defined as $T_e \approx 20$ eV and $n_e \sim 1e19$ m^{-3}) and cold ($T_e \approx 3$ eV and $n_e \sim 1e20$ m^{-3}) branches was observed. In hot branch discharges the W source is more screened showing larger promptly redeposited fractions with respect to the cold branch. Finally, eroded W ions in the hot branch tend to be multiply ionized, thus assuming the net flux in the first ionization state is perhaps erroneous.

After providing a list of the main results of the thesis work, it is also pertinent to highlight its limitations and potential for future research. The limitations primarily arise from the assumptions made to describe the eroded material and the physics model of erosion and redeposition. Firstly, the impurity content and charge of the impinging species are not known, leading to the analysis of only parametric studies or proxies. It becomes evident that if the impinging species are not known, any studies attempting to quantify erosion are accompanied by significant uncertainties. Another limitation pertains to the approximations used for the Sputtered Energy and Angular Distribution (SEAD) of neutral sputtered W. Throughout the thesis, a Thompson distribution was assumed, dependent solely on the energy of the incident ion. In reality, the distribution may also be influenced by the angle of incidence, and the azimuthal distribution is not always isotropic. The uncertainties extend to the plasma background and the assumption of locality. Specifically, the plasma sheath can be collisional and may exhibit varying electron and ion temperature profiles, all factors that were not simulated in this thesis. Furthermore, according to the concept of locality, plasma temperature and density are assumed to be more or less constant at the sheath entrance. This spatial limitation becomes evident when erosion occurs in areas with significant electron or temperature gradients along the directions parallel to the eroded surface. Moreover, the model is limited to representing the erosion of components larger than the characteristic length of redeposition of the sputtered species. While locality restricts the spatial scale of the model, the averaging of turbulence limits the temporal scale. Transitional states are neglected, assuming that erosion reaches a steady state rapidly compared to plasma core dynamics.

The comprehensive study of W erosion and redeposition in this thesis may give insights about future perspectives and research. As we consider the achievements and limitations of the current study, several areas emerge for further investigation. The assumptions regarding impurity content and charge of impinging species remain a significant limitation. Future research should focus on refining these assumptions or developing methods to experimentally determine these parameters, allowing for more accurate analyses. Similarly, the investigation of more realistic SEAD of sputtered neutrals may lead to improved predictions of erosion and redeposition. The presented physical model should incorporate collisional effects, electron temperature drop, and variations in plasma parameters at the sheath entrance in order to enhance its accuracy. Moreover, it would be interesting to add the time dynamics of the eroded

material, allowing for surface evolution, as done in other codes. The temporal scale limitations, where transitional states are neglected in favor of steady-state assumptions, should be addressed. Investigating the dynamics of turbulence and transitional phases will provide a more complete understanding of erosion and redeposition processes. In conclusion, the physics model proposed in this thesis (the NN and the analytical model of redeposition) could be integrated to solve boundary sources in fluid solvers such as SOLEDGE. This would open the road to time-dependent studies of erosion and redeposition. Moreover, tha analytical model could be used as a fast tool to calculate importance sampling maps which could be used to reduce the variance in full MC impurity transport codes such as ERO2.0 or GITR. Finally, a concerted effort to refine models and validate assumptions through advanced experiments should be pursued.

Bibliography

[1] T. E. G. Nicholas, T. P. Davis, F. Federici, et al. “Re-examining the role of nuclear fusion in a renewables-based energy mix”. In: *Energy Policy* 149 (Feb. 2021), p. 112043. ISSN: 0301-4215. DOI: 10.1016/j.enpol.2020.112043 (cit. on p. 10).

[2] John Wesson and D. J. Campbell. *Tokamaks*. en. Google-Books-ID: XJssMXjHUr0C. OUP Oxford, Oct. 2011. ISBN: 978-0-19-959223-4 (cit. on p. 10).

[3] John Wesson and D. J. Campbell. *Tokamaks*. en. Google-Books-ID: XJssMXjHUr0C. OUP Oxford, Oct. 2011. ISBN: 978-0-19-959223-4 (cit. on p. 11).

[4] P. N. Yushmanov, T. Takizuka, K. S. Riedel, et al. “Scalings for tokamak energy confinement”. en. In: *Nuclear Fusion* 30.10 (Oct. 1990), p. 1999. ISSN: 0029-5515. DOI: 10.1088/0029-5515/30/10/001 (cit. on p. 11).

[5] M. Bernert, S. Wiesen, O. Février, et al. “The X-Point radiating regime at ASDEX Upgrade and TCV”. In: *Nuclear Materials and Energy* 34 (Mar. 2023), p. 101376. ISSN: 2352-1791. DOI: 10.1016/j.nme.2023.101376 (cit. on pp. 12, 14).

[6] Stefan Costea, David Tskhakaya, Jernej Kovačič, et al. *Particle-In-Cell simulation of parallel blob dynamics in near scrape-off-layer plasma of medium-size tokamak*. June 2017 (cit. on p. 13).

[7] F. Escourbiac, A. Durocher, A. Fedosov, et al. “Assessment of critical heat flux margins on tungsten monoblocks of the ITER divertor vertical targets”. In: *Fusion Engineering and Design*. SI:SOFT-30 146 (Sept. 2019), pp. 2036–2039. ISSN: 0920-3796. DOI: 10.1016/j.fusengdes.2019.03.094 (cit. on p. 14).

[8] R. A. Pitts, S. Carpentier, F. Escourbiac, et al. “A full tungsten divertor for ITER: Physics issues and design status”. In: *Journal of Nuclear Materials*. Proceedings of the 20th International Conference on Plasma-Surface Interactions in Controlled Fusion Devices 438 (July 2013), S48–S56. ISSN: 0022-3115. DOI: 10.1016/j.jnucmat.2013.01.008 (cit. on p. 14).

[9] A. Kallenbach, J. Adamek, L. Aho-Mantila, et al. “Overview of ASDEX Upgrade results”. en. In: *Nuclear Fusion* 51.9 (Aug. 2011), p. 094012. ISSN: 0029-5515. DOI: 10.1088/0029-5515/51/9/094012 (cit. on p. 14).

[10] H. Reimerdes, M. Agostini, E. Alessi, et al. “Overview of the TCV tokamak experimental programme”. en. In: *Nuclear Fusion* 62.4 (Mar. 2022). Publisher: IOP Publishing, p. 042018. ISSN: 0029-5515. DOI: 10.1088/1741-4326/ac369b (cit. on p. 14).

[11] E. Stefanikova, M. Peterka, P. Bohm, et al. “Fitting of the Thomson scattering density and temperature profiles on the COMPASS tokamak”. In: *Review of Scientific Instruments* 87.11 (Aug. 2016), 11E536. ISSN: 0034-6748. DOI: 10.1063/1.4961554 (cit. on p. 14).

[12] Jan Willem Coenen. “Fusion Materials Development at Forschungszentrum Jülich”. en. In: *Advanced Engineering Materials* 22.6 (June 2020), p. 1901376. ISSN: 1438-1656, 1527-2648. DOI: 10.1002/adem.201901376 (cit. on pp. 14, 15).

[13] T. Pütterich, R. Neu, R. Dux, et al. “Calculation and experimental test of the cooling factor of tungsten”. en. In: *Nuclear Fusion* 50.2 (Jan. 2010), p. 025012. ISSN: 0029-5515. DOI: 10.1088/0029-5515/50/2/025012 (cit. on p. 15).

[14] V. Ostuni, J. Morales, J.-F. Artaud, et al. “Core radiative collapse characterisation and integrated modelling in WEST plasmas”. en. In: *Nuclear Fusion* 62.10 (Sept. 2022). Publisher: IOP Publishing, p. 106034. ISSN: 0029-5515. DOI: 10.1088/1741-4326/ac8cd6 (cit. on p. 15).

[15] C. Bourdelle, J. F. Artaud, V. Basiuk, et al. “WEST Physics Basis”. en. In: *Nuclear Fusion* 55.6 (May 2015). Publisher: IOP Publishing, p. 063017. ISSN: 0029-5515. DOI: 10.1088/0029-5515/55/6/063017 (cit. on pp. 15, 61, 101).

[16] YiPing Chen, Dongrui Zhang, Ling Zhang, et al. “Impurity control study of radiative tungsten divertor in EAST tokamak”. In: *Nuclear Materials and Energy* 25 (Dec. 2020), p. 100833. ISSN: 2352-1791. DOI: 10.1016/j.nme.2020.100833 (cit. on p. 15).

[17] A. Kallenbach, for the ASDEX Upgrade Team, and the EUROfusion MST1 Team. “Overview of ASDEX Upgrade results”. en. In: *Nuclear Fusion* 57.10 (June 2017). Publisher: IOP Publishing, p. 102015. ISSN: 0029-5515. DOI: 10.1088/1741-4326/aa64f6 (cit. on p. 15).

[18] J. W. Coenen, G. Arnoux, B. Bazylev, et al. “ELM induced tungsten melting and its impact on tokamak operation”. In: *Journal of Nuclear Materials*. PLASMA-SURFACE INTERACTIONS 21 463 (Aug. 2015), pp. 78–84. ISSN: 0022-3115. DOI: 10.1016/j.jnucmat.2014.08.062 (cit. on pp. 15, 19).

[19] H. Bufferand, G. Ciraolo, Y. Marandet, et al. “Numerical modelling for divertor design of the WEST device with a focus on plasma–wall interactions”. en. In: *Nuclear Fusion* 55.5 (Apr. 2015). Publisher: IOP Publishing, p. 053025. ISSN: 0029-5515. DOI: 10.1088/0029-5515/55/5/053025 (cit. on p. 16).

[20] D. Reiter, M. Baelmans, and P. Börner. “The EIRENE and B2-EIRENE Codes”. In: *Fusion Science and Technology* 47.2 (Feb. 2005). Publisher: Taylor & Francis _eprint: https://doi.org/10.13182/FST47-172, pp. 172–186. ISSN: 1536-1055. DOI: 10.13182/FST47-172 (cit. on p. 16).

[21] Shanlu Gao, Xiaoju Liu, Guozhong Deng, et al. “Tungsten divertor plasma simulation with bundled charge state model by SOLPS-ITER on EAST”. In: *AIP Advances* 11.2 (Feb. 2021), p. 025233. ISSN: 2158-3226. DOI: 10.1063/5.0037381 (cit. on p. 16).

[22] J. Romazanov, D. Borodin, A. Kirschner, et al. “First ERO2.0 modeling of Be erosion and non-local transport in JET ITER-like wall”. en. In: *Physica Scripta* 2017.T170 (Sept. 2017). Publisher: IOP Publishing, p. 014018. ISSN: 1402-4896. DOI: 10.1088/1402-4896/aa89ca (cit. on pp. 16, 25, 32, 36, 93, 94, 96).

[23] T. R. Younkin, D. L. Green, A. B. Simpson, et al. “GITR: An accelerated global scale particle tracking code for wall material erosion and redistribution in fusion relevant plasma–material interactions”. In: *Computer Physics Communications* 264 (July 2021), p. 107885. ISSN: 0010-4655. DOI: 10.1016/j.cpc.2021.107885 (cit. on pp. 16, 32, 36, 51).

[24] S. Di Genova, A. Gallo, N. Fedorczak, et al. “Modelling of tungsten contamination and screening in WEST plasma discharges”. en. In: *Nuclear Fusion* 61.10 (Sept. 2021). Publisher: IOP Publishing, p. 106019. ISSN: 0029-5515. DOI: 10.1088/1741-4326/ac2026 (cit. on pp. 16, 103).

[25] S. Di Genova, G. Ciraolo, A. Gallo, et al. “First 3D modelling of tungsten erosion and migration in WEST discharges adopting a toroidally non-symmetric wall geometry”. In: *Nuclear Materials and Energy* 34 (Mar. 2023), p. 101340. ISSN: 2352-1791. DOI: 10.1016/j.nme.2022.101340 (cit. on pp. 16, 103).

[26] H. Bufferand, P. Tamain, S. Baschetti, et al. “Three-dimensional modelling of edge multi-component plasma taking into account realistic wall geometry”. In: *Nuclear Materials and Energy* 18 (Jan. 2019), pp. 82–86. ISSN: 2352-1791. DOI: 10.1016/j.nme.2018.11.025 (cit. on p. 16).

[27] M. Scotto d’Abusco, G. Giorgiani, J. F. Artaud, et al. “Core-edge 2D fluid modeling of full tokamak discharge with varying magnetic equilibrium: from WEST start-up to ramp-down”. en. In: *Nuclear Fusion* 62.8 (May 2022). Publisher: IOP Publishing, p. 086002. ISSN: 0029-5515. DOI: 10.1088/1741-4326/ac47ad (cit. on p. 17).

[28] Peter Sigmund. *Sputtering by ion bombardment: Theoretical concepts*. Danois. Section: 128 sider. Odense, 1981 (cit. on pp. 18–22).

[29] Rainer Behrisch and Wolfgang Eckstein. *Sputtering by Particle Bombardment: Experiments and Computer Calculations from Threshold to MeV Energies*. en. Google-Books-ID: TSVcpxz3OXcC. Springer Science & Business Media, July 2007. ISBN: 978-3-540-44502-9 (cit. on pp. 19, 53, 103, 104).

[30] Friedrich Aumayr and Hannspeter Winter. “Potential sputtering”. In: *Philosophical Transactions of the Royal Society of London. Series A: Mathematical, Physical and Engineering Sciences* 362.1814 (Nov. 2003). Publisher: Royal Society, pp. 77–102. DOI: 10.1098/rsta.2003.1300 (cit. on p. 19).

[31] V. Philipps, J. Roth, and A. Loarte. “Key issues in plasma–wall interactions for ITER: a European approach”. en. In: *Plasma Physics and Controlled Fusion* 45.12A (Nov. 2003), A17. ISSN: 0741-3335. DOI: 10.1088/0741-3335/45/12A/002 (cit. on pp. 19, 93).

[32] Anna Warren, Anders Nylund, and Ingemar Olefjord. “Oxidation of tungsten and tungsten carbide in dry and humid atmospheres”. In: *International Journal of Refractory Metals and Hard Materials* 14.5 (Jan. 1996), pp. 345–353. ISSN: 0263-4368. DOI: 10.1016/S0263-4368(96)00027-3 (cit. on p. 19).

[33] S. Brezinsek, A. Pospieszczyk, G. Sergienko, et al. “Chemically assisted physical sputtering of Tungsten: Identification via the 6 {Π} → 6 {Σ} + transition of WD in TEXTOR and ASDEX Upgrade plasmas”. en. In: *Nuclear Materials and Energy* 18 (Jan. 2019), pp. 50–55. ISSN: 23521791. DOI: 10.1016/j.nme.2018.12.004 (cit. on p. 19).

[34] Shin Kajita, Naoaki Yoshida, and Noriyasu Ohno. “Tungsten fuzz: Deposition effects and influence to fusion devices”. In: *Nuclear Materials and Energy* 25 (Dec. 2020), p. 100828. ISSN: 2352-1791. DOI: 10.1016/j.nme.2020.100828 (cit. on p. 19).

[35] Yonggang Li, Yang Yang, Michael P. Short, et al. “Ion radiation albedo effect: influence of surface roughness on ion implantation and sputtering of materials”. en. In: *Nuclear Fusion* 57.1 (Dec. 2016). Publisher: IOP Publishing, p. 016038. ISSN: 0029-5515. DOI: 10.1088/1741-4326/57/1/016038 (cit. on pp. 19, 53, 56).

[36] C. García-Rosales, W. Eckstein, and J. Roth. “Revised formulae for sputtering data”. en. In: *Journal of Nuclear Materials* 218.1 (Jan. 1995), pp. 8–17. ISSN: 00223115. DOI: 10.1016/0022-3115(94)00376-9 (cit. on pp. 22, 23, 51).

[37] Xue Yang and Ahmed Hassanein. “Atomic scale calculations of tungsten surface binding energy and beryllium-induced tungsten sputtering”. en. In: *Applied Surface Science* 293 (Feb. 2014), pp. 187–190. ISSN: 01694332. DOI: 10.1016/j.apsusc.2013.12.129 (cit. on p. 22).

[38] J. Bohdansky. “A universal relation for the sputtering yield of monatomic solids at normal ion incidence”. en. In: *Nuclear Instruments and Methods in Physics Research Section B: Beam Interactions with Materials and Atoms* 2.1-3 (Mar. 1984), pp. 587–591. ISSN: 0168583X. DOI: 10.1016/0168-583X(84)90271-4 (cit. on pp. 22, 59).

[39] J. P. Biersack and L. G. Haggmark. “A Monte Carlo computer program for the transport of energetic ions in amorphous targets”. In: *Nuclear Instruments and Methods* 174.1 (Aug. 1980), pp. 257–269. ISSN: 0029-554X. DOI: 10.1016/0029-554X(80)90440-1 (cit. on p. 22).

[40] Yasumichi Yamamura, Yukikazu Itikawa, and Noriaki Itoh. *Angular dependence of sputtering yields of monatomic solids*. eng. IPPJ-AM reports. OCLC: 21725556. Nagoya, Japan: Institute of Plasma Physics, Nagoya University, 1983 (cit. on p. 23).

[41] W. Eckstein and R. Preuss. "New fit formulae for the sputtering yield". en. In: *Journal of Nuclear Materials* 320.3 (Aug. 2003), pp. 209–213. ISSN: 00223115. DOI: 10.1016/S0022-3115(03)00192-2 (cit. on pp. 23, 24, 88, 103).

[42] R. A. Langley, J. Bohdansky, W. Eckstein, et al. "Data Compendium for Plasma-Surface Interactions". en. In: *Nuclear Fusion* 24.S1 (Jan. 1984). Publisher: IOP Publishing, p. 001. ISSN: 0029-5515. DOI: 10.1088/0029-5515/24/S1/001 (cit. on pp. 23, 24).

[43] K. Krieger and J. Roth. "Synergistic effects by simultaneous bombardment of tungsten with hydrogen and carbon". In: *Journal of Nuclear Materials*. 14th Int. Conf. on Plasma-Surface Interactions in Controlled Fusion D evices 290-293 (Mar. 2001), pp. 107–111. ISSN: 0022-3115. DOI: 10.1016/S0022-3115(00)00611-5 (cit. on p. 25).

[44] J. Guterl, T. Abrams, R. Ding, et al. "Dynamic control of low-Z material deposition and tungsten erosion by strike point sweeping on DIII-D". In: *Nuclear Materials and Energy*. Proceedings of the 22nd International Conference on Plasma Surface Interactions 2016, 22nd PSI 12 (Aug. 2017), pp. 392–398. ISSN: 2352-1791. DOI: 10.1016/j.nme.2017.04.017 (cit. on p. 25).

[45] J. Winter. "Wall conditioning in fusion devices and its influence on plasma performance". en. In: *Plasma Physics and Controlled Fusion* 38.9 (Sept. 1996), p. 1503. ISSN: 0741-3335. DOI: 10.1088/0741-3335/38/9/001 (cit. on p. 25).

[46] S. M. Rossnagel. "Thin film deposition with physical vapor deposition and related technologies". In: *Journal of Vacuum Science & Technology A* 21.5 (Sept. 2003), S74–S87. ISSN: 0734-2101. DOI: 10.1116/1.1600450 (cit. on p. 25).

[47] P. Manz, N. Fedorczak, T. Dittmar, et al. "Nonlinear evolution of surface morphology under shadowing". In: *Physical Review E* 87.4 (Apr. 2013). Publisher: American Physical Society, p. 042404. DOI: 10.1103/PhysRevE.87.042404 (cit. on p. 25).

[48] J.N. Brooks, T. Sizyuk, G. Sinclair, et al. "Tungsten–carbon surface evolution and erosion modeling for a small angle slot divertor in DIII-D". en. In: *Nuclear Fusion* 61.12 (Dec. 2021), p. 126071. ISSN: 0029-5515, 1741-4326. DOI: 10.1088/1741-4326/ac36f4 (cit. on p. 26).

[49] P. C. Stangeby. *The Plasma Boundary of Magnetic Fusion Devices*. en. Google-Books-ID: qOliQgAACAAJ. Taylor & Francis, Jan. 2000. ISBN: 978-0-7503-0559-4 (cit. on pp. 26, 28–31, 39, 96).

[50] K.-U. Riemann. "The Bohm criterion and sheath formation". en. In: *Journal of Physics D: Applied Physics* 24.4 (Apr. 1991), p. 493. ISSN: 0022-3727. DOI: 10.1088/0022-3727/24/4/001 (cit. on p. 27).

[51] Roland Chodura. “Plasma Flow in the Sheath and the Presheath of a Scrape-Off Layer”. en. In: *Physics of Plasma-Wall Interactions in Controlled Fusion*. Ed. by D. E. Post and R. Behrisch. Boston, MA: Springer US, 1986, pp. 99–134. ISBN: 978-1-4757-0067-1. DOI: 10.1007/978-1-4757-0067-1_4 (cit. on p. 28).

[52] J. P. Gunn, V. Fuchs, and M. Kočan. “A kinetic model of retarding field analyser measurements in strongly magnetized, flowing, collisional plasmas”. en. In: *Plasma Physics and Controlled Fusion* 55.4 (Mar. 2013). Publisher: IOP Publishing, p. 045012. ISSN: 0741-3335. DOI: 10.1088/0741-3335/55/4/045012 (cit. on pp. 28, 39).

[53] J. E. Allen. “The plasma–sheath boundary: its history and Langmuir’s definition of the sheath edge”. en. In: *Plasma Sources Science and Technology* 18.1 (Nov. 2008), p. 014004. ISSN: 0963-0252. DOI: 10.1088/0963-0252/18/1/014004 (cit. on p. 28).

[54] R. N. Franklin. “Where is the ‘sheath edge’?” en. In: *Journal of Physics D: Applied Physics* 37.9 (Apr. 2004), p. 1342. ISSN: 0022-3727. DOI: 10.1088/0022-3727/37/9/007 (cit. on p. 28).

[55] D. Tskhakaya. “One-dimensional plasma sheath model in front of the divertor plates”. en. In: *Plasma Physics and Controlled Fusion* 59.11 (Sept. 2017). Publisher: IOP Publishing, p. 114001. ISSN: 0741-3335. DOI: 10.1088/1361-6587/aa8486 (cit. on pp. 28, 36, 59).

[56] Rinat Khaziev and Davide Curreli. “Ion energy-angle distribution functions at the plasma-material interface in oblique magnetic fields”. In: *Physics of Plasmas* 22.4 (Apr. 2015), p. 043503. ISSN: 1070-664X. DOI: 10.1063/1.4916910 (cit. on p. 29).

[57] I. E. Borodkina, M. Komm, and I. V. Tsvetkov. “Application of Analytical Model of the Electric Potential Distribution for Calculation of Charged Particle Dynamics in a Near-Wall Layer and Sputtering of the Plasma Facing Surfaces”. en. In: *Russian Physics Journal* 58.4 (Aug. 2015), pp. 438–445. ISSN: 1064-8887, 1573-9228. DOI: 10.1007/s11182-015-0518-5 (cit. on p. 29).

[58] I. Borodkina, D. Borodin, A. Kirschner, et al. “An Analytical Expression for the Electric Field and Particle Tracing in Modelling of Be Erosion Experiments at the JET ITER-like Wall”. en. In: *Contributions to Plasma Physics* 56.6-8 (Aug. 2016), pp. 640–645. ISSN: 0863-1042, 1521-3986. DOI: 10.1002/ctpp.201610032 (cit. on pp. 29, 30, 37, 46, 50, 54, 97).

[59] I Borodkina, D Borodin, S Brezinsek, et al. “Surface biasing influence on the physical sputtering in fusion devices”. en. In: *Journal of Physics: Conference Series* 748 (Sept. 2016), p. 012002. ISSN: 1742-6588, 1742-6596. DOI: 10.1088/1742-6596/748/1/012002 (cit. on pp. 29, 64, 93).

[60] N. Mellet, J. P. Gunn, B. Pégourié, et al. “Tungsten erosion by impurities and redeposition: focus on the magnetised sheath”. en. In: *Plasma Physics and Controlled Fusion* 59.3 (Feb. 2017). Publisher: IOP Publishing, p. 035006. ISSN: 0741-3335. DOI: 10.1088/1361-6587/aa576c (cit. on pp. 29, 36, 38–40, 43, 52, 104).

[61] J. P. Gunn. “The influence of magnetization strength on the sheath: Implications for flush-mounted probes”. In: *Physics of Plasmas* 4.12 (Dec. 1997), pp. 4435–4446. ISSN: 1070-664X. DOI: 10.1063/1.872608 (cit. on p. 29).

[62] P. C. Stangeby. “The Chodura sheath for angles of a few degrees between the magnetic field and the surface of divertor targets and limiters”. en. In: *Nuclear Fusion* 52.8 (July 2012). Publisher: IOP Publishing and International Atomic Energy Agency, p. 083012. ISSN: 0029-5515. DOI: 10.1088/0029-5515/52/8/083012 (cit. on pp. 30, 37, 54, 97).

[63] C. P. C. Wong, R. Junge, R. D. Phelps, et al. “Divertor materials evaluation system at DIII-D”. In: *Journal of Nuclear Materials*. Plasma-Surface Interactions in Controlled Fusion Devices 196-198 (Dec. 1992), pp. 871–875. ISSN: 0022-3115. DOI: 10.1016/S0022-3115(06)80159-5 (cit. on pp. 30, 94).

[64] K-S. Chung and I. H. Hutchinson. “Kinetic theory of ion collection by probing objects in flowing strongly magnetized plasmas”. en. In: *Physical Review A* 38.9 (Nov. 1988), pp. 4721–4731. ISSN: 0556-2791. DOI: 10.1103/PhysRevA.38.4721 (cit. on p. 32).

[65] S. Abe, C.H. Skinner, I. Bykov, et al. “Experimental verification of ion impact angle distribution at divertor surfaces using micro-engineered targets on DiMES at DIII-D”. en. In: *Nuclear Materials and Energy* 27 (June 2021), p. 100965. ISSN: 23521791. DOI: 10.1016/j.nme.2021.100965 (cit. on pp. 32, 96).

[66] S. Devaux and G. Manfredi. “Magnetized plasma–wall transition—consequences for wall sputtering and erosion”. en. In: *Plasma Physics and Controlled Fusion* 50.2 (Jan. 2008), p. 025009. ISSN: 0741-3335. DOI: 10.1088/0741-3335/50/2/025009 (cit. on p. 32).

[67] G. Kawamura, Y. Tomita, and A. Kirschner. “Kinetic effects of inclined magnetic field on physical sputtering by impurity ions”. In: *Journal of Nuclear Materials*. Proceedings of the 20th International Conference on Plasma-Surface Interactions in Controlled Fusion Devices 438 (July 2013), S909–S912. ISSN: 0022-3115. DOI: 10.1016/j.jnucmat.2013.01.197 (cit. on p. 32).

[68] M. Elias, D. Curreli, and J. R. Myra. “Energy-angle distribution of the ions in the RF sheath of ICRH antennas”. In: *Physics of Plasmas* 28.5 (May 2021), p. 052106. ISSN: 1070-664X. DOI: 10.1063/5.0045962 (cit. on p. 32).

[69] V.A. Abramov, Yu.L. Igitkhanov, V.I. Pistunovich, et al. “First wall and divertor plate sputtering in a tokamak reactor”. en. In: *Journal of Nuclear Materials* 162-164 (Apr. 1989), pp. 462–466. ISSN: 00223115. DOI: 10.1016/0022-3115(89)90313-9 (cit. on pp. 32, 51).

[70] R. H. Cohen and D. D. Ryutov. “Particle trajectories in a sheath in a strongly tilted magnetic field”. en. In: *Physics of Plasmas* 5.3 (Mar. 1998), pp. 808–817. ISSN: 1070-664X, 1089-7674. DOI: 10.1063/1.872764 (cit. on p. 32).

[71] H. Bufferand, B. Bensiali, J. Bucalossi, et al. “Near wall plasma simulation using penalization technique with the transport code SolEdge2D-Eirene”. In: *Journal of Nuclear Materials*. Proceedings of the 20th International Conference on Plasma-Surface Interactions in Controlled Fusion Devices 438 (July 2013), S445–S448. ISSN: 0022-3115. DOI: 10.1016/j.jnucmat.2013.01.090 (cit. on p. 33).

[72] S. Wiesen, D. Reiter, V. Kotov, et al. “The new SOLPS-ITER code package”. In: *Journal of Nuclear Materials*. PLASMA-SURFACE INTERACTIONS 21 463 (Aug. 2015), pp. 480–484. ISSN: 0022-3115. DOI: 10.1016/j.jnucmat.2014.10.012 (cit. on p. 33).

[73] L. Cappelli, N. Fedorczak, J. P. Gunn, et al. “Study of the erosion and redeposition of W considering the kinetic energy distribution of incident ions through a semi-analytical model”. en. In: *Plasma Physics and Controlled Fusion* 65.9 (July 2023). Publisher: IOP Publishing, p. 095001. ISSN: 0741-3335. DOI: 10.1088/1361-6587/ace282 (cit. on p. 34).

[74] 1994 International Conference on Plasma Physics and Controlled Nuclear Fusion Research (15 Sevilla). *Plasma physics and controlled nuclear fusion research 1994: proceedings of the fifteenth International Conference on Plasma Physics and Controlled Nuclear Fusion Research, held by the International Atomic Energy Agency in Seville, 26 September - 1 October 1994 : in four volumes. 3*. Anglais. Proceedings series. Section: 731 Seiten : Illustrationen, Diagramme. Vienna: IAEA, 1996. ISBN: 978-92-0-103795-4 (cit. on pp. 35, 47, 50, 70, 71, 74–76, 79).

[75] A V Chankin, D P Coster, and R Dux. “Monte Carlo simulations of tungsten redeposition at the divertor target”. en. In: *Plasma Physics and Controlled Fusion* 56.2 (Feb. 2014), p. 025003. ISSN: 0741-3335, 1361-6587. DOI: 10.1088/0741-3335/56/2/025003 (cit. on pp. 35, 37, 41, 42, 54, 94).

[76] J. Guterl, I. Bykov, R. Ding, et al. “On the prediction and monitoring of tungsten prompt redeposition in tokamak divertors”. In: *Nuclear Materials and Energy* 27 (June 2021), p. 100948. ISSN: 2352-1791. DOI: 10.1016/j.nme.2021.100948 (cit. on pp. 35, 41, 42, 44, 45, 50, 98).

[77] D. Tskhakaya and M. Groth. “Modelling of tungsten re-deposition coefficient”. In: *Journal of Nuclear Materials*. PLASMA-SURFACE INTERACTIONS 21 463 (Aug. 2015), pp. 624–628. ISSN: 0022-3115. DOI: 10.1016/j.jnucmat.2014.10.086 (cit. on pp. 35, 42, 76).

[78] A. Kirschner, V. Philipps, J. Winter, et al. “Simulation of the plasma-wall interaction in a tokamak with the Monte Carlo code ERO-TEXTOR”. en. In: *Nuclear Fusion* 40.5 (May 2000), p. 989. ISSN: 0029-5515. DOI: 10.1088/0029-5515/40/5/311 (cit. on pp. 36, 44).

[79] H. A. Kumpulainen, M. Groth, G. Corrigan, et al. “Validation of EDGE2D-EIRENE and DIVIMP for W SOL transport in JET”. In: *Nuclear Materials and Energy* 25 (Dec. 2020), p. 100866. ISSN: 2352-1791. DOI: 10.1016/j.nme.2020.100866 (cit. on p. 36).

[80] K. Shimizu, H. Kubo, T. Takizuka, et al. “Impurity transport modelling and simulation analysis of impurity behavior in JT-60U”. In: *Journal of Nuclear Materials*. Plasma-Surface Interactions in Controlled Fusion Devices 220-222 (Apr. 1995), pp. 410–414. ISSN: 0022-3115. DOI: 10.1016/0022-3115(94)00499-4 (cit. on p. 36).

[81] M. W. Thompson. “II. The energy spectrum of ejected atoms during the high energy sputtering of gold”. In: *The Philosophical Magazine: A Journal of Theoretical Experimental and Applied Physics* 18.152 (Aug. 1968). Publisher: Taylor & Francis _eprint: https://doi.org/10.1080/14786436808227358, pp. 377–414. ISSN: 0031-8086. DOI: 10.1080/14786436808227358 (cit. on pp. 36, 96).

[82] A. Eksaeva, E. Marenkov, D. Borodin, et al. “ERO modelling of tungsten erosion in the linear plasma device PSI-2”. en. In: *Nuclear Materials and Energy* 12 (Aug. 2017), pp. 253–260. ISSN: 23521791. DOI: 10.1016/j.nme.2017.03.014 (cit. on pp. 36, 98).

[83] G. Falcone. “Sputtering theory”. en. In: *La Rivista del Nuovo Cimento (1978-1999)* 13.1 (Jan. 1990), pp. 1–52. ISSN: 1826-9850. DOI: 10.1007/BF02742981 (cit. on p. 36).

[84] A. Kirschner, D. Matveev, D. Borodin, et al. “Modelling of the material transport and layer formation in the divertor of JET: Comparison of ITER-like wall with full carbon wall conditions”. In: *Journal of Nuclear Materials*. PLASMA-SURFACE INTERACTIONS 21 463 (Aug. 2015), pp. 116–122. ISSN: 0022-3115. DOI: 10.1016/j.jnucmat.2014.10.072 (cit. on pp. 36, 37).

[85] D Borodin, S Brezinsek, J Miettunen, et al. “Determination of Be sputtering yields from spectroscopic observations at the JET ITER-like wall based on three-dimensional ERO modelling”. en. In: *Physica Scripta* T159 (Apr. 2014), p. 014057. ISSN: 0031-8949, 1402-4896. DOI: 10.1088/0031-8949/2014/T159/014057 (cit. on p. 36).

[86] A. Kirschner, D. Tskhakaya, G. Kawamura, et al. “Modelling of Impurity Transport and Plasma–Wall Interaction in Fusion Devices with the ERO Code: Basics of the Code and Examples of Application”. en. In: *Contributions to Plasma Physics* 56.6-8 (2016), pp. 622–627. ISSN: 1521-3986. DOI: 10.1002/ctpp.201610014 (cit. on p. 36).

[87] A. Kirschner, D. Tskhakaya, S. Brezinsek, et al. “Modelling of plasma-wall interaction and impurity transport in fusion devices and prompt deposition of tungsten as application”. en. In: *Plasma Physics and Controlled Fusion* 60.1 (Nov. 2017). Publisher: IOP Publishing, p. 014041. ISSN: 0741-3335. DOI: 10.1088/1361-6587/aa8dce (cit. on pp. 36, 44, 93).

[88] J. P. Gunn, S. Carpentier-Chouchana, F. Escourbiac, et al. “Surface heat loads on the ITER divertor vertical targets”. en. In: *Nuclear Fusion* 57.4 (Mar. 2017). Publisher: IOP Publishing, p. 046025. ISSN: 0029-5515. DOI: 10.1088/1741-4326/aa5e2a (cit. on p. 37).

[89] J. N. Brooks. “Near-surface sputtered particle transport for an oblique incidence magnetic field plasma”. In: *Physics of Fluids B* 2 (Aug. 1990). ADS Bibcode: 1990PhFlB...2.1858B, pp. 1858–1863. ISSN: 0899-8221. DOI: 10.1063/1.859457 (cit. on p. 37).

[90] H. P. Summers. *The ADAS User Manual*. 2004 (cit. on pp. 37, 40, 45, 103–106).

[91] J. P. Gunn. “Kinetic investigation of a collisionless scrape-off layer with a source of poloidal momentum”. In: *Journal of Nuclear Materials*. PSI-16 337-339 (Mar. 2005), pp. 310–314. ISSN: 0022-3115. DOI: 10.1016/j.jnucmat.2004.10.054 (cit. on pp. 38, 39).

[92] C K Birdsall and A B Langdon. *Plasma physics via Computer Simulation*. IOP Publishing Ltd, 1991. ISBN: 978-0-7503-1025-3 (cit. on pp. 41, 52).

[93] Lieberman et al. “Principles of plasma discharges and materials processing”. In: *MRS Bulletin* 30.12 (1994), pp. 899–901 (cit. on p. 41).

[94] J. Guterl, W. R. Wampler, D. Rudakov, et al. “Reduced model of high-Z impurity redeposition and erosion in tokamak divertor and its application to DIII-D experiments”. en. In: *Plasma Physics and Controlled Fusion* 61.12 (Nov. 2019). Publisher: IOP Publishing, p. 125015. ISSN: 0741-3335. DOI: 10.1088/1361-6587/ab5144 (cit. on p. 46).

[95] C. A. Johnson, S. D. Loch, and D. A. Ennis. “The effect of metastable atomic levels in neutral tungsten for erosion and impurity transport applications”. en. In: *Plasma Physics and Controlled Fusion* 62.12 (Nov. 2020). Publisher: IOP Publishing, p. 125017. ISSN: 0741-3335. DOI: 10.1088/1361-6587/abc08b (cit. on pp. 55, 99).

[96] Sergey Ioffe and Christian Szegedy. *Batch Normalization: Accelerating Deep Network Training by Reducing Internal Covariate Shift*. arXiv:1502.03167 [cs]. Mar. 2015. DOI: 10.48550/arXiv.1502.03167 (cit. on p. 59).

[97] Genevieve B. Orr and Klaus-Robert Müller. *Neural Networks: Tricks of the Trade*. en. Google-Books-ID: VCKqCAAAQBAJ. Springer, July 2003. ISBN: 978-3-540-49430-0 (cit. on p. 59).

[98] Ian Goodfellow, Yoshua Bengio, and Aaron Courville. *Deep Learning*. MIT Press, 2016 (cit. on p. 60).

[99] François Chollet. *Keras*. 2015 (cit. on p. 60).

[100] Diederik P. Kingma and Jimmy Ba. *Adam: A Method for Stochastic Optimization*. arXiv:1412.6980 [cs]. Jan. 2017. DOI: 10.48550/arXiv.1412.6980 (cit. on p. 60).

[101] Eric Jones, Travis Oliphant, Pearu Peterson, et al. "SciPy: Open source scientific tools for Python". In: (2001) (cit. on p. 60).

[102] Pauli Virtanen, Ralf Gommers, Travis E. Oliphant, et al. "SciPy 1.0: fundamental algorithms for scientific computing in Python". en. In: *Nature Methods* 17.3 (Mar. 2020). Number: 3 Publisher: Nature Publishing Group, pp. 261–272. ISSN: 1548-7105. DOI: 10.1038/s41592-019-0686-2 (cit. on p. 60).

[103] Yuki Homma and Akiyoshi Hatayama. "Numerical modeling of thermal force in a plasma for test-ion transport simulation based on Monte Carlo Binary Collision Model". In: *Journal of Computational Physics* 231.8 (Apr. 2012), pp. 3211–3227. ISSN: 0021-9991. DOI: 10.1016/j.jcp.2011.12.037 (cit. on p. 76).

[104] S. P. Hirshman and D. J. Sigmar. "Neoclassical transport of impurities in tokamak plasmas". en. In: *Nuclear Fusion* 21.9 (Sept. 1981), p. 1079. ISSN: 0029-5515. DOI: 10.1088/0029-5515/21/9/003 (cit. on p. 77).

[105] L. Cappelli, J. Guterl, N. Fedorczak, et al. "Model validation of tungsten erosion and redeposition properties using biased tungsten samples on DiMES". In: *Nuclear Materials and Energy* 37 (Dec. 2023), p. 101551. ISSN: 2352-1791. DOI: 10.1016/j.nme.2023.101551 (cit. on p. 93).

[106] C. P. C Wong, D. G Whyte, R. J Bastasz, et al. "Divertor materials evaluation system (DiMES)". In: *Journal of Nuclear Materials* 258-263 (Oct. 1998), pp. 433–439. ISSN: 0022-3115. DOI: 10.1016/S0022-3115(98)00407-3 (cit. on p. 94).

[107] R. Ding, D. L. Rudakov, P. C. Stangeby, et al. "Advances in understanding of high-Z material erosion and re-deposition in low-Z wall environment in DIII-D". en. In: *Nuclear Fusion* 57.5 (Mar. 2017). Publisher: IOP Publishing, p. 056016. ISSN: 0029-5515. DOI: 10.1088/1741-4326/aa6451 (cit. on pp. 94, 98).

[108] F. Glass, T. N. Carlstrom, D. Du, et al. "Upgraded divertor Thomson scattering system on DIII-D". eng. In: *The Review of Scientific Instruments* 87.11 (Nov. 2016), 11E508. ISSN: 1089-7623. DOI: 10.1063/1.4955281 (cit. on p. 95).

[109] P. C. Stangeby, D. L. Rudakov, W. R. Wampler, et al. "An experimental comparison of gross and net erosion of Mo in the DIII-D divertor". In: *Journal of Nuclear Materials*. Proceedings of the 20th International Conference on Plasma-Surface Interactions in Controlled Fusion Devices 438 (July 2013), S309–S312. ISSN: 0022-3115. DOI: 10.1016/j.jnucmat.2013.01.052 (cit. on pp. 95, 98).

[110] T. Abrams, R. Ding, H.Y. Guo, et al. "The inter-ELM tungsten erosion profile in DIII-D H-mode discharges and benchmarking with ERO+OEDGE modeling". en. In: *Nuclear Fusion* 57.5 (May 2017), p. 056034. ISSN: 0029-5515, 1741-4326. DOI: 10.1088/1741-4326/aa66b2 (cit. on p. 97).

[111] D. L. Rudakov, P. C. Stangeby, W. R. Wampler, et al. “Net versus gross erosion of high-Z materials in the divertor of DIII-D”. en. In: *Physica Scripta* 2014.T159 (Apr. 2014). Publisher: IOP Publishing, p. 014030. ISSN: 1402-4896. DOI: 10.1088/0031-8949/2014/T159/014030 (cit. on p. 98).

[112] J. Bucalossi, J. Achard, O. Agullo, et al. “Operating a full tungsten actively cooled tokamak: overview of WEST first phase of operation”. en. In: *Nuclear Fusion* 62.4 (Feb. 2022). Publisher: IOP Publishing, p. 042007. ISSN: 0029-5515. DOI: 10.1088/1741-4326/ac2525 (cit. on p. 101).

[113] R. Guirlet, C. Desgranges, J. L. Schwob, et al. “Extreme UV spectroscopy measurements and analysis for tungsten density studies in the WEST tokamak”. en. In: *Plasma Physics and Controlled Fusion* 64.10 (Sept. 2022). Publisher: IOP Publishing, p. 105024. ISSN: 0741-3335. DOI: 10.1088/1361-6587/ac8d2c (cit. on pp. 101, 104).

[114] S. Brezinsek, M. Laengner, J. W. Coenen, et al. “Spectroscopic determination of inverse photon efficiencies of W atoms in the scrape-off layer of TEXTOR”. en. In: *Physica Scripta* 2017.T170 (Oct. 2017). Publisher: IOP Publishing, p. 014052. ISSN: 1402-4896. DOI: 10.1088/1402-4896/aa8a45 (cit. on pp. 103–106).

[115] Blaise Faugeras. “An overview of the numerical methods for tokamak plasma equilibrium computation implemented in the NICE code”. In: *Fusion Engineering and Design* 160 (Nov. 2020), p. 112020. ISSN: 0920-3796. DOI: 10.1016/j.fusengdes.2020.112020 (cit. on p. 104).